X-ray Diffraction Study of Cu(111)/Electrolyte Interfaces

By
Yong Song Chu

B.S., California Insitute of Technology, 1989
M.S., University of Illinois at Urbana-Champaign, 1990

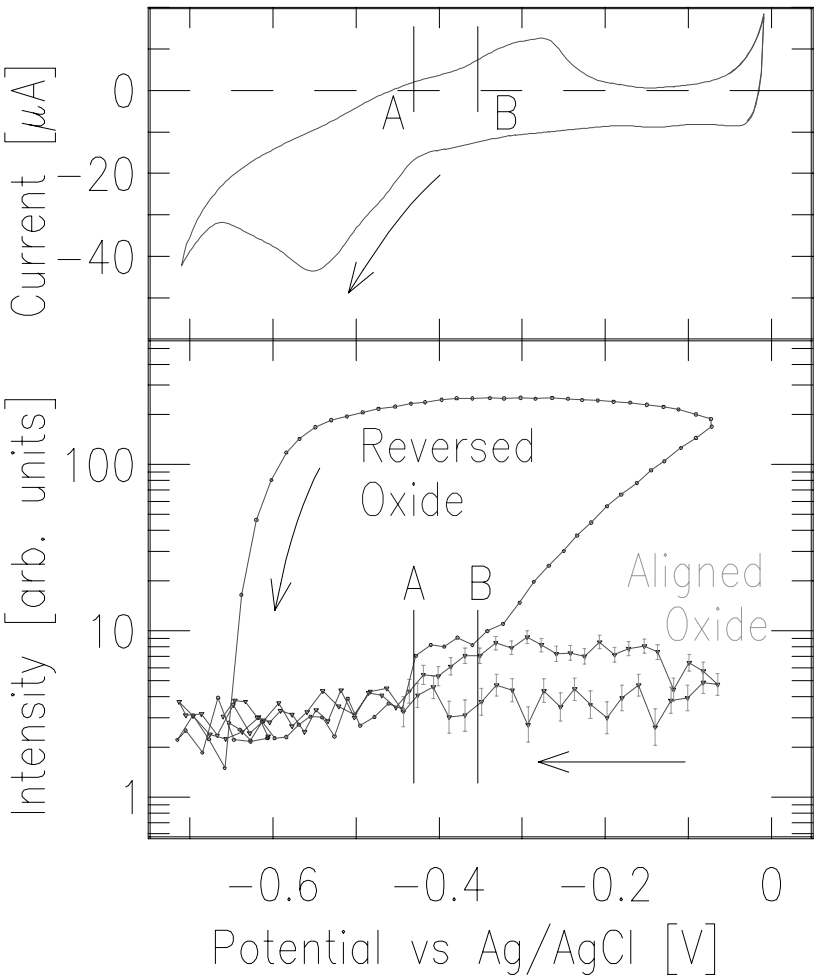

X-RAY DIFFRACTION STUDY ON Cu(111)/ELECTROLYTE INTERFACES

Yong Song Chu, Ph. D.
Department of Physics
University of Illinois at Urbana-Champaign, 1997
Ian K. Robinson, Advisor

An experimental study of the interfacial structures at the Cu(111) surface under various electrochemical environments is presented. The interfacial structures have been examined with the synchrotron x-ray diffraction. Here, three different Cu(111)/electrolyte systems are discussed.

In the first experiment, the properties of the underpotentially deposited (UPD) Pb monolayer on the Cu(111) surface was studied. The Pb UPD monolayer formed an incommensurate hexagonal closed-packed structure, aligned with the Cu(111) substrate. Both in-plane and surface-normal structure of Pb/Cu(111) was studied as a function of the electrochemical potential. While the surface-normal structure of the Pb/Cu(111) system exhibited no potential dependence, the in-plane structure of the Pb monolayer responded sensitively to the potential. The compression behavior the Pb monolayer showed excellent agreement with the free-electron gas model.

Next, the structure of the bare Cu(111) surface in 0.1 M $HClO_4$ (pH $\approx$1) was studied. The study revealed that there were two distinct interfacial structures. For a wide potential range negative of the Nernst potential, the Cu(111) surface was not bare but adsorbed with oxygen or hydroxide. The bare Cu(111) surface was observed only at the onset of the hydrogen evolution. The CTR (crystal truncation rods) analysis showed that the oxygen atoms are adsorbed at the 3-fold hollow sites of the Cu(111) substrate. The

observed bond length was consistent with the known Cu-O bond length. The presence of the oxygen adlayer in the pH regions (pH <3.5), in which the bulk oxide is forbidden, has significant thermodynamic implication, and the adsorbed oxygen monolayer can be interpreted as the precursor to the bulk oxide.

In a less acidic electrolyte (pH=4.5), the growth of aqueous oxide was observed. The aqueous oxide exhibited an epitaxial cubic Cu_2O (cuprite) structure. Two distinct epitaxial structures were found: the "aligned' cuprite with its $(1\,\bar{1}\,0)$ axis parallel with the substrate $(1\,\bar{1}\,0)$ axis and the "reversed" cuprite with its $(1\,\bar{1}\,0)$ axis anti-parallel with the substrate $(1\,\bar{1}\,0)$ axis. While the "reversed" cuprite was found to grow into a thick film, the "aligned" cuprite remained as a thin 2D film. The growth of the aqueous oxide showed the distinct growth modes, which are different from the those of the previously reported "dry" oxide grown under vacuum.

Acknowledgments

I was extremely fortunate to have Ian K. Robinson as a thesis advisor. I have benefited enormously from his expertise and intellect. Not only is he an exemplary scientist and mentor but also a kind and generous person with a great sense of humor.

The members of Robinson's research group and friends have provided me with intellectual and moral support. They are Kevin Whiteaker, Arunaba Gosh, Don Wacko, David Fanning, Chinkyo Kim, John Pitney, Libbert (the former post-doc), Curtis Beson (the former student), and Ken Ritely.

I would like to expressed my deepest gratitude to Prof. Andy A. Gewirth. Without his expertise in electrochemistry, my thesis work would have been possible. I also thank his student, Brian Niece, who taught me a number of practical aspects of electrochemistry. The CV data acquisition program used for experiments was adopted from his original codes.

I would like to thank Dr. Ben M. Ocko at Brookhaven National Lab. He allowed me to use his lab during the experiments at NSLS and provided me with valuable discussion on many aspects of the experments.

This material is based upon work supported by was by the U.S. Department of Energy under Contract No. DEFG02-96ER45439 to the Materials Research Laboratory. The National Synchrotron Light Source is supported by Department of Energy, Contract No. DEAC012-76CH00016.

This work would not been possible without the support and enthusiastic encouragement of my wife, Young.

Table of Contents

List of Tables

List of Figures

1. Overview on Electrochemical Interfaces.

1.1 Background and motivation

The structure of the interfacial region between a metal and an aqueous electrolyte[1] is the most fundamental question in electrochemistry. Significant effort has been directed toward understanding the structure of metal/electrolyte interface for more than 100 years. In addition to academic interest, metal/electrolyte interface is of significant practical interest because many important reactions such as metal dissolution/deposition, charge transfer, corrosion, oxidation, electroorganic synthesis, and catalysis take place at the interface. In order to understand these processes on the fundamental level, it is imperative to know the microscopic structure of the interface. Yet, for a long time, the refinement of interfacial models had been solely based on macroscopic thermodynamic measurements, particularly the measurements of electrocapillary curve for mercury. Electrocapillary curve measurements utilize the fact that the interfacial tension depends on the electrode potential [1]. A thermodynamically rigorous treatment of the interface has been possible only for liquid metals due to the lack of reliable surface tension methods for solid electrodes.

The first model for metal/electrolyte interface was proposed in 1879 by Helmholtz [2]. According to his extremely simplified model, the excess charges on the metal surface are balanced by an equal number of opposite charges at one plane on the solution side, forming an electric "double layer", and the at the interface potential changes linearly over a thickness of one

---

[1] Although much of the discussion presented here is applicable to non-aqueous solution, the discussion is focused on metal/aqueous electrolyte interfaces.

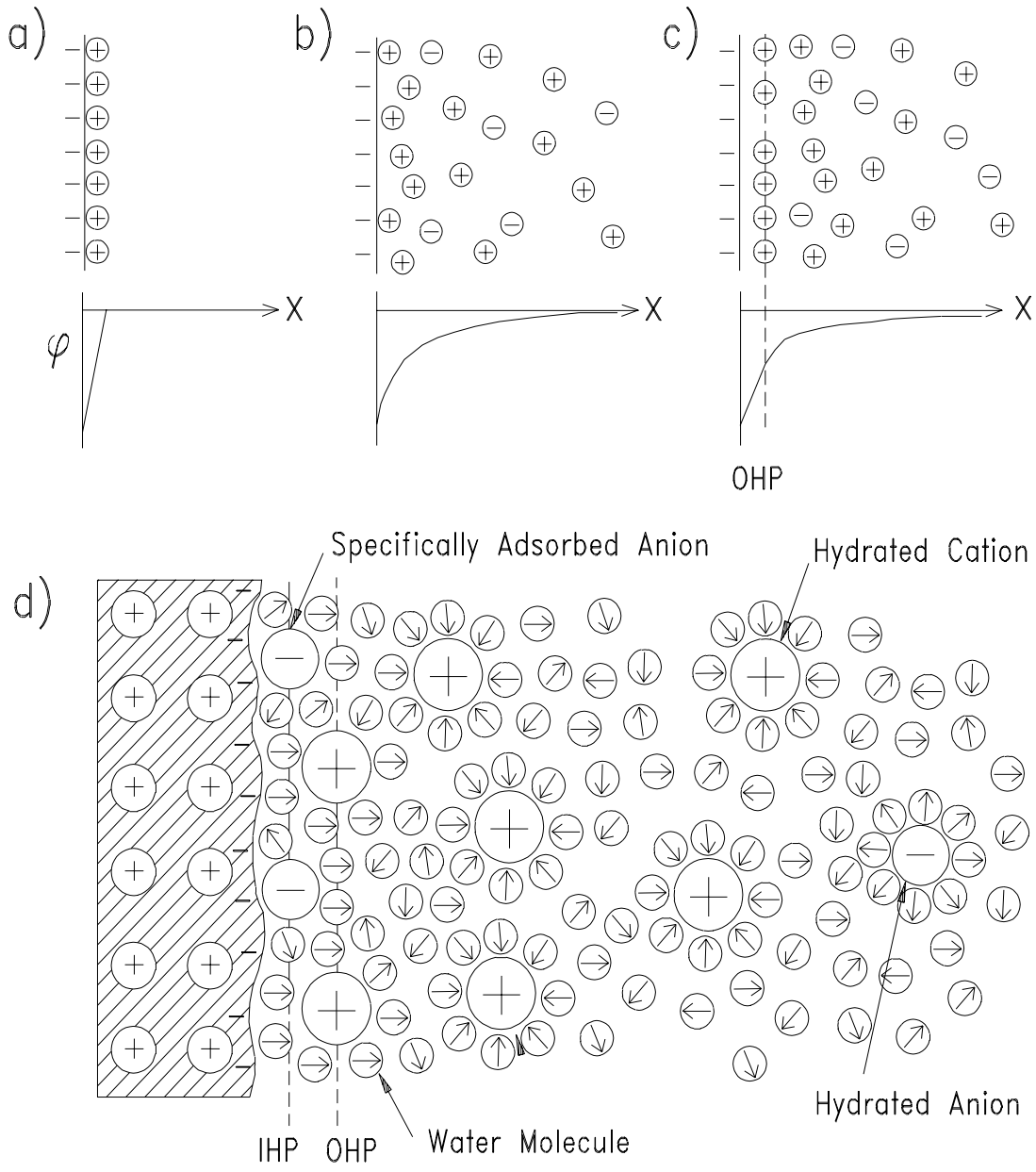

Figure 1: Models of the electric double layer: a) Helmholtz's Model, b) Gouy-Chapman's Model, c) Stern' Model. d) a more Modern model in which the metal is no longer viewed as a structureless metallic plane. It also includes oriented water molecules, specific adsorption, and hydrated ions.

ion layer (see Fig. 1a). An obvious prediction of this model, proven to be in gross disagreement with the experimental results, is that the capacitance of the double layer is independent of the electrode potential. An entirely opposite approach was taken by Gouy in 1910 and three years later by Chapman [3]. In so-called "diffuse-layer model", there is no Helmholtz layer, and the electrolyte is represented as point charges in a structureless constant dielectric medium, distributed according to the electrostatic potential provided by the excess charge on the metal surface (see Fig. 1b). In the Gouy-Chapman treatment, the interfacial potential is determined from one dimensional Poisson equation, and the concentration profile of the ions obeys the Boltzman distribution. This model predicts hyperbolic (differential) capacitance as a function of electrode potential, which was found to be true only near PZC (potential of zero charge) in very dilute 1:1 electrolytes[2] (<0.001 M). Treating an ion as a spherical charge with cloud of (opposite) charge distribution, Stern proposed in 1924 that there are two layers in the electrolyte (see Fig. 1c). Some of the excess charges are in the outer Helmholtz plane (OHP) due to finite size of the ion, and the remainder are distributed in the diffused layer [4]. An immediate consequence of this model is that the potential drop across the double layer consists of two parts. Within OHP, the potential changes linearly, whereas, in the diffuse layer, it changes exponentially with the distance from the electrode. Another equivalent way to view this model is that the total capacitance of the double layer is a harmonic average of those of the Helmholtz and the diffuse layer (two capacitor in series). Stern's model approaches to Helmholtz' model in very concentrated electrolytes (> 1 M) and to Gouy's model in very dilute electrolytes (<0.001 M). No significant changes in the model had occurred until dipolar properties of water molecule were considered in 1950's and 1960's [5,6,7,8]. According to these models, water molecules are supposed to occupy the first layer just outside of

[2] symmetric electrolytes. For example, NaF is an 1:1 electrolyte while Na_2SO_4 is not.

the metal surface (the inner Helmholtz layer), with their dipole moments aligned with electrostatic fields. The ions are hydrated (shielded by water molecules) and can only approach within a certain distance from the metal surface (up to the outer Helmholtz plane). The rest of the hydrated ions are distributed in the diffuse layer in the essentially same manner as the Gouy-Chapman treatment. More recent models include sophisticated arrangement of orientations of water dipoles allowing the possibility of hydrogen bonding between them [9] and even a network of hydrogen bonds at the metal surface [10].

Many simplistic models described above do not work for most systems because the metal-electrolyte interaction can not be adequately described by electrostatics alone. In order to describe realistic metal/electrode interfaces, chemical interactions must be included. As the ions approach the metal surface, they can lose some or all of their hydration shells and form chemical bonds with the metal surface. This is called "specific adsorption" in which the adsorption is specific to the chemical nature of the ion. This is to be contrasted with "non-specific adsorption" in which the interaction between the metal surface and the hydrated ion is essentially electrostatic, independent of the chemical properties of the ion. Specifically adsorbed species can approach much closer to the metal surface than non-specifically adsorbed ions. The centers of specifically adsorbed ions define the inner Helmholtz plane. Most anions are specifically adsorbed while most cations retain their hydration shells. When the electrostatic potential decreases significantly, the cations can get deposited onto the metal surface, becoming a part of the combine metal (i.e. UPD process, bulk deposition). This process is classified as physisorption, because it involves only charge transfer without formation of strong chemical bonds. Since specific adsorption involves short-range forces, its coverage is usually less than a monolayer, and the actual coverage also depends on the electrostatic potential at the metal surface. Specific adsorption significantly influences the

distribution of electrons at the metal surface through chemical bond, which leads to a change in the effective dipole moment at the metal surface [11,12].

Most of the models discussed so far treat the metal as a classical perfect conductor, a structureless plane wall which is infinitely polarizable. First attempt to incorporate the electronic distribution of metal was made in 1928 with an application of the "Thomas-Fermi model" in the double layer theory [13]. However, this model predicts essentially the same behavior for all metals with far too small values for the interfacial capacity. No significant attempt was made until early 1980's when the "jellium model" was introduced to electrochemistry. The jellium model has been successful in calculating work function of the free metal surface [14]. The combination of the jellium model and the model of electrolyte, the jellium-hard sphere model, shows good agreement with the measured capacities of many metals, but the calculations are possible for only small excess charge on the metal. [15,16].

Significant developments have been made in the double layer theory since the first model was proposed by Helmholtz. The diffuse layer of the metal/electrolyte interface has been reasonably well understood at least in dilute 1:1 electrolytes. However, no adequate treatment of the inner layer exists due to strong chemical interactions between the specifically adsorbed species and the metal surface. One major difficulty in the progress of the double layer theory is the lack of reliable molecular level structural information, especially for the inner layer.

In order to probe molecular level structure of the metal/electrolyte interfaces, many ultrahigh vacuum (UHV) techniques, developed for surface science studies, have been used since early 1980's [17,18,19]. These techniques, based on scattering of electrons or ions, have the required sensitivity to probe the surface but could not be used for wet surfaces due to their short penetration distance. The samples must be emersed from their electrochemical environments and transported

to a vacuum chamber where the measurements are made. While these *ex situ* characterization have provided valuable insights, the possibility that changes in the structure of the adsorbates could occur after the loss of the potential control can not be completely ruled out. The spectroscopic techniques using ultraviolet, visible, or infrared radiation whose wave lengths are larger than the length scale of the metal/electrolyte interfaces have been used successfully for *in situ* studies, providing valuable information on chemical sensitivity, bond types, and orientation of interfacial species. However, these techniques can offer only indirect information about the atomic structures.

In recent years, breakthroughs in obtaining atomic structures of the electrochemical interfaces have been made by scanning tunnel microscopy (STM), atomic-force microscopy (AFM), and X-ray diffraction. These techniques do not require vacuum and can probe the metal/electrolyte interfaces under potential control. Each technique has its unique advantages and limitations.

The principal advantages of X-ray diffraction lie in the weakly interacting nature of X-rays with matter. The weak interaction allows X-rays to penetrate into the electrolyte and probe the interface without interfering the electrochemical environment, permitting perfect potential control during the measurements. STM or AFM requires much more precaution because its tip can interfere with the atoms being probed. The X-ray diffraction can probe not only the surface of the metal, but also the layers underneath the surface and the structure of the electrolyte and even the interfacial roughness. Such information is impossible to obtain with STM or AFM. Since the weak interaction of X-rays with matter allows a kinematic approximation, the analysis is easy and straightforward. The wave length of X-rays is comparable to atomic spacing of the solids (λ=1.46 Å at 8.5 keV), so X-ray diffraction can directly prove crystal structures. X-ray diffraction directly probes the reciprocal space by taking a vast average over the real space. This property of X-ray

diffraction is often considered to be its biggest weakness because the results are not immediately obvious. However, it is also the biggest strength of X-ray diffraction. For example, X-ray diffraction can easily monitor phase transitions or structural changes by monitoring the intensity of only one point in the reciprocal space. Therefore, X-ray diffraction is an ideal tool for kinetic studies. This is a significant advantage because rapid changes of the interfacial structure as a function of the electrode potential can be reliably measured. In addition, the structural sensitivity of X-ray diffraction, usually better than 0.01 Å, is very useful in measuring the strain present in the film. Throughout this thesis, the strengths of X-ray diffraction technique are used to extract the kinds of information on the electrochemical interfaces that are either extremely difficult or simply impossible by any other techniques.

1.2 Copper/electrolyte interface

This thesis work investigates the structure of copper/electrolyte under various conditions. The focus is directed on the structure of the inner part of this double layer. The study of copper/electrolyte interface is important not only because of academic interest but also because of practical interest. So, far most structural studies of electrochemical interfaces have been performed on platinum, gold, and silver electrodes, partly because experiments on these electrodes are much easier than other metals. The surface preparation for these metals are relatively easy, and they have little tendency to oxidize. Although copper is prone to oxidation, oxidation and corrosion on copper can be controlled more easily than on more reactive metals like iron. This makes copper an appealing candidate for the study of oxidation and corrosion.

This thesis work examines three different kinds of copper/electrolyte interfaces. The first system is an electrochemically deposited Pb monolayer on Cu(111). Here, we examine the structure of the Pb monolayer and the structure of the Cu(111) surface influenced by the Pb

overlayer, under thermodynamic equilibrium conditions. The emphasis on this experiment is focused on understanding how the in-plane and the surface normal structures respond to the potential. A fine spatial resolution on the in-plane structure (< 0.01 Å), combined with fast measurement capability of X-ray diffraction, made it possible to study the kinetics of this system Next, we examine the structure of the bare Cu(111) electrode. The emphasis of this experiment is on the structure of the Cu(111) electrode and specifically adsorbed oxo-species on the surface as a function of the potential. Lastly, we examine the growth of bulk oxide on Cu(111). With the *in situ* techniques developed from the previous experiments, the amount of bulk oxide was controlled with the potential. The strain of the epitaxial oxide film as a function of the thickness is investigated. The study of the electrochemical oxidation of Cu(111) exhibited interesting growth kinetics which depended on the crystallographic orientation of the oxide, to be contrasted with the growth kinetics found elsewhere.

1.3 Copper/water system

In order to focus on the details of the copper/aqueous electrolyte interface, a brief discussion on the copper/water system and its equilibrium phases is in order. The copper/water system consist of many different ionic and solid phases, including various oxides and ionic complexes. For illustration purpose, only major phases are shown in Fig. 1-2. The complete phase diagram can be found in Ref. [20]. The phases of copper/water system are defined by the electrochemical reactions and their equilibrium conditions. The electrochemical equilibrium between two phases, $O + ne = X$, is governed by Nernst equation,

$$E = E^0 + \frac{RT}{nF}\ln\frac{a_O}{a_X} \approx E^0 + \frac{RT}{nF}\ln\frac{[O]}{[X]} = E^0 + \frac{2.3RT}{nF}\log_{10}\frac{[O]}{[X]} \qquad (1\text{-}2)$$

where E is the equilibrium potential, E_0 is the equilibrium potential at the standard condition (at 1 atm. at 25 °C and at 1 molar concentration of dissolved species). R is the ideal gas constant, T is temperature, F is Faraday's constant, a_O is the activity of species O, and [O] is the molar concentration of O. In the case where X is solid body, its activity is assumed to be unity, and the above equation is reduced to

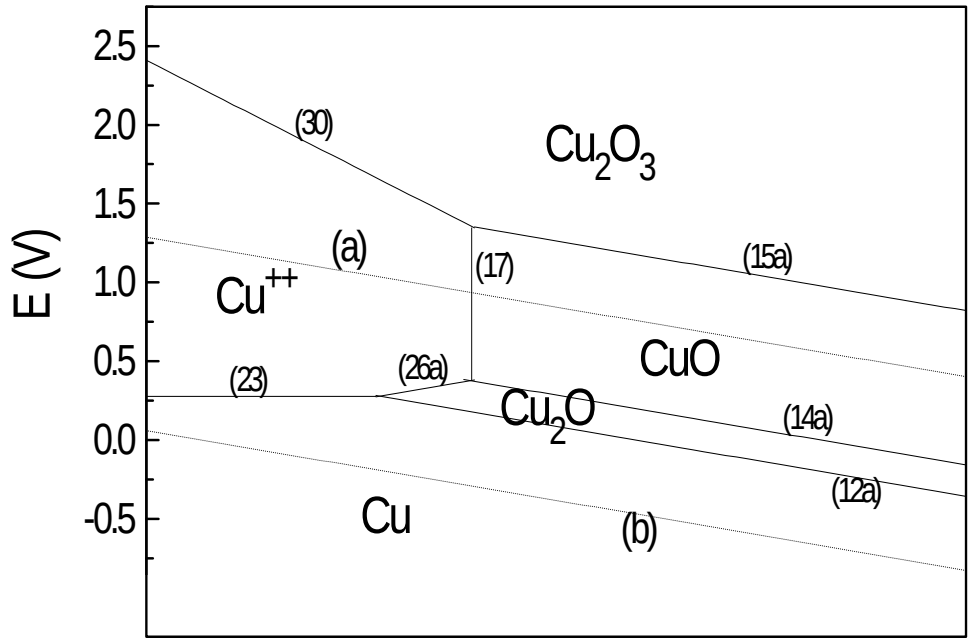

Figure 1-2: Electrochemical phase diagram ("Pourbaix diagram") of the copper/water system at standard condition (under 1 ATM. and at 25° C) as a function of the pH and the potential. For illustration purpose, only Cu, Cu^{++}, Cu_2O, CuO, and Cu_2O_3 phases are shown, and more complex phases such as Cu^{+}, Cu^{+++}, $HCuO_2^{-}$ CuO_2^{--}, CuO_{2-}, Cu(OH), $Cu(OH)_2$ are omitted. The phases are divided by electrochemical equilibrium between phases, and the actual boundaries between the sold and ionic phases (i.e. Cu^{++}) depend on the concentrations of the dissolved species in a simple way predicted by eq (1-1). The electrochemical reaction corresponding to each boundary is listed in Tab. 1-1.

$$E \approx E^0 + \frac{0.0591}{n} \log\ [\mathrm{O}] \qquad (1\text{-}4)$$

when $T = 25$ °C and the potential is in volts. The consequence of Nernst equation is that the equilibrium potential change by 59 mV as the ionic concentration [O] changes by one decade. The phase boundary between Cu and Cu^{++} is determined by this simple version of Nernst equation (see Eq. (23) in Tab. 1-1). At potentials positive to the Nernst equilibrium potential, the reduced species become oxidized, while at potentials negative the Nernst equilibrium potential, the oxidized species become reduced. In the case of metal, this corresponds to dissolution and deposition.

If the electrochemical reaction in question involves break up of water, for example, Eq. (12) in Tab. 1-1, the equilibrium between proton, H^+, and water, H_2O, must be taken into account. To be specific, the equilibrium potential for the reaction, $a\mathrm{A} + c\mathrm{H_2O} + ne = b\mathrm{B} + m\mathrm{H^+}$, is [21]

$$E \approx E^0 - \frac{0.0591m}{n} \mathrm{pH} + \frac{0.0591}{n} \log \frac{[\mathrm{A}]}{[\mathrm{B}]} \qquad (1\text{-}6)$$

Reaction	**Equilibrium locus**	**label**
$2H^+ + 2e = \boldsymbol{H}_2$	$E_{0a} = 0.000 - 0.0591\mathrm{pH} - 0.0295 \log \mathrm{P_{H_2}}$	(a)
$\boldsymbol{O}_2 + 4H^+ + 4e = 2H_2O$	$E_{0b} = 1.228 - 0.0591\mathrm{pH} + 0.0147 \log \mathrm{P_{O_2}}$	(b)
$Cu_2O + 2H^+ + 2e = 2\mathbf{Cu} + H_2O$	$E_0 = 0.471 - 0.0591\mathrm{pH}$	(12)
$2\mathbf{CuO} + 2H^+ + 2e = \mathbf{Cu_2O} + H_2O$	$E_0 = 0.669 - 0.0591\mathrm{pH}$	(14a)
$\mathbf{Cu_2O_3} + 2H^+ + 2e = 2\mathbf{CuO} + H_2O$	$E_0 = 1.648 - 0.0591\mathrm{pH}$	(15a)
$\mathbf{CuO} + 2H^+ = Cu^{++} + H_2O$	$\log [Cu^{++}] = 7.89 - 2\mathrm{pH}$	(17a)
$Cu^{++} + 2e = \mathbf{Cu}$	$E_0 = 0.340 + 0.0295 \log [Cu^{++}]$	(23)
$2Cu^{++} + H_2O + 2e = \mathbf{Cu_2O} + 2H^+$	$E_0 = 0.203 + 0.0591\mathrm{pH} + 0.0591 \log [Cu^{++}]$	(26a)
$\mathbf{Cu_2O_3} + 6H^+ + 2e = 2Cu^{++} + 3H_2O$	$E_0 = 2.114 - 0.1773\mathrm{pH} - 0.0591 \log [Cu^{++}]$	(30)

Table 1-1: Electrochemical reactions and their equilibrium conditions. The potentials are given vs. NHE. The equilibrium loci for the reactions constitute the boundaries of the copper/water phases shown in Fig. 1-2. In (a) and (b), $\mathrm{P_{H_2}}$ and $\mathrm{P_{O_2}}$ partial pressure of H_2 and O_2 in atm.

where pH = -log [H^+]. Eq.1-6 explicitly states how pH of aqueous electrolyte influence the thermodynamics of metal/water system.

Although the phase diagram for the copper/water system extends over 3 V, experiments on this system (also all other metal/water systems) must be performed within the range of the stability of water. At standard conditions, water is stable with two dotted boundaries labeled as "a" and "b", beyond which water begins breaks down into hydrogen and oxygen, respectively. In the pH (adsorption of oxygen or hydroxide), and unstable or metastable phases are need to be explored. range below about 3.5, the copper is stable (as metal) only for a narrow potential window. In higher pH ranges, the copper exists mainly as oxides.[3]

The phase diagram of the copper/water interface shown here is obtained considering only macroscopic thermodynamic reactions, and the phases discussed here are only the stable bulk phases. Microscopic details, such as crystallographic dependence, any possible 2D phases are not considered.

1.4 Electrochemistry vs. surface science

Although study of electrochemical interfaces is often motivated by chemical interests, its significance is by no means limited to the field of electrochemistry. A number of phenomena found

at electrochemical interfaces such as metal deposition, adsorption, and oxidation are equally important in surface science. The use of surface science techniques in probing the atomic structure of the interfaces and application of the theoretical models originally developed in condensed matter

---

[3] In pH region above 13, copper can be directly converted in to ionic phases, $HCuO_2^-$ and CuO_2^-, without formation of oxides or hydroxides. Such phases are not shown in Fig. 2-2.

physics have blurred the traditional boundary between electrochemistry and surface science. Indeed, a number of interesting similarities and parallel mechanisms are found between metal/electrolyte and metal/vacuum interfaces, and some of these are discussed later.

Yet, much more interesting and different phenomena are expected to found in metal/electrolyte interfaces not only because the electrolyte and the specifically adsorbed species influence the kinetics and the details of the structure but also because the interfacial reactions are controlled by different thermodynamic variables. Though still important, temperature and pressure are no longer most influential and interesting thermodynamic variables at most electrochemical interfaces. Much more relevant and crucial variables are potential and pH (in case of corrosion and oxidation of metals). Thus, the study of electrochemical interfaces offers unique opportunities, at least from the traditional surface science point of view, to investigate the thermodynamics at the metal surface with quite different variables and to further our understanding of metal surfaces.

1.5 References

[1] J. O'M. Bockris and A. K. N. Reddy, Modern Electrochemistry (Plenum Press, NewYork, 1970).

[2] H. L. von Helmholtz, Wied. Ann. **7** 337 (1879).

[3] G. Gouy, J. Chim. Phys. **9** 457 (1910).

[4] O. Stern, Z. Elektrochem. **30**, 508 (1924).

[5] J. O.M. Bockris and E. C. Potter, J. Chem. Phys. **20**, 614 (1952).

[6] N. F. Mott and R. J. Watts-Tobin, Electrochim. Acta **4**, 79 (1961).

[7] J. R. Macdonald, J. Chem. Phys. **22**, 1857 (1954).

[8] J. O.M. Bockris, M. A. V. Devanathan, and K. Müller, Proc. Roy. Soc. **A274**, 55 (1963).

[9] R. Guidelli, J. Electroanal. Chem., 123, **59** (1981); *ibid*. **197**, 77 (1986).

[10] G. M. Torrie and G. N. Patey, Electrochim. Acta, **36**, 1677 (1991).

[11] I. Langmuir, J. Amer. Chem. Soc., **54**, 1798 (1932).

[12] W. Lorentz and G. Salié, Z. Phys. Chem. 218, **259** (1961).

[13] O. K. Rice, Phys. Rev. **31**, 105 (1928).

[14] N. D. Lang and W. Kohn, Phys. Rev. B **1** 4555 (1970); ibid. **3**, 1215 (1971).

[15] J. P. Badiali, M. L. Rosinberg, and J. Goodisman, J. Electroanal. Chem. **143**, 73 (1981).

[16] D. Henderson and W. Schmickler, J. Chem. Phys. **82**, 2925 (1985).

[17] A. T. Hubbard, Acc. Chem. Res. **13**, 177 (1980).

[18] P. N. Ross, Surf. Sci. **102**, 463 (1981).

[19] E. Yeager, J. Electroanal. Chem. **128**, 463 (1981).

[20] M. Pourbaix, *Atlas of Electrochemical Equilibria in Aqueous Solutions* (Pergamon, New York, 1966).

[21] M. Pourbaix, *Lectures on Electrochemical Corrosion* (Plenum Press, New York, 1973).

2. Experiment

This chapter is devoted to the details of the experiment, which include cleaning procedures, sample preparation methods, description of the electrochemical x-ray cell, purging procedures, and *in situ* X-ray diffraction procedures. In addition, the background of electropolishing of copper and the protocol for preparing electropolishing solution are discussed.

2.1 Sample rurface preparation methods

The samples are Cu(111) and Cu(100) single crystals (Monocrystal Co.), 0.5" in diameter and 3 mm in thickness. A typical miscut is less than 0.5°. Since experiments are performed in an electrochemical environment outside vacuum, the usual vacuum surface preparation method, sputtering and annealing, is not a convenient way to prepare the sample surface. This method is cumbersome and time-consuming, because the sample has to be transported in and out of the vacuum chamber. Excluding the UHV sample preparation method, there are three ways to prepare the sample surface: flame-annealing, chemical polishing (chemical etching), electropolishing (or electrolytic polishing). Flame-annealing is a quick and easy surface preparation technique used for gold and platinum surfaces. In the flame-annealing surface treatment, the sample surface is heated close to the melting temperature of the metal and cooled. This procedure improves the surface flatness and the crystallinity as well as removing impurities (oxides, organics, etc.). However, some metals such as copper and silver would oxidize of flame-annealed, and chemical methods must be used. Chemical polishing is performed either by pouring a suitable solution over the sample or by immersing the sample in the solution. This method is also quick and convenient but can be quite difficult because the reaction can not be controlled. The chemical polishing tends to leave macroscopically disordered but microscopically flat surface. The detailed discussion on the

chemical polishing of copper and its alloy is found in ref.[1]. The last method is electropolishing. The electropolishing is carried by anodizing the sample surface in an polishing solution. For copper, the electropolishing is the best alternative to the UHV preparation. A successfully electropolished surface typically exhibits a surface mosaic of less than 0.1° and a coherence length better than 500 Å, determined by x-ray diffraction.

2.2 Background on electropolishing

Electropolishing is considered to be a "black art." The reason for such conception is due to irregular electrochemical behavior at the surface during the electropolishing. Since success of experiments depends on preparation of a flat surface by electropolish, a detailed discussion on this subject is in order.

Electropolishing of copper has received much attention due to its practical and academic interests [2,3,4,5]. Despite the considerable experimental and theoretical works, the exact mechanisms responsible for the current limiting behavior during the anodic dissolution of copper, necessary for a successful polish, is unknown. A typical I-V curve of anodic dissolution of copper in phosphoric acid (H_3PO_4) is shown in Fig. 2-1. Different regions of the curve are marked as A, B, C, and D. The data in Fig. 2-1 were obtained with the computer controlled power supply. The small oscillations and steps in the data are due to the finite resolution of the power supply. Strikingly similar current-potential characteristics was also observed by others [2,3,4,5]. The region "A" is the beginning stage of the anodic dissolution, in which the current rises sharply with the potential due to an increasing rate of the conversion of copper metal atoms to copper ion, Cu^{++}. The current density decreases in region B and finally becomes constant in region C. A limited diffusion of the large concentration of Cu^{++} produced at the surface is responsible for decrease and flattening of the current density in region B and C, giving rise to a peak. The shape and the

size of the current peak is determined by the kinetics in the double layer; the peak becomes smaller as the potential is scanned more slowly. After a current plateau, the current sharply rises again. This is due to opening of a new current channel due to evolution of oxygen at the copper surface.

According to direct in *situ* observations of polycrystal copper surface using conventional optical microscope, surface morphologies depended on the dissolution potential [4,5]. Formation of red-brown film on the surface with the sharp grain-boundary pattern was observed in region A. The grain-boundary pattern was attributed to crystallographic etching of the surface. The color indicated that the film was probably composed of cuprous oxide (Cu_2O). A gradual vanishing of the grain structure and a transparent film were observed in region B. Polishing in this region yielded a broad undulating etched surface. The best polishing result was observed in region C, where the current density is constant over the potential. Polishing in region D also yield a bright surface but with pits due to formation of oxygen bubbles. These results were confirmed by the author.

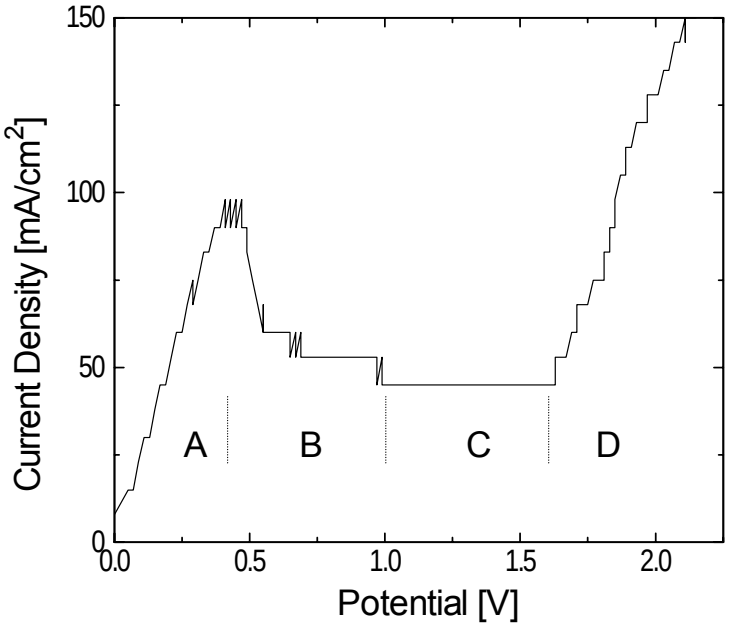

Figure 2-1: Current-potential characteristics of anodic dissolution of copper in 43 % phosphoric acid (H_3PO_4) . Different potential regions A-D are discussed in the text. The potential is vs. copper cathodic plate.

The formation of oxide during the dissolution of copper indicates that the anodic dissolution of copper is not a simple process in which solid copper is directly converted into copper ions [2], but it involves much more complex mechanisms. According to the thermodynamics at copper/water interface [6], formation of bulk oxide is impossible at pH less than 3.5. The observation of oxide in concentrated phosphoric acid (H_3PO_4) indicates that the pH at the surface is significantly larger than the pH of the bulk electrolyte (pH 0.8 at about 40% H_3PO_4). A number of other hypotheses have been presented to explain the dissolution behavior of copper in phosphoric acid, especially the current-limiting behavior which is essential in producing an ideal polish. Some of the proposed mechanisms for the current limiting behavior include involvement of copper-hydroxyl complex [7], copper-phosphate complex [3,8], or water itself [5,8]. Although the exact mechanism is unknown, the evidences indicate that either solid or highly viscous film forms on the copper surface during the anodic dissolution of copper in the current-limiting region [8,9,10,11,12]. The presence of this film was found to be essential in maintaining the current-limiting conditions. Disturbance of the film strongly affected the current density and the polishing outcome [12].

2.3 Electropolishing conditions

There are number of parameters affecting the current density during the electropolishing: polishing solution, polishing potential, viscosity of the solution, stirring condition, and temperature. The result of polishing sensitively depends on the current density. In general, the lower the current density during the polishing, the better polishing result gets. Therefore, the polishing conditions should be set to minimize the current density.

2.3.1 Polishing solution

Although most of the experimental works in the literature have been on copper/phosphoric acid

system, every polishing expert has his own recipe. Some of the popular choices are: phosphoric acid, phosphoric acid with sulfuric acid, phosphoric acid with ethanol, nitric acid with methanol [1]. Here, only the phosphoric acid is discussed.

The limiting-current density depends on the concentration of phosphoric acid. At room temperature, the current density was found to sharply increase with the concentration with its maximum at around 250 g/L (about 14%[1]) and slowly decrease with increasing concentration [13]. At about 1000 g/L (about 55%), the current density was found to be only about 1/6 (about 35 mA/cm^2) of the maximum. Since good polishing results are achieved when the current density is low (below 60 mA/cm^2), the phosphoric acid concentration must be at least above 40% to avoid high current density. However, even when the optimal concentration is used, the current density is often very large (above 100 mA/cm^2). The reason for the large current density has to do with in the viscosity of the polishing solution at the surface during the polishing. This will be discussed section 2.3.3.

2.3.2 Potential

As explained in section 2.2, potential is most important parameter determining the polishing result. Even when all other parameters are at their optimal conditions, wrong polishing potential produces either oxidized or pitted surface. Since the optimal polishing potential tends to depend on the geometry of the polishing setup [15] and the composition of the polishing solution, it iimportant to map out the potential-current relation before the polish. The best polishing region is at the upper part of the current-limiting region just below the onset of gas evolution. When a new polishing solution is prepared, the I-V does not look like the one in Fig. 2-1 (see Fig. 2-3). The

[1] The usual bottle concentration for phosphoric acid is 85%.

reason for this is that the solution is not properly "aged" yet. This will be discussed in the following section.

2.3.3 Viscosity and copper ions

One of the most interesting properties of anodic dissolution of copper is that the viscosity of the electrolyte strongly influence the dissolution behavior. The viscosity increases with the phosphoric acid concentration [3] and the amount of the dissolved copper ions [3,5,11]. This means that the viscosity of the electrolyte at the copper surface during the polishing is much higher than the bulk of the electrolyte, because the concentration of the dissolved copper ions is very large at the surface. The "secret" in preparing a good electropolishing solution lies in how to adjust the concentration of the phosphoric acid and the amount of the dissolved copper ions in the solution so that the limiting current is the least. This is not a trivial task because the solubility of copper decreases with the increasing concentration of phosphoric acid [3]. The dissolved copper ions in the electropolishing solution are important not only because they affect the viscosity of the solution but also they suppress gas evolution at both anodic and cathodic electrodes. This point is illustrated in Fig. 2-3. The data in Fig. 2-3 were collected in different electropolishing solutions with different amount of dissolved copper ions but with the same concentration of phosphoric acid (43%). Solution A was freshly prepared and contained almost no dissolved copper (clear solution). Solution B contains some dissolved copper but was not quite properly "aged". The color of the solution was light blue. Solution C was properly aged and the color of the solution was bright blue. Since copper was anodically dissolved in the solution, the exact

amount of the copper concentrations were not measured. However, the solution C was almost supersaturated with copper ions. The polishing solution preparation method will be discussed in section 2.4. For solution A, the I-V curve lacked a well defined current-limiting region, and the current density was very large (above 300 mA/cm^2). This behavior was due to early gas evolution. Polishing in this solution was unsatisfactory. There is a well-defined current-limiting region for the I-V curve in solution B. However, the width of the current-limiting region is only about 0.5 V because gas evolution occurred at about 0.8 V. Also, the limiting current density was still high. Polishing in the current-limiting region for solution B resulted in an oxidized surface. Solution C produced an ideal I-V curve, characterized by a current peak before the current-limiting region, a wide current-limiting region, and delayed gas evolution. Polishing in the current-limiting region for this solution resulted in a mirror like finish with no pits.

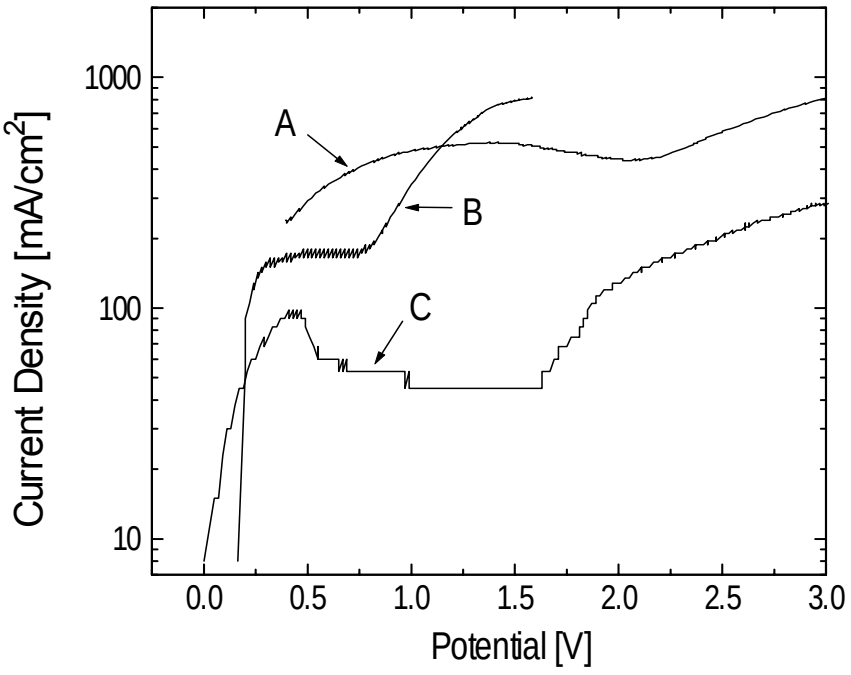

Figure 2-3: I-V curves for electropolishing in different polishing solutions: a freshly prepared solution (A), a somewhat aged solution (B), and a properly aged solution (C). All three solution contains the same amount of phosphoric acid (43%) but different amount of dissolved copper.

Under certain conditions, a peculiar current oscillatory behavior can occurs. The current oscillations were attributed to instability of the double layer during the anodic dissolution of copper, corresponding to formation and breakdown of a viscous film on the copper surface [5]. Current oscillations are shown in Fig. 2-5 and Fig. 2-7. The oscillations occurs usually when the solution is not quite properly aged. No oscillations have been ever seen in a properly aged polishing solution. The polishing accompanied by the current oscillation usually results in an oxidized surface (see Fig. 2-7).

2.3.4 Stirring

Stirring promotes the transport of the dissolved copper ions from the vicinity of the surface to the bulk and increases the limiting current density. The polishing without stirring tends to produce orange-peel like texture on the surface due to local fluctuation of the dissolution rates. However, too much stirring disrupts the formation of viscous film on the copper surface resulting in instability of the system. A gentle stirring (about 60 rpm) is desirable.

2.3.5 Temperature

Temperature was shown to influence polishing results. The relation between the viscosity and the dissolved copper ion was also found to depend on temperature [11]. The electro-polishing at temperatures from 4.5° C to 70° C demonstrated that the limiting current density increases with potential. The results of polish were poor when the temperature was much higher than the room temperature [14].

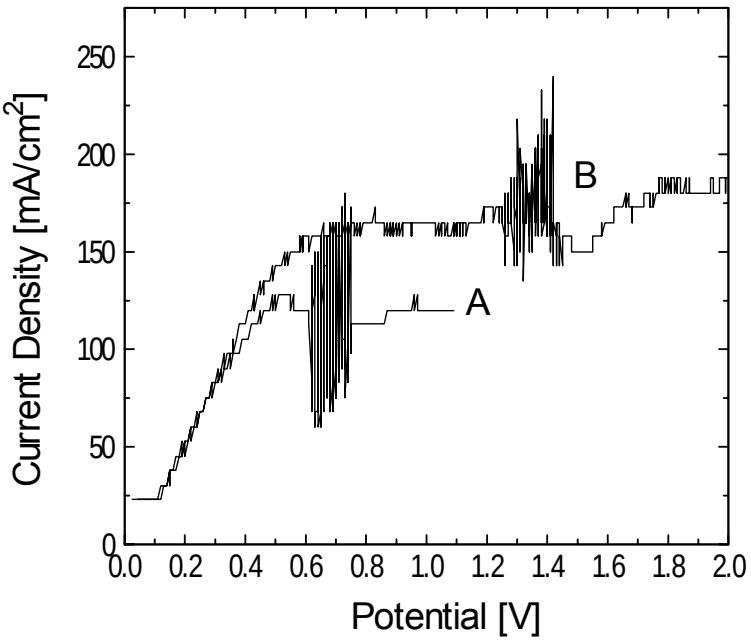

Figure 2-5: Current oscillations. They usually occur as the current decreases toward the limiting current. The oscillation is due to instability of the film formed on the copper surface during the polish.

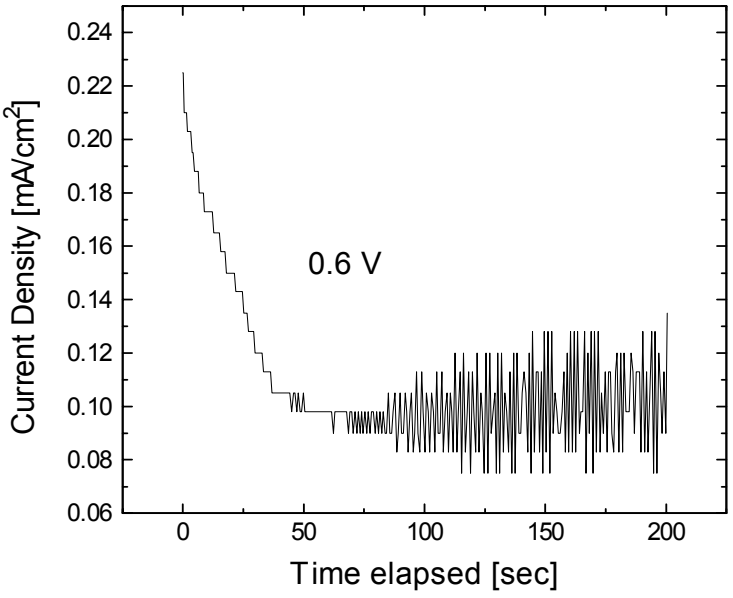

Figure 2-7: The current oscillations started during the polishing at 0.6 V in solution A (see Fig. 2-5). This polish resulted in an oxidized surface.

2.3.6 Preparation of electropolishing solution

In the previous sections, the complexity of the anodic dissolution behavior of copper and the parameters affecting the results of the electropolishing are discussed. . In this section, the details of how to "age" the polishing solution are discussed. The "secret" or "mystery" behind in aging the solution is how to come up with optimal concentration of the dissolved copper ions in the solution.

The polishing solution is prepared first by mixing high purity 85% phosphoric acid and Millipore water with 1:1 ratio by volume. Supersaturation of copper into this solution can be carried out by either a direct dissolution of $CuHPO_4 \cdot H_2O$ or by an anodic dissolution. Unfortunately, $CuHPO_4 \cdot H_2O$ is not a regular stock item for most chemical companies and must be prepared in the lab [5]. The anodic dissolution of copper is carried out by applying about 1 V between the copper anode and the copper cathode plate with slow stirring. The copper anode and cathode must be high purity copper and cleaned thoroughly to avoid possible contamination. After about two or three hours, the solution starts to turn blue and the large amount of brown copper deposit accumulates on the cathode plate. The excess copper deposit should be removed with a clean pipette. The dissolution must continue until the solution turns bright blue. This takes about a few to several hours. As the copper concentration increases, the production of gas becomes noticeable reduced as well as the current density. When properly aged, there should be no gas evolution at potentials between 1-1.5 V, and the steady state current density should be about 30-60 mA/cm^2. A test of the polishing solution should be carried out using a piece of copper with about the same surface area as the crystal, because the polishing results can depend on the geometry [15]. During the aging process, current oscillations can occur as shown in Fig. 2-5 and Fig. 2-7, which is an indication that the solution is not ready. If an ideal I-V curve resembling

Fig. 2-1 is not obtained even after the solution turns into bright blue, the anodic dissolution should be stopped and the solution should be stored in the hood with the copper cathode still in the solution. Nothing more can be done at this stage except to wait. The biggest mystery behind the aging of the polishing solution is that it often requires long waiting period of time (about 2-4 weeks or longer). Although the exact reason for this peculiar phenomenon is unknown, it is possible that the optimal concentration of dissolved copper ions (or some copper complex) may take long time to reach. There are many references to this phenomenon in the literature. A generally accepted practice in preparing a new polishing solution is to add some portion of the already aged solution to the new solution in order to save time [1].

2.4 Electrochemical X-ray cell

The electrochemical X-ray cell used for the experiment is shown in Fig. **2-9**. In order to ensure chemical inertness, the cell was constructed with Teflon. All of its parts, with exception of its X-ray window and O-ring, are also made of Teflon or equivalent materials. It consists of a tapered center collet for holding the sample, a pocket for electrolyte, an X-ray window, and the side ports for inlet/outlet of electrolyte and for electrodes. This cell is similar to the cells used by others [16,17], but it uses a different sample holding method. The sample is inserted from the bottom of the collet and mounted slightly above the cell wall to allow the grazing incident measurements. The sample collet, tapered slightly inward at the end, ensures a tight seal around the crystal. This method of holding sample reduces the background in the voltammetry by eliminating the unwanted current from the side and the bottom of the sample. A 6-μm polypropylene membrane (Chemplex Inc.) is used as an X-ray window and to contain the electrolyte in the cell. An excellent seal is achieved with a tightly fitted ring around the cell with a thin O-ring. The sample collet is designed so that it can be replaced if it becomes too loose to provide a tight seal. To prevent diffusion of

oxygen through the thin membrane, N_2 gas is flushed in the outer plastic bag. A gold or platinum wire (99.999%, Aldrich) is used for the counter electrode. The counter electrode must be long enough (about 5-10 cm) to have a comparable surface area with the sample. The counter electrode was cleaned by flame-annealing just before the experiment. A double junction Ag/AgCl electrode (Micro Electrode Inc.) is used for general purpose. However, for Pb UPD study on Cu(111), a Pb wire (99.999%, Aldrich) was used for the reference electrode in order to make a correct reference to the Pb bulk deposition potential. The oxidized surface of the Pb wire was scraped off with a clean razor blade just before the experiment. The volume occupied by the electrolyte was about 15 mL. The thickness of the electrolyte over the sample can be increased up to several mm's (thick-film geometry) by gently pressurizing the supplying bottle or decreased to the thickness of a capillary layer (thin-film geometry) by partially draining the electrolyte into the draining bottle (Fig. **2-13**). Normally, electrochemical measurements are carried out in the thick-

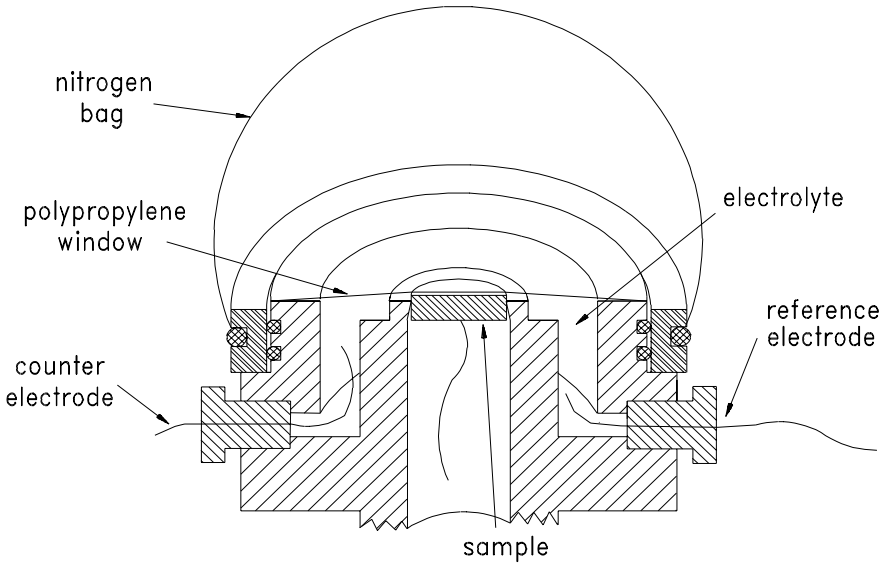

Figure 2-9: Schematic drawing of the electrochemical x-ray cell. A sample is inserted from the bottom and placed slightly above the cell wall. The cell has ports for the reference and counter electrode, as well as for inlet and outlet (not shown). A 6μm-thick polypropylene membrane containing the electrolyte also serves as the x-ray window. In order to prevent oxidation, nitrogen is flushed in a bag over the sample.

film geometry, and X-ray diffraction measurements are carried out in the thin-film geometry.

2.5 Experimental procedures

In this section, details on the experimental procedures is discussed from cleaning glassware to in situ X-ray diffraction measurements.

2.5.1 Glassware cleaning

Proper cleaning is necessary to avoid the problems associated with impurities during the experiment. The first step of the cleaning is an overnight soaking of all the glassware used to prepare solution and the cell including all of its Teflon parts in an acid bath composed of sulfuric acid and peroxide (Nochromix). Care must be taken to make sure that no bubble is trapped in a small openings, especially for valves. After the sulfuric acid bath, they are rinsed with ample amounts of deionized water. Beakers and volumetrics are typically washed 10 times. Since valves are difficult to clean, after careful initial washing, they are repeatedly ultrasonicated under deionized water. After rinsing, the glassware, the cell, and the cell parts are soaked in 6 M nitric acid bath (the usual bottled concentration is 15.73 M). Nitric acid helps remove adsorbed sulfates. After an overnight nitric bath, they are rinsed with Millipore water, followed by a final rinsing with boiling Millipore water. Since tubing is difficult to submerge in the acid baths without trapped air, its interior is cleaned while connected to the supplying bottle assembly (see Fig. **2-13**.) by filling the

tubing with acid and leaving it overnight. Plastic parts and O-rings can not be soaked in acid for long. They are usually soaked only for a few hours in nitric bath and rinsed thoroughly with boiling Millipore water.

2.5.2 Solution preparation

The solutions are prepared with the highest grade of chemicals available. Since copper is sensitive to chloride contamination, the chemicals are chosen based on their trace chloride content. The perchlorate electrolytes were prepare perchloric acid (Ultrex, J. T. Baker Co.) and Millipore water. Other chemicals used for experiments are PbO (99.999%, Aldrich), NaCl (99.999%, Aldrich), and $NaClO_4$ (99.99%, Aldrich).

2.5.3 Sample preparation

The copper single crystal is first mechanically polished using alumina (Buheler). Mechanical polish is usually carried out using 0.3μm alumina powder mixed with water on a microcloth pad (Buheler). If the surface is severely roughened due to bad electropolishing, an extensive polish with 5 μm alumina is required before 0.3 μm alumina can be used. After mechanical polishing, the sample is thoroughly rinsed with either deionized water or Millipore water to remove all the polishing particles. Then, the sample is blow-dried using nitrogen gas for electropolishing. Electropolishing is performed just before the experiment to avoid possible contamination or excessive oxidation. It is carried out in a hanging meniscus geometry as shown in Fig. 2-11. In a properly aged polishing solution, a typical polishing is performed at 1.3 V for 3 minutes with a slow stirring (about 60 rpm). After the electropolish, the sample is thoroughly rinsed with about 500 mL of Millipore water followed by another rinse with about 500 mL of boiling Millipore water. According to XPS and AES studies on the electropolished copper [18], the viscous film formed on the copper surface during the electropolishing is from the polish [9]. After rinsing, the sample is quickly blow-dried with nitrogen to get ready for mounting in the cell.

2.6 Sample mounting and data collection

The polished sample is inserted from the bottom of the cell and mounted slightly higher than the cell wall to allow grazing incident X-ray diffraction measurements. After the sample is completely water soluble. However, a thorough rinsing is required to remove all the residues mounted, the electrical contact to the sample is checked. After putting on the polypropylene membrane, a leak check is made by gently pressurizing the cell with Ar or N_2 gas and monitoring the time to become appreciably deflated. A rupture in the membrane, untightened Teflon screws, or loose sample collet can contribute to unacceptable leak. After all the checks are made, the membrane is removed. Then, the sample is aligned for diffraction measurements using copper bulk Bragg peaks. Meanwhile, the electrolyte is deoxygenated in the supplying bottle by bubbling Ar gas in it (see Fig. **2-13**). It takes about 1 hour to achieve good deoxygenation for 100 mL solution, judging from the features in the voltammetry. After the X-ray alignment, the membrane

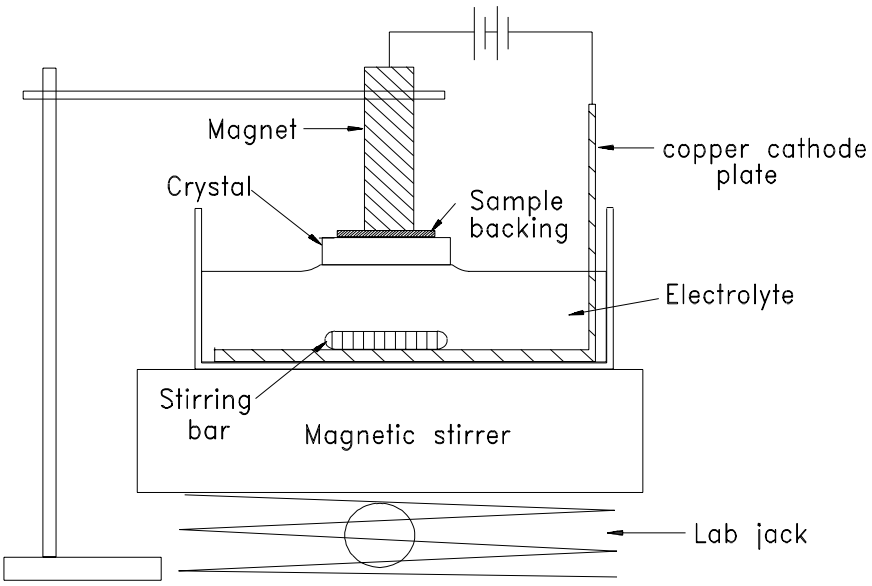

Figure 2-11: Schematic view of electropolishing setup. A sample is polished in a hanging meniscus geometry. A sample backing made of magnetic alloy is attached to the crystal with silver epoxy, allowing an easy mounting to the magnetic sample holder. During the polish, the polishing solution is gently stirred (about 60 rpm).

is put on, all the tubing connections are completed, and the electrical connections to all three electrodes are made. When the double junction Ag/AgCl reference electrode is used for experiment, the reference electrode should not inserted to the cell until this time to avoid a possible drying-out of the ceramic frit. Just before filling the cell with the electrolyte, the cell, tubing, and draining bottle are purged by flowing Ar gas as indicated in Fig. **2-13**. When the cell is filled with the electrolyte, a special care must be taken to remove all the bubbles that are trapped in the corners of the cell. As soon as the filling is completed, the nitrogen bag is put on and the cyclic voltammetric measurements are made except when the cycling is deliberately different, probably due to its native oxide, formed right after the electropolish. Thus, before the X-ray measurements, the potential are kept cycling for about 30 minutes. Over this period of time, the features in the voltammetry are carefully examined by changing the scan rates or the limits of the cycle, in order to check if any unusual features due to contamination are present. After examination of the voltammetric features, the cell is partially deflated to its thin-film geometry, and the sample alignment is quickly checked. Then, the surface quality is checked by measuring the bulk crystal truncation rods (CTR) of the sample. The profile of the CTR peaks are frequently measured during the experiment to keep track of the surface flatness. When the CTR peaks become too weak, the experiment is stopped, the sample is repolished, and the cell is thoroughly cleaned. Usually, two cells are used in turns. While one cell is being used, the other cell is soaked in the nitric bath to get cleaned.

2.7 X-ray diffraction measurement

X-ray diffraction measurements were performed at the National Synchrotron Light Source (NSLS) at beam line X16C. The Synchrotron X-ray was not absolutely needed for some of the experiments in this thesis, for example Pb UPD study on Cu(111), in which the diffraction

intensity from the Pb diffraction peaks were about 20,000-30,000 cts/sec. Such experiment would have been possible using a focused rotating anode X-ray source which is about two orders of magnitude lower in flux. However, using the synchrotron X-ray is much more convenient because the copper surface tends to get either contaminated or roughened after about 24 hours.

The energy of the X-ray beam was usually set at 8.500 keV (λ=1.4585 Å) to avoid copper absorption edge at 8.98 keV. The energy was selected using Si(111) double-crystal monochromator. The X-ray beam produced from the bending magnet was focused with a Saggital focus monochromator down to a size of about 0.5 mm x 2 mm at the focal point and yielded an approximate photon flux of $10^{11}/mm^2/s$. The incident and exit beam of the sample was defined by the vertical parallel slits at 1 mm, and the horizontal exit slit was set at 5 mm. The intensity of the diffracted beam was measured with a NaI scintillation detector. The sample was mounted on a four-circle Kappa diffractometer [19], custom-designed to fit in the small space of the X16C hutch.

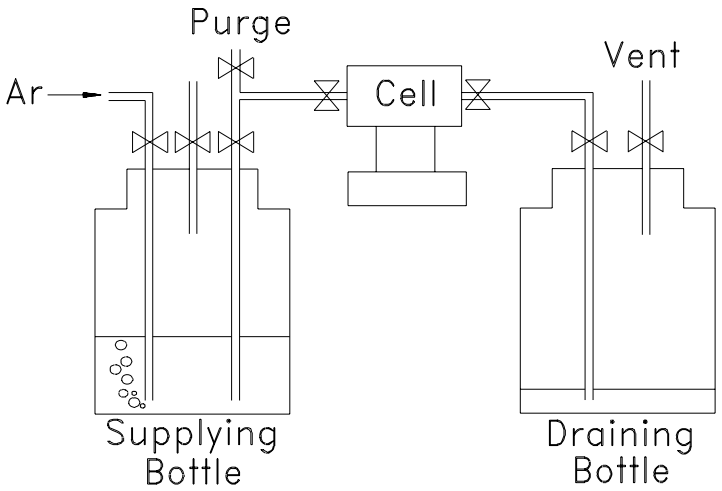

Figure 2-13: Schematic drawing of the experimental set up. The electrolyte is deoxygenated in the supplying bottle by bubbling Ar gas. Before the electrolyte is introduce to the cell, the cell and the tubing are purged with Ar gas. Thickness of the electrolyte over the sample (in the cell) is controlled by varying the amount of electrolyte in the cell.

Throughout this thesis, the coordinates of reciprocal space are indexed using a hexagonal coordinate system which is the convention used in LEED and makes the continuous perpendicular momentum transfer spanned by a single variable. In the hexagonal coordinate system, *H* and *K* describe the projection of the wave vector in the plane of the surface, and *L* alone describes the projection of the wave vector along the surface normal direction, whereas no such simple indexing is possible in the cubic coordinate system. The hexagonal index $(H,K,L)_{hex}$ is related to the cubic index $(h,k,l)_{cubic}$ by the transformation,

$$\begin{pmatrix} H \\ K \\ L \end{pmatrix} = \begin{pmatrix} -1/2 & 1/2 & 0 \\ 0 & -1/2 & 1/2 \\ 1 & 1 & 1 \end{pmatrix} \begin{pmatrix} h \\ k \\ l \end{pmatrix}, \text{ or } \begin{pmatrix} h \\ k \\ l \end{pmatrix} = \begin{pmatrix} -4/3 & -2/3 & 1/3 \\ 2/3 & -2/3 & 1/3 \\ 2/3 & 4/3 & 1/3 \end{pmatrix} \begin{pmatrix} H \\ K \\ L \end{pmatrix} \qquad (2\text{-}2)$$

For example, $(0,0,3)_{hex} = (1,1,1)_{cubic}$, $(-1,0,2)_{hex} = (2,0,0)_{cubic}$, $(1,0,4)_{hex} = (0,2,2)_{cubic}$. The in-plane diffraction measurements were usually performed at L = 0.2, corresponding to a grazing incident angle of about 1.3°, in order to avoid the background from the bulk. The measurements at lower *L* values was not practical because of the large X-ray absorption in the electrolyte at low angles. Unless otherwise specified, the *L* is assumed to be 0.2 and only (*H, K*) reciprocal coordinates will be given in the rest of the thesis.

2.8 Potential control

Potential control method for three terminal cell is shown in Fig. 2-15. Fig. 2-15 shows the potentiostatic method in which the potential between the working (sample) and reference electrodes is the controlled while the current flow between the working and counter electrode is measured. In the alternate galvanostatic method, the current between the working and counter electrodes is controlled while the potential between the working and reference electrode is measured. In a electrochemical cell, the potential of the working electrode is grounded to the

reference electrode not to the ground of the power line. The ground of the power line is not a suitable reference because it is not electrochemically defined. In order to control the electrode potential, it must be referenced to a well-defined electrochemical process. A reference electrode contains electrochemical interfaces at which the reference process takes places. Some of the commonly used reference processes are

$2H^+ + 2e = H_2$ (at Pt surface)	0.000 V	normal hydrogen electrode (NHE)
$Hg_2Cl_2 + 2e = 2Hg + 2Cl^-$ (sat'd KCl)	0.242 V	saturated calomel electrode (SCE)
$AgCl + e = Ag + Cl^-$ (sat'd KCl)	0.191 V	Ag/AgCl electrode

where the potentials are vs. NHE.

2.9 Simple electrochemical techniques

In this section, a few basic electrochemical techniques are illustrated. In order to illustrate these

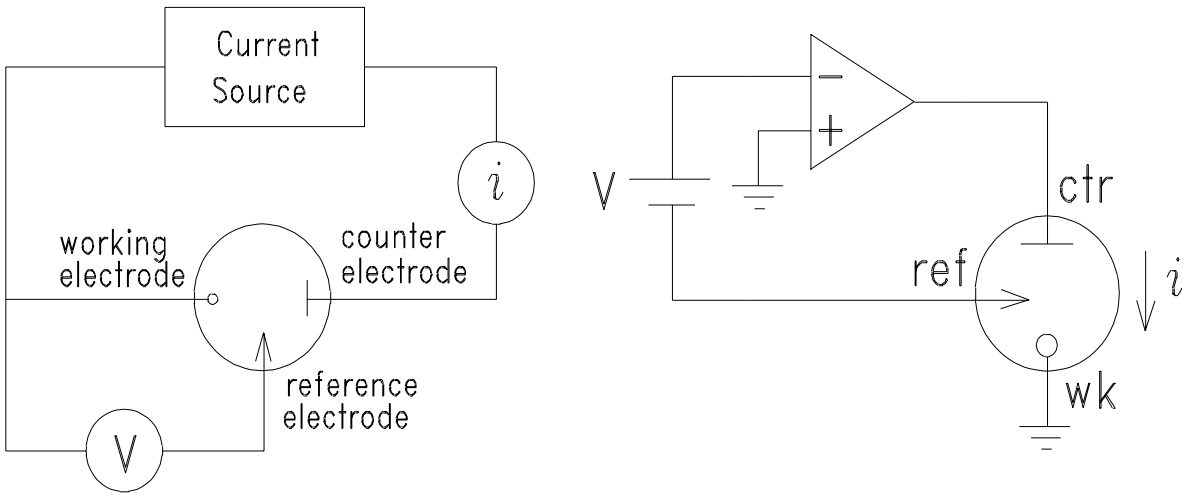

Figure 2-15: Schematic representation of the potential control for three-terminal cell. Feed-back control is used to maintain the desired potential difference between the working (sample) and reference electrode while the current passed between the working and counter electrode is measured.

techniques, it is useful to approximate electrochemical interface with the equivalent circuit. The electrified interface can be represented with a capacitor and a resistor connected in parallel, in which the capacitance and the resistance are function of the potential as shown in Fig. 2-17. The capacitance of the interface depends sensitively to type and extent of adsorption on the electrode, while the resistance reflects extent of Faradaic process (i.e. current flow across the interface *via.* bulk deposition/dissolution or bulk oxidation/reduction, instead of simple "charging up" of the double layer *via.* adsorption). The interfaces, in which no current flow across the interface occurs, can be modeled by the equivalent circuit with $R \rightarrow \infty$, while those with large Faradaic process can be approximated with $R \rightarrow 0$. In most interfaces, the capacitance and the resistance are function of potential, and their potential dependence can be probed using macroscopic electrochemical techniques. Fig. 2-19 shows some of the basic methods. The first three methods investigate the transient responses of interfaces, which depend sensitively on the nature and extent of adsorption at the interface. Cyclic voltammetry, the fourth method in Fig. 2-19, measures steady state

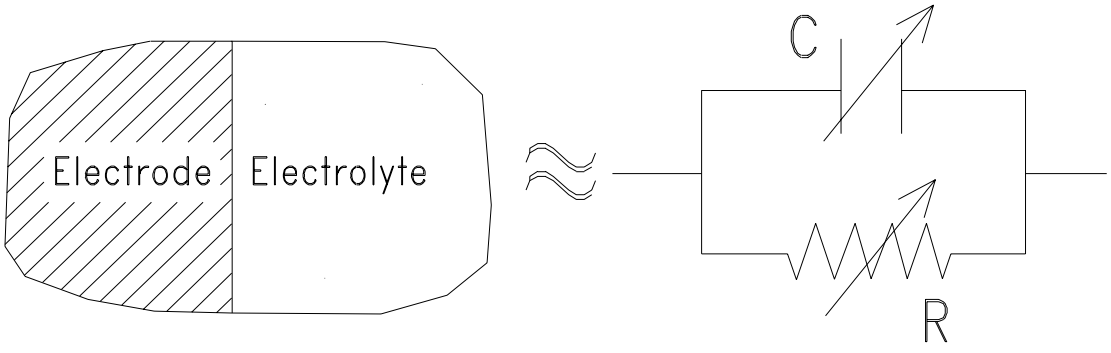

Figure 2-17: The electrified interface can be approximated with a simple circuit with a variable capacitor and a variable resistor connected in parallel.

current response as a function of potential. It measures the electrochemical "spectrum" of the interface and is useful to study the potential dependence of electrochemical reactions. Since the spectrum can be measured in two different potential scan directions, it is useful to study the reversibility of system, especially suited for deposition/dissolution or oxidation/reduction processes. CV is used extensively in conduction with X-ray diffraction to study the electrochemical interfaces throughout this thesis, and its analysis methods are discussed in later chapters. More detailed discussion on the electrochemical techniques can be found in Ref. [20]

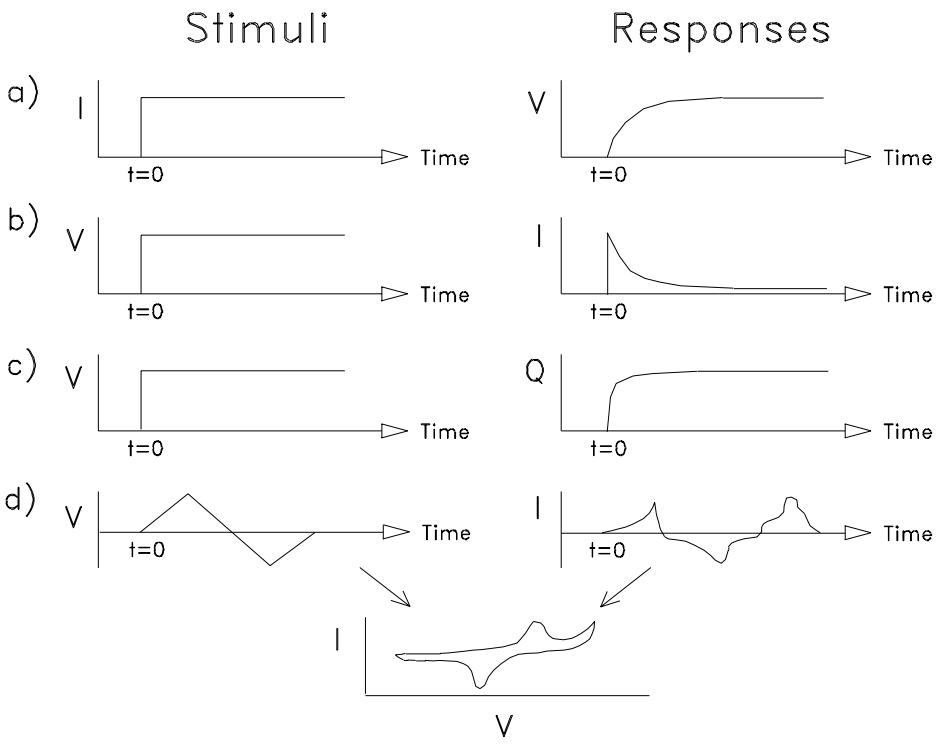

Figure 2-19: Basic electrochemical techniques: a) current step method, b) potential step method, c) coulometric measurement, and d) potential sweep method, cyclic voltammetry (CV), or linear sweep voltammetry (LSV).

2.10 References

[1] H. Leidheiser, Jr., *The corrosion of copper, tin, and their alloys* (John Wiley and Sons, Inc., New York, 1971).

[2] W. C. Elmore, J. Appl. Phys., 10, 724 (1939); *ibid.*, **11**, 797 (1940).

[3] J. Edwards, J. Electrochem. Soc., **100**, 189C (1953).

[4] K. F. Lorking, Electrochim. Acta., **7**, 101 (1962).

[5] S. H. Glarum, and J. H. Marshall, J. Electrochem. Soc., **132**, 2872 (1985); *ibid.*, **132**, 2878 (1985).

[6] M. Pourbais, Atlas of *Electrochemical Equilibria in Aqueous Solutions* (Pergamon, New York, 1966).

[7] D. Laforgue-Kantzer, J. Chim. Phys. **52**, 163 (1955).

[8] M-C. Petit, Electrochim. Acta. 18, 217 (1963).

[9] N. H. Simpson and N. Hackerman, J. Electrochem. Soc. **102**, 660 (1955).

[10] T. P. Hoar and T. N. Farthing, Nature, **169**, 324 (1952).

[11] H. F. Walton, J. Electrochem. Soc. **97**, 219 (1950).

[12] L. C. F. Blackman and R. Wall, Nature, **202**, 285 (1964).

[13] A. Hickling and J. K. Higgins, Trans. Inst. Metal Finishing, **29**, 274 (1953).

[14] R. W. K. Honeycombe and R. R. Hughan, J. Council Sci. Ind. Res. Australia, **20**, 297 (1947).

[15] M. Naruse and A. Nannichi, Technol. Repts. Tohoku Univ. 22, 29 (1957).

[16] M. Samant, M. Toney, G. Borges, L. Blum, and O. Melroy, J. Phys. Chem. 92, 220 (1988).

[17] B. M. Ocko et. al., Phys. Rev. Lett. 65, 1466 (1990).

[18] J. L. Fang and N. J. Wu, J. Appl. Electrochem. **20**, 231 (1990).

[19] I. K. Robinson, H. Graafsma, A. Kvick, and J. Linderholm, Review of Scientific Instruments

66, 1765 (1995).

[20] A. Bard and L. R. Faulkner, *Electrochemical Methods* (John Wiley & Sons, Inc, New York, 1980).

3. Properties of UPD Pb Monolayer on Cu(111).

In the first sets of experiment on the electrochemical interface of copper, the structural properties of electrochemically deposited Pb monolayer on Cu(111) were studied. In this study, the structure of the Pb monolayer and the Cu(111) substrate was studied as a function of the interfacial potential.

3.1 Introduction

As more powerful and sophisticated modern surface science techniques become available, *in situ* measurements of the structure of the electrode/electrolyte interface on an atomic level have become possible. The microscopic structural information available with these techniques can provide better understanding of the atomic-level electrochemical processes that are often strongly influenced by the interface structure. One area of active research is the structure of metal monolayers on the electrode surface deposited through the underpotential deposition (UPD) process. UPD is the electrochemical deposition of foreign metals onto substrates at potentials positive relative to the reversible Nernst potential for bulk deposition [1]. The formation of a stable overlayer before the bulk deposition potential is possible because the adatom-substrate bond is thermodynamically more favorable to the adatom-adatom bond. For this reason, UPD is usually limited to a monolayer in extent, and the resulting structure of the UPD adlayer is strongly influenced by the substrate. The UPD process is an important subject in electrochemistry because of its unique thermodynamic, kinetic, structural and catalytic properties [2]. In addition to its electrochemical importance, the UPD monolayer is fundamentally significant because it closely resembles an ideal two-dimensional metal under thermodynamic equilibrium conditions. Moreover, since electrochemical conditions are in thermodynamic

equilibrium with a reservoir of ions, conditions which are difficult to obtain in the UHV environment, the UPD monolayer is the only practical candidate to study the properties of a two dimensional metal, within the grand canonical ensemble. Many examples of UPD systems are listed in Tab. 3-2. The underpotential shift, ΔE_p, is the potential at which UPD occurs with respect to Nernst potential. The magnitude of ΔE_p is often interpreted as the difference in the bond energies of adsorbate-substrate and adsorbate-adsorbate. It has been shown that the bond energy is dependent on the work function difference between the substrate and the adsorbate ($\Delta\Phi = \Phi_{sub} - \Phi_{ads}$), and ΔE_p is correlated with the work function difference in the following fashion [3],

$$\Delta E_p = \alpha \Delta\Phi \qquad (3\text{-}2)$$

where $\alpha = 0.5$ V/eV. Only three pairs out of 31 systems listed in Tab3-2 deviate from this empirical correlation, which are Hg, Ag, and Tl on Au. Therefore, UPD is possible only if the work function of the substrate is larger than the work function of the adsorbate.

In this work, we examine the structure of Pb UPD monolayer on Cu(111) with *in situ* X-ray diffraction. Although the structures of many UPD systems have been explored previously, most of these works examined only three substrates, gold, silver, and platinum. There are only a small number of reports on structure of UPD systems on Cu surface [4,5]. The main challenges in performing atomic resolution experiment with copper lie in the difficulties of preparing a clean and smooth surface and keeping it free of oxidation and contaminants for an extended period of time required by data acquisition (several hours for X-ray diffraction). In particular, the requirement on the surface quality is more stringent for spatially averaging probes like X-ray diffraction than for local probes. Our work demonstrates the feasibility that X-ray diffraction can be used to probe the electrochemical interface of copper.

Adsorbate/Substrate	Supporting Electrolyte	ΔE_p (V)
Ag/Pt	0.5M H_2SO_4	0.44
Cu/Pt	0.5M H_2SO_4	0.41
Hg/Pt	0.5M H_2SO_4	0.47
Pb/Pt	1M $HClO_4$	0.87
Bi/Pt	0.12M $HClO_4$	0.59
Cd/Pt	1M $HClO_4$	0.96
Tl/Pt	1M $HClO_4$	~1.3
Sb/Pt	1N H_2SO_4	0.64
As/Pt	1N H_2SO_4	~0.75
Ge/Pt	1N H_2SO_4	~0.40
Ag/Pd	0.5M $NaClO_4$ (pH 2)	~0.30
Cu/Pd	0.5M $NaClO_4$ (pH 2)	0.23
Ag/Au	0.5M H_2SO_4	0.51
Cu/Au	0.5M Na_2SO_4 (pH 3)	0.22
Cd/Au	0.5M Na_2SO_4 (pH 3)	0.51
Tl/Au	0.5M Na_2SO_4 (pH 3)	0.69
Pb/Au	1M $NaClO_4$ (pH 3)	0.40
Hg/Au	0.5M H_2SO_4	0.43
Bi/Au	0.12M $HClO_4$	0.25
Zn/Au	1M Na_2SO_4	0.59
Cu/Ag	0.5M H_2SO_4	0
Cd/Ag	1M Na_2SO_4 (pH 3)	0.16
Tl/Ag	1M Na_2SO_4 (pH 3)	0.28
Pb/Ag	1M $NaClO_4$ (pH 3)	0.16
Bi/Ag	0.5M $HClO_4$	0.06
Sn/Ag	0.5M $NaClO_4$	0.21
Zn/Ag	1M Na_2SO_4	0.13
Cd/Cu	1M Na_2SO_4	0.23
Tl/Cu	1M Na_2SO_4	0.34
Pb/Cu	0.5M $NaClO_4$ (pH 2)	0.20
Tl/Sn	0.5M $HClO_4$ + 0.5M NH_4ClO_4	0.08

Table 3-2: Previously reported UPD systems. The UPD occurs at ΔEp above the Nernst potential. The underpotential shift, ΔEp, has been empirically shown to related to the work function difference between the adsorbate metal and the substrate

The Pb UPD process on Cu(111) is known to exhibit a complex and irreversible behavior. The voltammetric features were found to depend strongly on the pH of the electrolyte, the prepolarization history, and the types of anions present in the electrolyte [6,7] Especially, strongly adsorbing anions such as chloride (Cl^-) or acetate (CH_3COOH^-) were reported to affect the kinetics of the UPD process [7,8]. These complicated behaviors generated the hypothesis that the Pb UPD process on Cu(111) might be interfered by simultaneous adsorption/desorption of either oxygen-containing species like hydroxide (OH^-) [6,7] or chloride present as a trace impurity in the electrolyte [8]. *In situ* X-ray standing wave measurements revealed that the layer spacing of the UPD Pb/Cu(111) system changed with the potential. Based on the these measurements and some assumptions about the Pb in-plane structure, a model was proposed that oxygen might be incorporated underneath the Pb layer [5]. Here, we try to address some of these questions by examining both in-plane and surface normal structures. Also, we investigate the relationship between the kinetic effects with structure, particularly focusing on the effects of chloride on the structure and the properties of the Pb monolayer.

One fundamentally interesting aspect of the Pb monolayer on Cu(111) is that this system is an archetype of large adatoms on a small substrate. In a system of small adatoms on a large substrate atom, the substrate has a strong influence on the structure of the adlayer, often resulting in a commensurate adlayer structure. However, the substrate influence is weaker for the larger adatoms because the intra-layer contacts become important instead, and the resulting structure of the adlayer is often incommensurate. A theoretically interesting case is when the adlayer is rotated with respect to the orientation of the substrate in order to relieve the interfacial strain due to the mismatch of the lattice parameters [9]. In the systems like Pb/Ag(111) [10], Pb/Au(111) [10], Tl/Ag(111) [10], and Tl/Au(111) [10,11], in which the adatoms are larger than the substrate spacing by about 19-21%, the incommensurate adlayers were found rotated by a few degrees. It is

interesting to see if a similar rotation exists for Pb/Cu(111) in which the lattice mismatch is even larger (about 37%). There are some differences in the findings for the structure of evaporated Pb films on Cu(111) in vacuum [12,13,14], and the differences may be due to the different levels of accuracy in the measurements or non-equilibrium behavior at the interface. Here we examine the structure of Pb/Cu(111) under thermodynamic equilibrium conditions as a function of electrode potential.

For many electrochemically adsorbed layers [10,11,15,16], the nearest neighbor spacing changes with the electrode potential. As the electrode potential decreases, the Fermi level for the electrons in the working electrode (sample) increases, leading to the reduction of more metal ions and their incorporation into the UPD layer as neutral atoms. To accommodate a greater number of adatoms on the surface, the lateral spacing of the UPD monolayer must compress. We will closely examine the compression behavior of the Pb monolayer on Cu(111) and compare it with the expected behavior of the corresponding ideal 2D electron gas.

3.2 Experiment

The Cu(111) single crystal sample was prepared as described in section 2.4. A gold wire (99.999 %, Aldrich) was used for the counter electrode, and a lead wire (99.999 %, Aldrich) was used for the reference electrode, in order to make a correct reference to the Pb bulk deposition potential. The electrolyte consisted with 0.1 M \hcl (Ultrex by J. T. Baker and Millipore water) and 5 mM PbO (99.999 %, Aldrich).

Surface X-ray diffraction measurements were performed at the National Synchrotron Light Source (NSLS) at beam line X16C. The energy of the X-ray beam was 8.50 keV (λ=1.459 Å). The in-plane diffraction measurements were performed at L = 0.2, corresponding to a grazing incident angle of about 1.3°, in order to avoid the background from the bulk. The measurements

at lower L values were not practical because of absorption in the electrolyte at very small grazing angles. Unless otherwise specified, $L = 0.2$ is assumed, and only (H, K) reciprocal coordinates will be given from this point on. See section 2.4 for more details.

3.3 Results

3.3.1 Voltammetry

Cyclic voltammetry from the electropolished Cu(111) sample obtained under various conditions are shown in Fig. 3-2. These voltammograms were measured with a scan rate of 10 mV/s in the X-ray cell prior to the X-ray measurements. Voltammogram, "A", was obtained 10 minutes after the cell was filled with the electrolyte consisting of 0.1 M $HClO_4$ and 5 mM PbO. Voltammogram, "B" was taken about 11 hours later in the same electrolyte. During these 11 hours, the X-ray measurements had been performed, requiring extensive cycling of the potential and a number of 30 to 60 minute-long polarizations with a fully formed Pb monolayer coverage. Voltammogram, "C", was taken after introducing a small amount of chloride (0.4 mM NaCl) in the system. In these voltammograms, the current density ($\mu A/cm^2$) is plotted against the electrode potential referenced vs. the bulk deposition potential of Pb (Nernst potential), which is about -0.460 V *vs.* SCE (saturated calomel electrode) at this Pb concentration. There are two prominent peaks, one in each scan direction. The cathodic (negative current) peak corresponds to deposition of one Pb monolayer on the Cu(111) surface, while the anodic (positive current) peak corresponds to stripping of the deposited Pb monolayer. In all three voltammograms, the deposition and stripping do not occur at the same potential; the stripping occurs always at a higher

potential. This potential separation of the deposition peak and stripping peak is due to irreversibility and slow kinetics associated with deposition/stripping of the Pb UPD layer, and the size of separation increases with the potential scan rate [7,8]. Similar irreversibility was also observed in the Pb UPD process on other substrates [10]. This question of irreversibility will be discussed later in detail.

After 11 hours' potential cycling and polarizations, the voltammetric response changed somewhat; the peaks changed their position slightly and their width became much broader. The broadening of the peaks is probably due to roughening of the copper surface, and the change in voltammetric features due to extended polarizations are consistent with the findings of Sigenthaler et. al. [6]. Upon addition of 0.4 mM chloride in the system, dramatic changes both in the position and shape of the peaks occurred. The peaks became sharper, the peak current densities increased

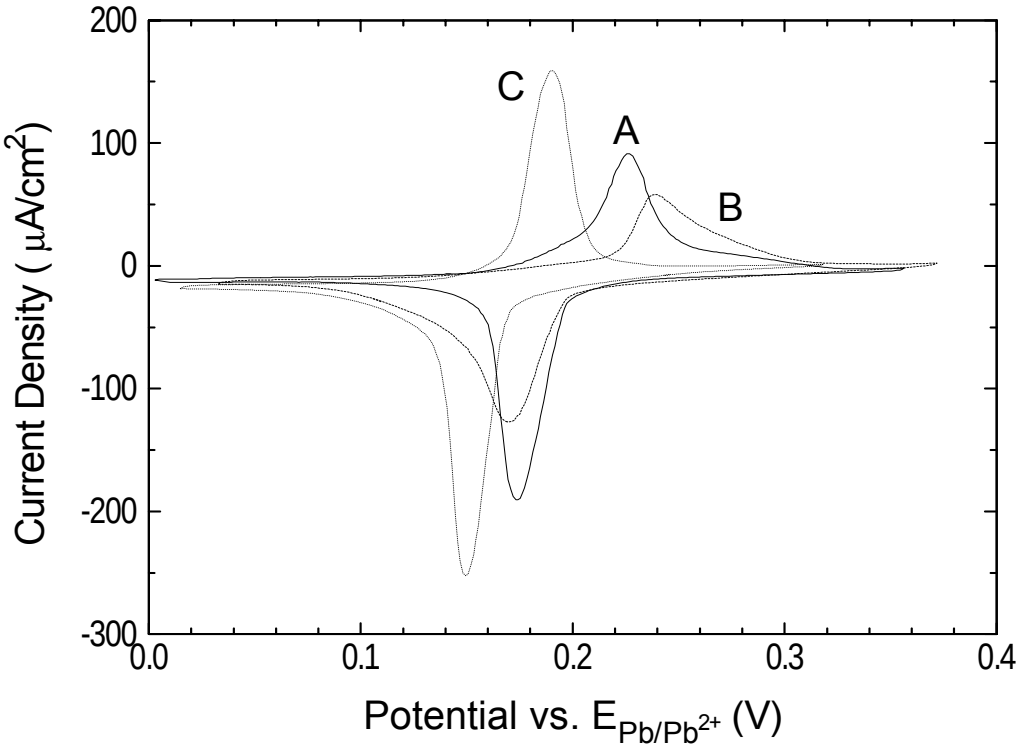

Figure 3-2: Voltammetric responses of Pb UPD on Cu(111) under various conditions; 10 minutes after filling the cell with 0.1 M $HClO_4$ + 5 mM PbO ("A"), 11 hours after the fill ("B"), and after 0.4 mM NaCl was added ("C"). All voltammograms were taken at 10 mV/s.

significantly, and the potential separation between the two peaks became narrower. In addition, both the deposition and stripping peaks were shifted to more negative potentials. Such change in voltammetric response was also reported by Vilche et. al. [7] and Brisard et. al. [8]. Although our voltammograms are in good agreements with those of Siegenthaler et. al. and Vilche et. al., they are not in good agreement with Brisard et. al. in that our voltammograms obtained in the chloride-free electrolyte are similar to their voltammogram obtained in the electrolyte with a small amount of chloride. Therefore, in spite of all our precautions, it is possible that our chloride-free electrolyte might contain a trace amount of chloride.

3.3.2 In-plane structure

Grazing incident angle X-ray diffraction measurements were performed to determine the structure of the underpotentially deposited Pb monolayer on Cu(111) surface. Intense surface diffraction peaks (about 20,000 cts/sec) with a small mosaic spread (about 0.5°) indicated a well-ordered Pb overlayer. Throughout the entire UPD potential range, the main diffraction peaks were found at (x, 0) and (0, x), where the value for x ranged between 0.741 and 0.754 depending on the electrode potential. Weaker but pronounced higher-order peaks were also found at (x, x), (2x, 0), (2x, 2x), and (3x, 0). Diffraction peaks were found also at all other symmetrically equivalent positions. The pattern of the Pb diffraction peaks is consistent with an incommensurate close-packed hexagonal structure which is aligned exactly with the Cu(111) substrate. The model of the in-plane structure of the Pb UPD monolayer, probed by grazing incident angle X-ray diffraction measurements, is shown in Fig. 3-4. This model is in accord with the structure of Pb UPD on Cu(111) determined by *in situ* AFM measurements[17].

Throughout the entire potential range where the Pb monolayer is stable (i.e. between the bulk deposition potential and stripping potential), the Pb monolayer exhibited only the incommensurate

close-packed hexagonal structure. However, the lateral nearest-neighbor spacing showed a significant potential dependence. The in-plane Pb diffraction peaks scanned along the (10)-direction (radial direction) and the ($\bar{1}2$)-direction (transverse direction) at different electrode potentials are displayed in Fig. 3-6a. and Fig. 3-6b, respectively. The position of the diffraction peak scanned along the transverse direction (Fig. 3-6a) remained at $K = 0$, as the potential changed from 0.180 V to 0.005 V relative to the bulk deposition potential. If the Pb monolayer were rotated with respect to the substrate, there would be two orientational domains, and the transverse scan would have therefore revealed two symmetric peaks separated equally from the origin. Thus, the change in the electrode potential did not affect the alignment of the Pb monolayer with the substrate. However, narrowing of the transverse peaks suggests that the ordering of the Pb monolayer increased with decreasing potential. Unlike the transverse scans,

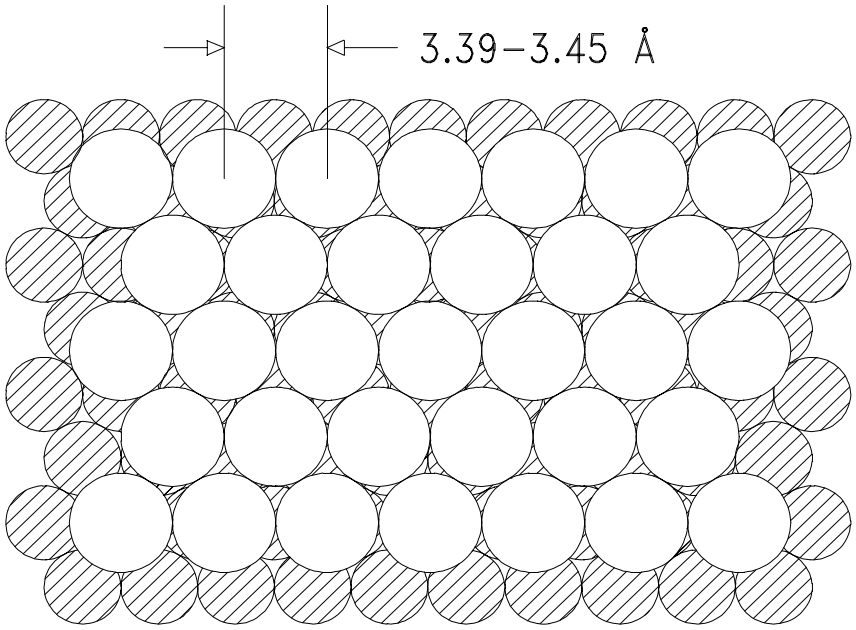

Figure 3-4: Proposed model for the structure of Pb UPD monolayer on Cu(111). The small hatched circles represent the Cu(111) substrate atoms while the larger open circles represent the Pb adatoms in the unrotated incommensurate hexagonal structure. The spacing of the Pb monolayer varies from about 3.45 Å to 3.39 Å depending on the electrode potential.

the radial scans (Fig. 3-6b) do show shifting of peak position with potential. As the potential decreased from 0.180 V to 0.005 V, the radial peak position in H. changed from 0.741 to 0.754. The nearest neighbor spacing for the Pb monolayer can be obtained from the radial peak position, H, with the relation, $a_{Pb} = a_{Cu}/H$, where the nearest-neighbor spacing for Cu(111), a_{Cu}, is 2.556 Å. Therefore, the change in the peak position from 0.741 to 0.754 translates into a change in the nearest-neighbor spacing for the Pb monolayer from 3.448 to 3.392 Å.

Consequently, the Pb coverage, θ ($= (a_{Cu}/a_{Pb})^2 = H^2$), has increased from 0.550 to 0.568 in units of monolayer of Cu(111).

The measured in-plane spacing of the Pb monolayer as a function of the electrode potential is shown in Fig. 3-8. The data represented by solid triangles were obtained in the chloride-free electrolyte (0.1 M $HClO_4$ + 5 mM PbO), and the data represented by hollow triangles in the chloride-containing electrolyte (0.1 M $HClO_4$ + 5 mM PbO + 0.4 mM NaCl). Each data point was obtained from the diffraction peak position along the radial direction. As observed for most electrochemically deposited overlayers [10,11,15,16,18], the nearest neighbor spacing of Pb UPD monolayer on Cu(111) changes linearly with the electrode potential. One remarkable difference in our case, however, is a large hysteresis; the Pb nearest-neighbor spacing is always smaller during the anodic scan (increasing potential). The hysteresis is probably due to a slow kinetics associated with reaching the electrochemical equilibrium and the formation of an ordered Pb layer as confirmed by the observations: i) at a fixed potential, the Pb spacing was found to change slowly with time, and ii) the observed Pb spacing was found to depend also on such factors as the potential scan rate and the electrolyte film thickness. In order to reduce the fluctuation of data due to the hysteresis, a careful procedure was adopted. The initial potential for the measurements

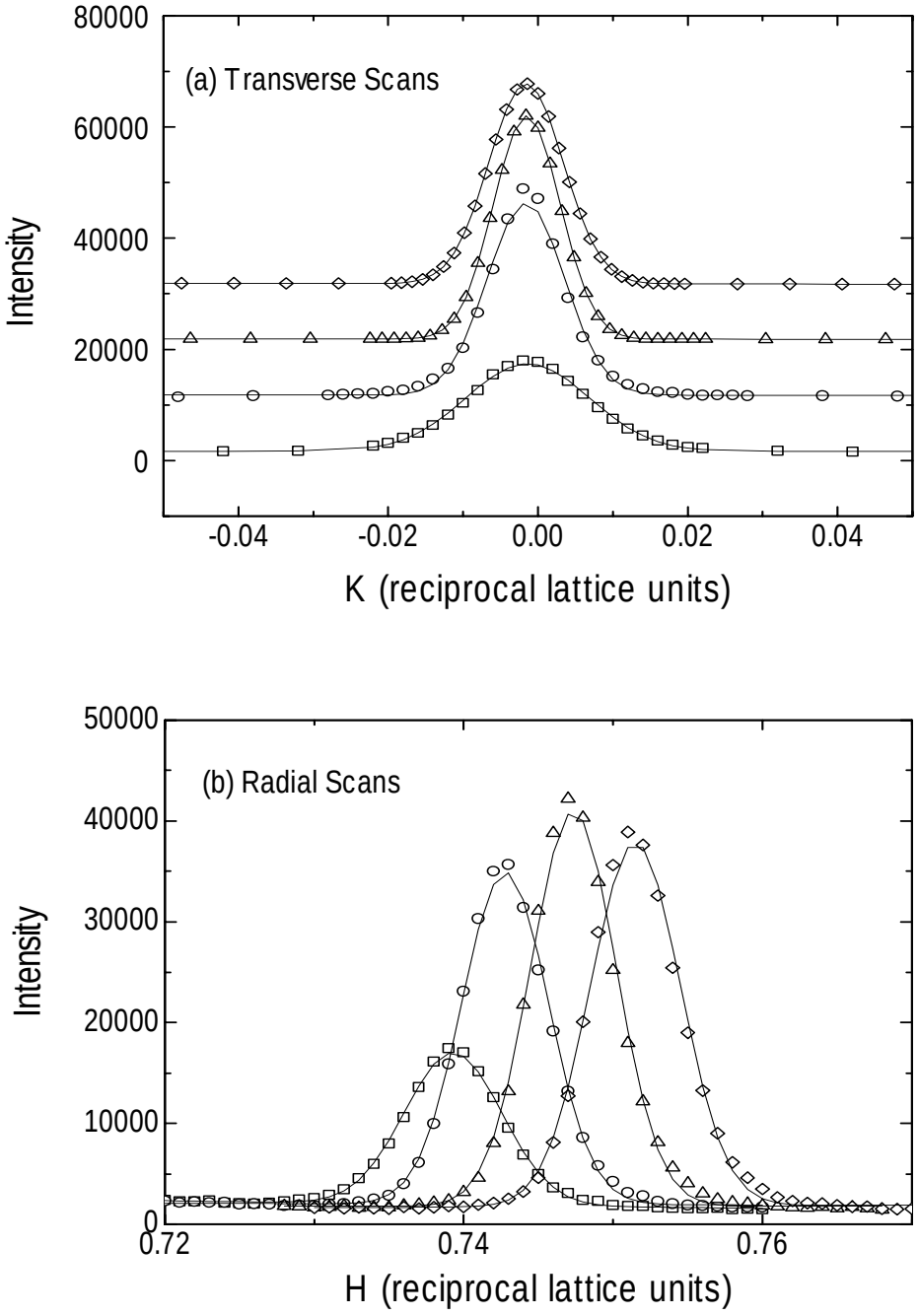

Figure 3-6: Profiles of the first order Pb diffraction peaks at various electrode potentials; transverse (a) and radial (b) scans; 0.180 V (squares), 0.120 V (circles), 0.060 V (triangles), and 0.005 V (diamonds). The transverse scans are shifted vertically for better viewing. The solid lines are the Gaussian fits to the data.

was always near the cathodic peak potential. After the potential was set at the desired value, a fixed interval of time was allowed to pass before the membrane was deflated to the thin-film geometry for X-ray measurements, and an almost equal amount of time was used to collect data at each potential. After the measurements, the membrane was restored to the thick- film geometry, and the potential was scanned down to the next desired value at a rate of 1 mV/s. This procedure was repeated until the potential reached 5 mV above the Pb bulk deposition potential. Then, the direction of potential scan was reversed, and the same procedure was repeated. The data shown in Fig. 3-8 were obtained with a three-minute waiting interval before deflating the membrane. Although a lower scan rate and a longer waiting interval decreased the magnitude of the hysteresis, it still persisted even when 0.1 mV/s scan rate and 30 minute waiting interval were employed. The scan rate of 1mV/s and waiting interval of 1 minutes

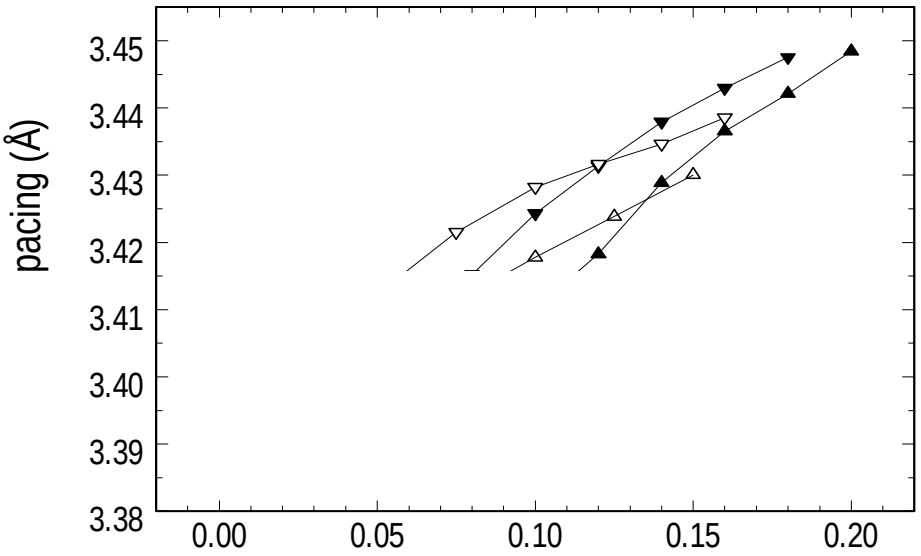

Figure 3-8: Compression curves. The nearest-neighbor spacing of Pb monolayer *vs.* the electrode potential; in chloride-free electrolyte (solid triangles) and in chloride-containing (0.4 Mm) electrolyte (hollow triangles). The data collected while decreasing (increasing) the potential are represented by triangles pointing down (up).

were chosen because the complete set of data had to be measured before the sample surface became noticeably roughened, usually after 15-20 hours. In addition to the hysteresis in the position of the diffraction peaks, the intensities and widths also show a weak dependence on the potential scan direction. The diffraction peaks measured during the anodic scan (increasing potential) were slightly but consistently stronger and narrower than the peaks measured during the cathodic scan (decreasing potential), indicating that the Pb monolayer obtained increasing potential is more ordered than decreasing potential. The observed hysteresis, arising from a large equilibrium time constant for the formation of the ordered overlayer, suggests that there exists an activation energy associated with adding and taking away a Pb adatom. A similar hysteresis was also observed for the diffraction profiles of the electrochemically adsorbed iodine monolayer on Au(111) [18]. The hysteresis observed in the diffraction peaks should be distinguished from the irreversibility seen in the voltammetry, in which the deposition and stripping of the UPD monolayer do not occur at the same potential (see Fig. 3-2). The voltammetric irreversibility only reflects the hysteresis associated with the charge transfer needed for formation and stripping of the Pb UPD monolayer. The time constant for the charge transfer is on the order of several seconds and can be measured by potential step method or estimated from the width of the voltammetric peaks. On the other hand, the potential dependence of the diffraction peaks measures the hysteresis associated with adding (removing) additional adatoms into (out of) an ordered Pb overlayer, and the subsequent relaxation of the layer. The time constant for the structural response to the potential is much larger (on the order of several minutes).

The compression data shown in Fig. 3-8 can be used to calculated the two dimensional isothermal compressibility of the Pb UPD monolayer. The isothermal compressibility, $\kappa_{2D,,}$ for electrochemically deposited layer with a hexagonal structure is given by [10]

$$\kappa_{2D} = \frac{\sqrt{3}a}{n e}\left(\frac{\partial a}{\partial V}\right)_T \qquad (3\text{-}4)$$

where n is the number of electrons required for oxidation or reduction of the adatom (i.e. Pb = $Pb^{n+} + ne^-$, $n = 2$), and V is the electrode potential. The quantity, $(\partial a/\partial V)_T$ is the measured slope of the electrocompression data. Although the large hysteresis presented in our data makes estimation of the slope difficult, the data were reasonably represented when fitted with a line going through the middle of the hysteresis loop. The two dimensional isothermal compressibility of Pb on Cu(111), estimated with the linear fit of data, was 0.95 ± 0.07 Å^2/eV. This value is smaller than the previously measured values for the Pb UPD monolayer on Ag(111) and Au(111), 1.25 ± 0.05 Å^2/eV and 1.69 ± 0.10 Å^2/eV, respectively [10].

In order to study the anion effects on the UPD Pb monolayer, a small known amount of chloride (0.4 mM) was introduced to the system. The packing arrangement of the Pb monolayer on Cu(111) was not affected by the presence of chloride. The Pb monolayer still formed an unrotated hexagonal close-packed structure. However, the presence of chloride in the electrolyte influenced the compression behavior of the Pb monolayer. The data represented by hollow triangles in Fig. 3-8 are the compression curve of the Pb monolayer obtained in an chloride containing electrolyte (0.1 M $HClO_4$ + 5 mM PbO + 0.4 mM NaCl) and otherwise under identical condition. The effects of chloride on the compression behavior of the Pb monolayer are clearly seen. One of the most apparent effects is the increase in the Pb-Pb spacing, especially in the lower UPD potential region (<0.12 V). Another way to appreciate this apparent increase in the Pb-Pb spacing is in terms of a shift in the compression curve. A large portion of both compression curves overlap if the compression curve obtained in the chloride-containing electrolyte is shifted by about 25 mV. This shift of the compression curve is consistent with the voltammetric response

of the system, in which the deposition peak of Pb monolayer is typically shifted to more negative potentials upon addition of specifically adsorbing anions like chloride and acetate, and the amount of shift depends on the concentration and the type of anions [7,8]. In our case, a shift of -25 mV was observed at 0.4 mM chloride concentration as shown in Fig. 3-2. This shift in the voltammetry is not just kinetic effects but an actual change in the deposition potential. For example, the Pb diffraction peak was never observed at 0.18V upon decreasing the potential in the electrolyte with 0.4 mM chloride. Consequently, the compression of the Pb monolayer is expected to be lagged in potential, because the rates of compression in both electrolytes are comparable. In addition, the presence of chloride in the electrolyte decreased the compression hysteresis. This is consistent with the voltammetric response of the system (see Fig. 3-2) and an interpretation that the UPD process becomes more reversible and enhanced in its kinetics with addition of chloride [7,8]. Another effect of chloride is a decrease in the slope of the compression curve. Since the 2D compressibility is obtained from the slope of the compression curve, the decrease in the slope indicates a decrease in the compressibility of the Pb monolayer. The measured compressibility in the chloride-containing electrolyte is 0.79 ± 0.09 Å^2/eV. This is a $17 \pm 11\%$ change. In addition to the effects exhibited in Fig. 3-8, the influence of chloride was also manifested in the profiles of the Pb diffraction peak. After adding chloride, the diffraction peak became noticeably weaker and wider, indicating that the Pb monolayer was less well-ordered with chloride. The change in the compressibility and the broadening of the diffraction suggests that the effect of chloride on the structure of Pb monolayer and its compression property is not negligible. The compression curve measured at 4 mM chloride concentration (data not shown) exhibited much greater chloride effects. However, these measurements may have been hampered by white precipitants visible on the surface (probably $PbCl_2$) which significantly changed the voltammetry and severely weakened

the Pb diffraction peaks.

3.3.3 Surface normal structure

The surface normal structure of the underpotentially deposited Pb monolayer was probed using the X-ray reflectivity measurement. Reflectivity is a well-established technique to measure the electron density profile in the surface normal direction [19]. Fig. 3-10 shows the reflectivity measurements at two different potentials, 0.160 V and 0.050 V in the chloride-free electrolyte. The data are represented by the hollow symbols and the solid curves are the best fits to the data. The dashed curve is the calculated reflectivity curve of the ideally terminated bare Cu(111) surface. Each data point was obtained by integrating the ϖ-rocking curves at each L value in order to remove the background due mainly to scattering from the solution and membrane. The divergent behavior at $L = 3$ and 6 is due to $(0,0,3)_{hex}$ or $(1,1,1)_{cubic}$ and $(0,0,6)_{hex}$ or $(2,2,2)_{cubic}$ bulk Bragg peaks. Both data sets deviate significantly from the calculated curve for the ideally terminated surface. The dramatic modulations around the Bragg peaks are due to the constructive and destructive interference between the amplitudes scattered by the substrate and the much heavier Pb monolayer on the surface. Although the data measured at both potentials look very similar, a careful inspection reveals some fine differences. The data taken at 0.05 V are slightly larger on the shoulders to the left of the Bragg peaks and smaller at the minimum. Also, the minimum at 0.05 V is slightly narrower and is located slightly closer to the Bragg peak. These difference are consistent with the increase in Pb coverage. The detail of the surface normal structure is obtained by fitting the data with a layered model. Since the density of the water is much smaller than the density of Pb, the data were easily fitted with a simple model including only a monolayer of Pb and bulk Cu(111) substrate with a relaxed top layer. The reflected intensity is given by the square of the structure factor which is written as

$$|F(q_z)|^2 = e^{q_{abs}/q_z}\left| f(q_z)e^{-q_z^2\sigma_B^2/2}\sum_{n=0}^{n=\infty} e^{-ind_B q_z} + f_{Cu}(q_z)e^{-q_{Cu}^2\sigma_{Cu}^2/2}e^{id_{Cu}q_Z} + \theta_{Pb}f_{Pb}(q_z)e^{-q_z^2\sigma_{Pb}^2/2}e^{id_{Pb}q_z}\right|^2 \qquad (3\text{-}6)$$

The first term is the contribution from the bulk Cu(111) where the summation over n represents the semi-infinite crystal. The second and the third terms represent the contributions from the topmost Cu layer and the deposited Pb monolayer, respectively. The parameters pertaining to the bulk, the topmost Cu layer, and the Pb layer are denoted with labels, B, Cu and Pb. The quantity, $f(q_z)$, is the atomic scattering form factor, which approaches to the number of electrons in the atom as q_z becomes small. The Debye-Waller factor, $e^{-q_z^2\sigma^2/2}$ accounts for thermal vibration of the atoms as a root-mean-square (rms) atomic displacement, σ. The parameter, d, is the position of the layer in question. The parameter, θ_{Pb}, is the coverage of the Pb layer, and the coverage of the topmost Cu layer is assumed to be unity. The prefactor, e^{q_{abs}/q_z}, is the correction factor for

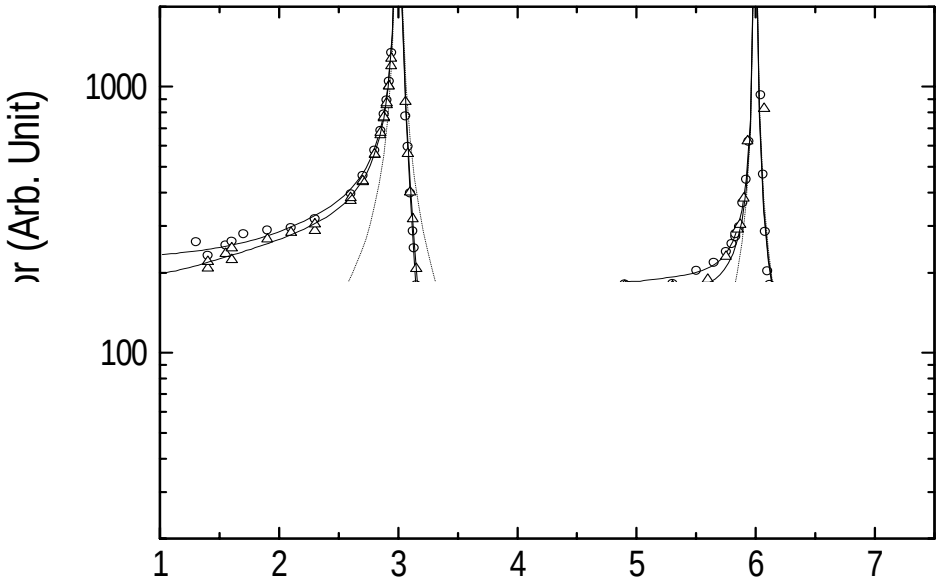

Figure 3-10: Reflectivity Data; at 0.160 V (triangles) and at 0.050 V (circles). The lines are the best fits to the data using Eq. (3-6). The calculation for a perfectly terminated Cu(111) surface without Pb is represented by the dotted line.

the absorption by the thin electrolyte film over the surface, and $q_{abs} = 0.10$ Å^{-1} was obtained from the fits. In the fitting analysis, the bulk spacing d_B and Debye-Waller parameter, σ_B, were fixed at their bulk values, 2.087 Å and 0.085 Å [20] , respectively, but all other parameters were allowed to vary. The proposed model produced excellent fits for both data sets ($\chi^2 = 1.17$ for data at 0.160 V and $\chi^2 = 0.67$ for 0.050 V). The fit parameter results are listed in Tab.3-4

At 0.160 V, the coverage of the Pb monolayer, 0.52 ± 0.02, is close to the coverage of 0.55 based on the Pb lateral spacing. The spacing of the topmost Cu layer, 2.096 ± 0.009 Å, is slightly (0.5%) expanded from the bulk spacing. The Debye-Waller parameter for the topmost Cu atoms, 0.09 ± 0.03 Å and the deposited Pb atoms, 0.21 ± 0.01 Å, are in a good agreement with the bulk values, 0.085 Å and 0.206 Å, respectively. The spacing between the Pb monolayer and the topmost Cu layer (d_{Pb} - d_{Cu}) turned out to be 2.519 ± 0.011 Å. The average bond length of Pb-Cu can be calculated under the assumption that there is no preferred site for Pb atoms and all possible relative positions of Pb atom with respect to the nearest Cu atom are equally probable, which is a valid assumption for an ideally incommensurate structure. The calculated average bond length is 2.68 ± 0.05 Å, while the bond length for topsite, bridge site, and hollow site would be 2.52 Å, 2.82 Å, and 2.92 Å, respectively. The average bond length is significantly smaller than 3.03 Å, the average of the radii for bulk Pb (3.50 Å) and Cu (2.56 Å), suggesting a considerable bonding

E (V)	atom	spacing (Å)	σ (Å)	coverage
0.160	Cu	2.096 ± 0.009	0.09 ± 0.03	1 (fixed)
	Pb	2.519 ± 0.011	0.21 ± 0.01	0.52 ± 0.02
0.050	Cu	2.111 ± 0.009	0.09 ± 0.02	1 (fixed)
	Pb	2.497 ± 0.011	0.21 ± 0.01	0.58 ± 0.02

Table 3-4: Fit results of the reflectivity data.

between Pb and Cu. The only significant change in the surface normal structure with the potential was the Pb coverage. At 0.05 V, the Pb coverage obtained from the fits is 0.58, which is in a good agreement with 0.57, the estimated coverage based on the in-plane Pb spacing. The change in all other parameters are well within the errors.

Other models were also used to fit the data to investigate the possibility of different structures. An additional layer of Pb was added with a variable coverage, but that value refined to zero; giving a convincing evidence that the underpotential deposition of Pb on Cu(111) is limited only to a single monolayer. The voltammetric peaks become significantly wider after extensive potential cycling and/or long polarizations with a full coverage of the Pb monolayer, which raises the question of the possibility of surface alloying. To test this possibility, the data were fitted using various models allowing the presence of Pb below the Cu surface. These models all failed to fit the data, giving large χ^2 and moreover produced unphysical parameter values. Therefore, the formation of surface alloying during the time required for the measurements (about 10 hours) is undetectable.

3.4 Discussion

Our in-situ surface X-ray diffraction study demonstrated that UPD Pb on Cu(111) forms an ordered incommensurate close-packed hexagonal monolayer structure, exactly aligned with the substrate. Although the packing arrangement and alignment of the Pb monolayer with the substrate did not show any potential dependence, the spacing continuously changed from 3.448 to 3.392 Å. No locking-in of the Pb spacing was observed at a possible commensurate (4×4) structure which corresponds the Pb spacing of 3.408 Å, in the middle of this range. Thus, the Pb monolayer behaved much like a two dimensional floating layer unaffected by the periodic potential of the substrate. In the past, there have been four reports on the structure of Pb monolayer on

Cu(111): three on the evaporated Pb film in vacuum[12,13,14] and one on the Pb UPD monolayer emersed into vacuum [8]. The first two of these studies claimed a commensurate $p(4\times4)$ structure, whereas the later two claimed an incommensurate hexagonal structure. It is possible that the older measurements lacked the accuracy to distinguish between the $p(4\times4)$ and incommensurate structures. In addition, Ref. 12 and Ref. 13 reported an abrupt change in the lattice parameter with the coverage, while Ref. 14 observed a more gradual change. These findings are qualitatively consistent with our results. The sudden change of the lattice parameter of the Pb layer may be due to non-equilibrium behavior at the interface during the vapor deposition. One interesting finding of Ref. 8 is that the spacing of the Pb monolayer was the same as the bulk value, regardless of the emersion potential. This suggests that the compressed Pb spacing may have become relaxed to its natural spacing after the loss of potential control. Despite some quantitative differences, the structure of evaporated Pb film on Cu(111) and the underpotentially deposited Pb monolayer on Cu(111) are apparently the same.

While the electrochemically deposited and evaporated Pb monolayers on Cu(111) share a common structure, the Pb monolayer exhibits different structures on different substrates, in particular Au(111) and Ag(111). Although the Pb monolayer forms an incommensurate hexagonal structure on all three substrates, it has different rotation angles with respect to the substrate orientation. On a Ag(111) substrate prepared by evaporating Ag film on mica, the Pb monolayer was rotated with a fixed rotation angle of 4.5° [10]. On the evaporated Au(111) film on mica, the rotation angle showed the potential dependence; 2.5° for the potential less than 0.13 V and 0° for the potential larger than 0.16 V [10]. In contrast, for the Pb monolayer on Au(111) single crystal, the rotation angle changed continuously from about 2° at 0.21 V to 3.7° at 0.05V with a large hysteresis [21]. The discrepancy between the Au(111) film and the single crystal

results may be due to very large mosaic present in the evaporated Au(111) film. According the theory of McTague and Novaco [9], an epitaxial overlayer should rotate with respect to the substrate to reduce the strain energy due the mismatch of the lattice parameters, and the rotation should increase with the increasing mismatch. The theory predicts a rotation angle of 5~6° on both Ag(111) and Au(111) (about 21% mismatch) and 8~9° on Cu(111) (about 37% mismatch). Moreover, the rotation angle should decrease as the potential decreases because the decreasing potential compresses the spacing of the Pb layer, reducing the misfit. Although the theory seems to be in a qualitative agreement regarding the rotation of Pb monolayer on Au(111) and Ag(111), it fails completely in the case of the Pb monolayer on Cu(111), which we find is not rotated at all. In addition, the direction of the potential dependence of the rotation of Pb monolayer on Au(111) is inconsistent with the theory. Considering the all the experimental facts, the theory of McTague and Novaco [9] does not work well for the epitaxial metal layer. The reason for the failure may be that the theory is based on phonon interactions between the overlayer and substrate, whereas the electronic effects are more important for a metal overlayer on metal substrate. The absence of rotation in Pb/Cu(111) suggests that the spatial corrugation of the underlying Cu(111) substrate is too fine to impose a significant influence on the structure of the much larger adatoms. Despite its quantitative failure in these systems, the theory can still offer some insights. If the rotation is needed to lower the interaction energy between the epitaxial layer and the substrate, the fact that the rotation exists means the substrate influence is not negligible. The absence of rotation in Pb/Cu(111) suggests that the spatial corrugation of the underlying Cu(111) substrate is too fine to impose a significant influence on the structure of the much larger adatoms, and the adatom-substrate interaction for Pb/Cu(111) is expected to be smaller than for Pb/Ag(111) and Pb/Au(111).

Although it is plausible to think that the lack of rotation in the Pb/Cu(111) system is attributed

to the large size difference between Pb and Cu atoms, a possibility exists that the lack of rotation may be extrinsic, due to defects or impurities on the substrate as observed in some systems of physisorbed noble gases. For example, for Xe/Ag(111), the lack of 30° rotation predicted by the theory of McTague and Novaco [9,22] is attributed to the preferential nucleation of the Xe monolayer along the (111) steps [23]. For Kr/Pt(111), rotation angles of 30°, 0°, or both (in coexistence) were observed depending the levels and types impurities blocking the step sites [24]. If there were effects due to steps or impurities, we would expect inhomogeneous distributions of rotation angles as a function of miscut, polishing conditions, and contaminants (Cl^-). In our experiment, four different substrates were used, with different miscut directions (all less than 0.5°). A total of about 20 separate measurements with different levels of chloride concentrations were performed on these substrates, each time freshly repolished, but we never observed a rotated Pb overlayer. So, we conclude that the lack of rotation was not due to the effects of steps or impurities. However, no matter what the actual reason for the lack of the rotation may be, our findings on the compression properties of the Pb monolayer are unaffected.

The compression behavior of the Pb monolayer on Cu(111) can be satisfactorily modeled by the free electron gas model [25]. The justification for using the free electron description is that the Pb monolayer does show evidences of a floating 2D layer. In the free electron gas model of a metal, the 2D compressibility, κ_{2D}, for a closed-pack hexagonal 2D metal is given by [10](see chapter 4).

$$\kappa_{2D} = \frac{3ma^4}{4\pi\hbar Z^2} \qquad (3\text{-}8)$$

where m is the electron mass, a is the nearest neighbor spacing of the 2D metal, and Z is the number of valence electrons per metal atom. The κ_{2D} computed using $a = 3.386$ Å which is the extrapolated nearest neighbor spacing at $V = 0$ and $Z = 4$ is 0.258 Å^2/eV, whereas the measured κ_{2D} value using Eq. (3-4) is 0.95 ± 0.07 Å^2/eV. This apparent discrepancy is resolved by considering the fact Eq. (3-8) is derived using the valence electron density in the 2D metal while Eq. (3-4) is derived using the atomic density. In order to compare the two values on the same footing, the measured κ_{2D} value must be divided by $Z = 4$. After this correction, the experimental κ_{2D} value agrees excellently with the theoretical value based on the free electron gas model as shown in Fig. 3-12. In Fig. 3-12, the data collected during each potential scan direction are fitted separately with a line of fixed slope given by theoretical compressibility in the free electron gas model. The agreement between the theoretical compressibility value and the measured

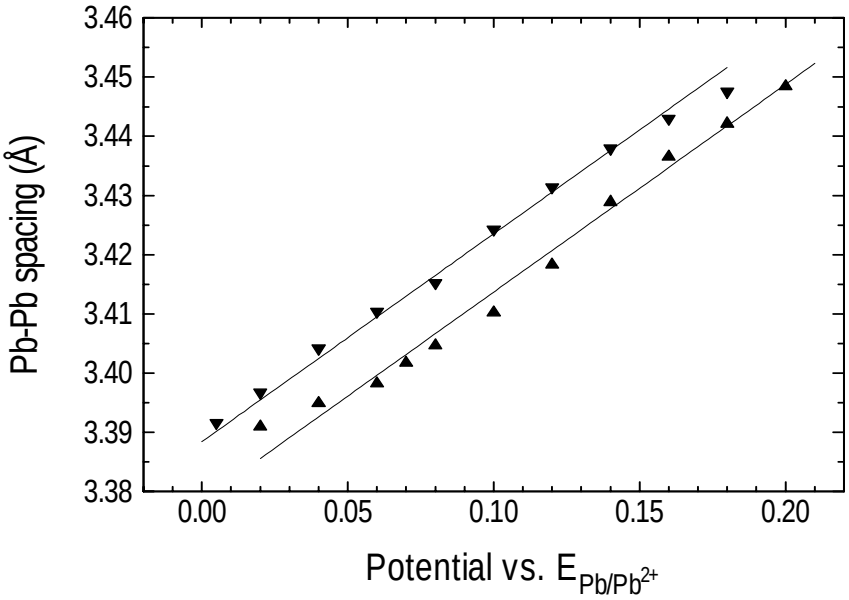

Figure 3-12: Comparison between the data and the theoretical compressibility in the free electron gas model. The data obtained in each potential scan direction are fitted separately with a line of fixed slope given by the theoretical compressibility value; downward triangles (decreasing potential);upward triangles (increasing potential).

compressibility values for Pb/Au(111), 1.69 ± 0.1 $Å^2$/eV, and for Pb/Ag(111), 1.25 ± 0.05 $Å^2$/eV, is not very good. The different levels of agreement for these three similar systems are attributed to the difference in the degrees of the interaction between the Pb overlayer and the substrate, which must be added to the free electron description [26].

It is interesting to observe that the surface normal structure of the Pb monolayer exhibited little potential dependence while the in-plane spacing was strongly affected by the electrode potential; as the potential changed from 0.160 V to 0.050 V, the Pb-Cu bond length remained virtually constant. It implies that the electronic density of the Pb monolayer along the surface normal direction is unaffected by the compression in the plane. This is in complete contrast with the usual three dimensional situation in which a structure under lateral pressure is vertically expanded [27]. At both potentials, the average Pb-Cu bond length was smaller than the sum of the two metallic radii, and the topmost Cu layer spacing was slightly expanded. This surface normal structure is consistent with that for most metals. The top surface layer spacing of a metal is usually contracted from its bulk spacing in order to lower the energy of the surface layer by increasing effective coordination of the surface atoms, and the second layer is expanded to relieve the strain caused by the contraction of the first layer and to restore the average atomic volume at the surface [28]. In the case of the Pb UPD layer, the Pb monolayer is fully discharged and becomes part of a com-bined metal-substrate system. Since the Pb layer is the top layer for this combined system, the Pb-Cu spacing is contracted from the "bulk" spacing, meaning the sum of the two metallic radii. The topmost Cu layer, now being the second layer of the combined system, is consequently ex-panded. A similar finding is reported for the underpotentially deposited Tl layer on Au(111) [11].

Our findings on the surface normal structure are in contrast to results of the standing wave

measurements by Zegenhagen et. al., in which the Pb-Cu spacing depended on the electrode potential [5]. According to their measurements, the Pb-Cu spacing was 2.32 ± 0.07 Å at the potential near the UPD deposition peak and 2.54 ± 0.03 Å near the bulk deposition potential for Pb. Their Pb-Cu spacing near the bulk deposition potential for Pb is in agreement with our results, but the value near the UPD deposition peak is significantly different from ours. In order to explain the unusually small Pb-Cu spacing, they proposed a model in which an oxygen is embedded in the interstitial sites between the 1st and 2nd Cu layers, and the Pb atom is located at the 3-fold hollow sites. The interstitial oxygen would cause a outward displacement of three Cu atoms in the 1st layer, allowing the Pb atom to move downward further. This model is based on incorrect assumptions about the registry of Pb atoms and the Pb coverage. Since the outward displacement is not possible for all the 3-fold hollow sites for Cu, in order to accommodate such geometry, the Pb coverage must be much less than 0.52-58, the value confirmed by our in-plane diffraction and reflectivity measurements as well as the previous electrochemical studies[6,7,8]. The voltammetry of Zegenhagen et. al. indicates that there is a significant level of oxidation and reduction of the working electrode, which was never observed by others. Therefore, it is possible that the structure for Pb/Cu(111) may be completely when the copper substrate is significantly oxidized. One way to confirm the results of Zegenhagen et. al. [5] would be to repeat our experiment in an electrolyte with a higher pH.

Since the effects of anions on the Pb UPD process on Cu(111) are of significant interest, the effects of chloride on the UPD Pb/Cu(111) structure deserve more discussion. Anions are known to incorporate into the UPD structures if the UPD layers form open structures [29]. However, it is generally accepted that anions are not involved in a UPD structure if the UPD layer forms an closed structure like the close-packed hexagonal structure [10,15]. We also come to the

same conclusion for UPD Pb/Cu(111) in that the packing arrangement of the Pb on Cu(111) is also hexagonal in the chloride-containing electrolyte. However, it is not certain if the specifically adsorbed anions affect the detail of the structure and/or properties. The good agreement between the Pb coverage based on the reflectivity measurements and the estimated values from the in-plane lattice spacing indicates that the chloride is not present inside the Pb monolayer but rather specifically adsorbed on top of the Pb monolayer. This conclusion is supported by the coulometry measurements by Brisard et. al. [8]. Thus, we believe that the change in the compression behavior of the Pb monolayer shown in Fig. 3-8 is due to the influence of the specifically adsorbed chloride onto the Pb UPD layer. It is probable that the specifically adsorbed chloride affects the valence electron density of the Pb monolayer, modifying the compression behavior of the Pb layer. Though it was not as dramatic, a similar phenomenon was observed by Toney et. al. [10]. At the same electrode potential, they found that the Pb-Pb spacing was slightly larger in the acetate than in the perchlorate. Also, the slope of the compression curve was slightly smaller in the acetate. These findings are in qualitative agreement with our results. A possible reason for the smaller anion effects seen by Toney et. al. may be that acetate is not as strongly adsorbing an anion as chloride.

3.5 Conclusion

In our experiment, the structure of the Pb UPD monolayer on Cu(111) was studied by surface X-ray diffraction. The Pb UPD monolayer exhibited an unrotated incommensurate hexagonal structure. No other structure was observed throughout the entire UPD potential range. The structure found for the Pb UPD monolayer is consistent with the vapor-deposited Pb monolayer on Cu(111). However, it is different from the structure of Pb UPD monolayer on Au(111) and Ag(111) in which the overlayer was rotated with respect to the substrate.

The in-plane nearest-neighbor spacing of Pb monolayer was found compressed by 1.4-3.2% compared with the Pb bulk spacing. The compression of the Pb monolayer exhibited hysteresis, which is attributed to the slow kinetics and the irreversibility associated with the formation of the ordered Pb layer on Cu(111). Despite the hysteresis, the Pb monolayer on Cu(111) behaved much like an ideal 2D floating layer, exhibiting excellent agreement with the free electron gas model [26].

The surface normal structure, probed with the reflectivity measurements, was modeled satisfactorily with a single Pb layer on the relaxed Cu(111) substrate. The coverage obtained from the fits agree well with the estimates based on the in-plane lattice spacing. Unlike the in-plane structure, the surface normal structure showed little potential dependence. Based on the fitting analysis using various models, the possibilities for the deposition of more than one Pb monolayer during the UPD process on Cu(111), or the formation of surface alloy, is negligible.

The presence of chloride in the electrolyte significantly influenced the Pb UPD process. Addition of chloride in the electrolyte enhanced the kinetics and reduced the irreversibility of the UPD process. These effects were manifested through reduction of the hysteresis in the compression behavior of the Pb monolayer. Moreover, a decrease in the compressibility of the Pb monolayer was observed. The influence on the compressibility suggests that the valence electronic density of the Pb monolayer may be affected by the specifically adsorbed chloride.

3.6 References

[1] D. M. Kolb, *Advances in Electrochemistry and Electrochemical Engineering, Vol. 11*, Eds. H. Gerischer, and C. W. Tobias (Wiley-interscience, New York, 1978).

[2] R. Adzic, *Advances in Electrochemistry and Electrochemical Engineering, Vol. 13*, Eds. H. Gerischer, and C. W. Tobias (Wiley-Interscience, New York, 1978).

[3] D. M. Kolb, M. Przasnyski, and H. Gerischer, J. Electroanal. Chem. **54**, 25 (1974).

[4] M. Ge and A. A. Gewirth, Surf. Sci., **324**, 140 (1995).

[5] J. Zegenhagen, G. Materlik, J. P. Dirks, and M. Schmäh, *Synchrotron Techniques in Interfacial Electrochemistry*, Eds. C. A. Melendres and A. Tadjeddine (Kluwer Academic Publishers, Boston, 1994).

[6] H. Siegenthaler and K. Jüttner, Electroanal. Chem., **163**, 327 (1984).

[7] J. R. Vilche and K. Jüttner, Electrochim. Acta. **32**, 1567 (1987).

[8] G. M. Brisard, E. Senati, H. A. Gasteiger, N. M. Markovíc, and P. N. Ross, Jr.,

[9] J. P. McTague and A. D. Novaco, Phys. Rev B, **19**, 5299 (1979).

[10] M. F. Toney, J. G. Gorden, M. G. Samant, G. L. Borges, and O. R. Melroy,

[11] J. Wang, R. Adzic, and B. Ocko, J. Phys. Chem., **98**, 7182 (1994).

[12] J. Henrion and G. E. Rhead, Surf. Sci., **29**, 20 (1972).

[13] K. J. Rawlings, M. J. Gibson, and P. J. Dobson, J. Phys. D. **11**, 2059 (1978).

[14] G. Meyer, M. Michailov, and M. Henzler, Surf. Sci., **189/190**, 1091 (1987).

[15] M. F. Toney, J. G. Gordon, M. G. Samant, G. L. Borges, D. Wiesler, D. Yee, and L. B. Sorensen, Langmuir, **7**, 796 (1991).

[16] C.-H. Chen, K. D. Kepler, A. A. Gewirth, B. M. Ocko, and J. Wang,

[17] D. D. Sneddon, Ph.D. thesis, University of Illinois, 1995.

[18] B. M. Ocko, G. M. Watson, and Jia Wang, J. Phys. Chem., **94**, 897 (1994).

[19] J. Als-Nielsen, *Handbook on Synchrotron Radiation, Vol III*, Eds. G.S. Brown, and D. E. Moncton (North-Holland, Amsterdam, 1991).

[20] *International Tables for X-ray Crystallography, Vol III*, (The Kynoch Press, Birmingham, England, 1962).

[21] B. M. Ocko, private communication

[22] L. W. Bruch and J. M. Phillips, Surf. Sci., **91**, 1 (1980).

[23] P. I. Cohen, J. Unguris, and M. B. Webb, Surf. Sci., **58**, 429 (1796).

[24] K. Kern, P. Zeppenfeld, R. David, R. L. Palmer, and G. Cosma, Phys. Rev. Lett., **57**, 3187 (1986).

[25] N. Ashcroft and N. D. Mermin, *Solid State Physics* (Saunders, Philadelphia, 1976).

[26] Y. S. Chu and I. K. Robinson (to be published).

[27] J. P. Hirth, and J. Lothe, *Theory Of Dislocations*, (A Wiley-Interscience Publication, New York, 1982).

[28] A. Zangwill, *Physics At Surfaces* (Cambridge University Press, Cambridge, 1988).

[29] M. F. Toney, J. N. Howard, J. Richer, G. L. Borges, J. G. Gordon, O. R. Melroy, D. Yee, and L. B. Sorensen, Phys. Rev. Lett. **75**, 4472 (1995).

4. Substrate Dependence of the Compressibility of 2D Metals.

As shown in the last chapter, the Pb monolayer on Cu(111) compresses much like an ideal 2D electron gas. However, the Pb monolayers on other similar substrates, Ag(111) and Au(111), exhibit somewhat different compression behaviors. In this chapter, the compression behaviors of the Pb monolayers on these three substrates are compared, and the possible reasons for such "substrate effects" are discussed.

4.1 Introduction

In the last decade, powerful modern surface science tools such as scanning microscopy [1,2,3] and surface X-ray diffraction [4,5,6,7,8] have been used to probe the metal/electrolyte interfaces on an atomic scale, obtaining breakthroughs in understanding of simple electrochemical interfaces and their fundamental interactions. Although study of these interfaces is often motivated by chemical interests, its significance is by no means limited to the field of electrochemistry but can offer us excellent model systems in which to study 2D physics. In particular, a two-dimensional metal layer electrochemically deposited onto a metal substrate is of significant importance because it closely resembles an ideal two dimensional metal. In practice, such a metal layer can be obtained through an unique electrochemical process called underpotential deposition (UPD) in which deposition of foreign metals, usually a single monolayer thick, occurs at potentials positive of the bulk deposition potential [9]. This is analogous to the surface wetting of an physisorbed gas before bulk condensation [10]. In an electrochemical system, the potential at the interfaces externally controlled and plays a similar role to the gas pressure for systems of physisorbed gas. During the potential region of its stability (between the UPD and bulk deposition potentials), the monolayer is in thermodynamic equilibrium with the reservoir of the metal ions in

solution, and its structure and the properties can be measured in the absence of strong non-equilibrium effects. One interesting aspect of the electrochemically deposited 2D metals is that their structures respond sensitively to the electrode potential if they lack strong adatom-substrate interactions to pin the adatoms at fixed sites. The measured lattice parameters of these 2D metals can be reproducibly controlled by the electrode potential with an accuracy better than 0.01Å [4,5,6,7,8]. On the other hand, evaporated metal layers in UHV are usually specified by their coverage, since equilibrium with a vapor is hard to achieve. Although the fundamental reason for structural dependence on the potential is clear [8], there has been no satisfactory quantitative description of the compression behavior of these 2D metals. Moreover, there seems be a systematic substrate dependence on the 2D compressibility values, all of which were consistently larger on Au(111) than on Ag(111) [6,7,8]. In this chapter, we present the compression data of the 2D Pb monolayer on Cu(111) in order to investigate further these "substrate effects". Then we explain the substrate trend using a phenomenological parameterization of a simple free electron gas description of the metallic cohesion in the 2D layer.

4.2 Discussion

The Pb-Pb spacings of the Pb monolayers on three substrates, Au(111), Ag(111), and Cu(111) are plotted together on Fig. 4-1. The data on Pb/Au(111) and Pb/Ag(111) are taken from Ref. [8], which were obtained in a very similar way.. Each data point in Fig.4-1 corresponds to the position of the Pb diffraction peak along the radial direction. There are clear differences in the compression behavior of the Pb monolayers; the slope of the compression is largest on Au(111) and the least on Cu(111). The data for Pb/Cu(111) exhibit some hysteresis with the direction of the potential scan. The hysteresis is due to slow kinetics, and its degree was found to decrease

with the time scale of the measurements [11] (see section 3.3.2). The differences among the three compression curves are too large to be explained by experimental errors. Since virtually the same electrolytes were used for the all three experiments, and perchlorate (ClO_4^-) is known to be one of the most weakly interacting anions [12], we can rule out the possibility of electrolyte effects. Therefore, the differences in the observed Pb compression curves must be due to the influence of the substrates. However, since the Pb monolayer behaves like a floating layer without any

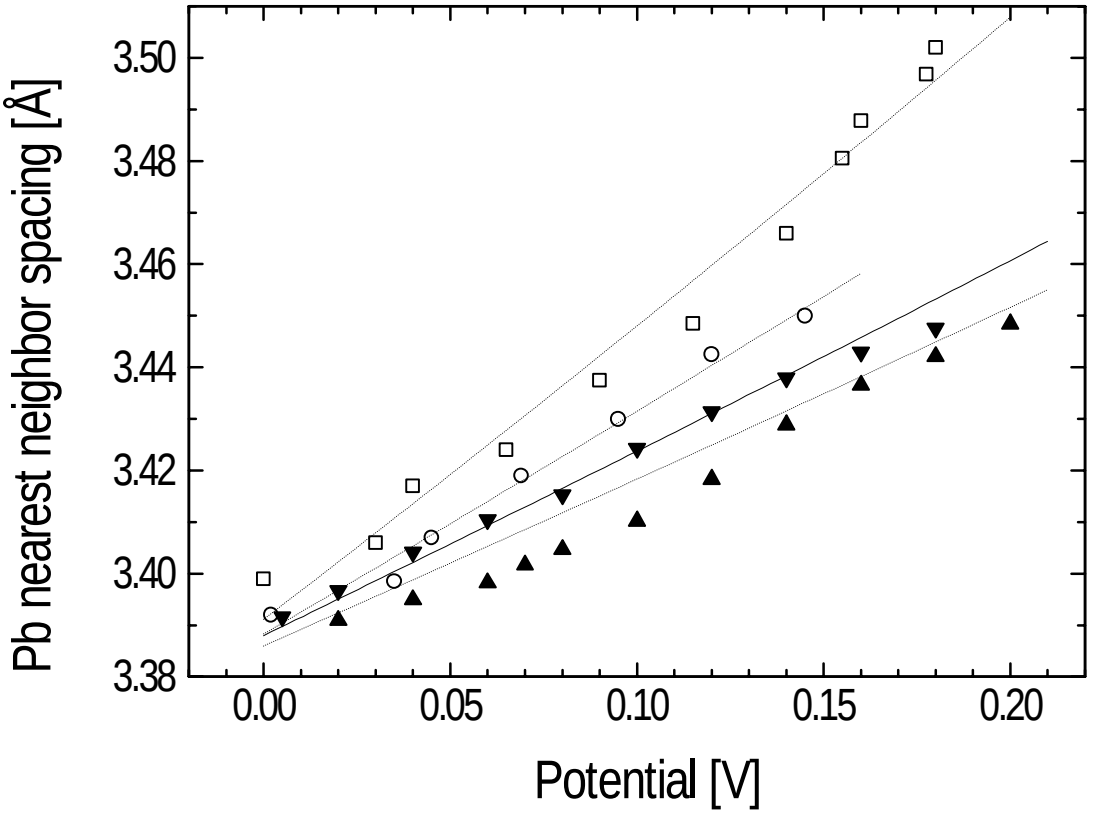

Figure 4-1: Compression curves for Pb monolayer on three substrates: Au(111) (squares), Ag(111) (circles) and Cu(111) (triangles). The data for Pb/Au(111) and Pb/Ag(111) are obtained from Ref. [8]. For Pb/Cu(111), the hysteresis in the data is indicated with the data collected while decreasing the potential (downward triangles) and increasing the potential (upward triangles). The dashed lines are the best fits to the data using Eq. (**Error! Reference source not found.**) with Z_{eff} and a_{2D} as fitting parameters. The solid line represents the calculation for an ideal Pb electron gas with
$Z_0 = 4$ and $a_{2D} = 3.388$ Å.

tendency to lock-in, the substrate influence is expected to be weak.

In order to explain the substrate dependent compression behavior of Pb monolayers, we start with the simplest model of the 2D metal: the free electron gas model [13]. In this model, the metallic cohesion within the 2D layer is attributed to the valence electrons, assumed to be free. Counting the number of electrons of states, k_i with energy, $\hbar^2 k_i^2/2m$, up to the Fermi wavevector, k_F, gives the electronic density,

$$\rho_e = \frac{k_F^2}{2\pi}. \tag{4-1}$$

The ground state energy of electrons, E, obtained by integration up to the Fermi level, is related to the electronic density by

$$\frac{E}{N} = \frac{1}{2}\frac{\hbar^2 k_F^2}{2m} = \frac{\pi\hbar^2}{2m}\rho_e^2 \tag{4-2}$$

where N is the total number of electrons, and m is the electron mass. The average energy of electrons depends only on their density. By analogy with bulk matter, the isothermal 2D compressibility, κ_{2D}, is given by

$$\kappa_{2D} = \frac{1}{A}\left(\frac{\partial^2 A}{\partial E^2}\right)_T = \frac{m}{\pi\hbar^2}\rho_e^2 = \frac{3ma^4}{4\pi\hbar^2 Z^2} \tag{4-3}$$

where A is the area of the 2D layer. The last identity is obtained by assuming the 2D metal of Z valence electrons per atom forms an ordered hexagonal structure with nearest neighbor spacing, a. The unit cell area, $A_{Cell} = \sqrt{3}a^2/2$, and the electronic density, $\rho_e = Z/A_{Cell}$ were used. Thus, κ_{2D}, related to the free electron density ρ_e, depends ultimately on the lattice spacing, a, of the 2D

layer. To describe the electrochemical interface, the potential dependence must be built into the model, because the Fermi level at the interface changes with the applied potential. We assume that the Fermi level scales with the electrode potential, V, relative to an arbitrary choice of zero, as

$$E_F(V) = E_F(0) - neV\,, \tag{4-4}$$

where n is the number of electrons needed to reduce one adsorbate ion. The factor n is needed because it is the number of electrons that enter the system when an extra atom is added to the layer. The number of electrons transferred per reaction, n, must not be confused with Z, the number of valence electrons per atom. The potential dependence of the Fermi level is analogous to the definition of the electrochemical potential for an electron in an electrode (*i.e.* $\bar{\mu} = \mu - neV$) [14]. This relation can be rewritten as

$$a(V) = \left(\frac{1}{a_{2D}^2} - \frac{2mn}{\hbar^2 ZeV} \right)^{-\frac{1}{2}} \tag{4-5}$$

where a_{2D} is the nearest neighbor spacing for the 2D hexagonal lattice at the chosen zero of potential, which is the bulk deposition potential of Pb in our analysis. Eq. (4-5) describes the way that the nearest neighbor spacing of a hexagonal 2D layer changes with the electrode potential in

Substrate	Z_{eff}	a_{2D} (Å)	κ_{2D} (Å^2/eV)
Au(111)	2.56 ± 0.12	3.391 ± 0.003	1.69 ± 0.1
Ag(111)	3.33 ± 0.18	3.388 ± 0.002	1.25 ± 0.05
Cu(111)	4.41 ± 0.29	3.386 ± 0.002	0.96 ± 0.09

Table 4-1: Fit results of the compression curves of the Pb monolayer on three substrates along with the measured κ_{2D} values. Z_{eff} is the effective number of valence electrons in the Pb monolayer, and a_{2D} is the Pb nearest-neighbor spacing at the Pb bulk deposition potential.

the framework of the free electron gas model. Eq. (4-5) can be converted into an alternate expression for the 2D compressibility,

$$\kappa_{2D} = \frac{\sqrt{3}\,a}{Zne}\left(\frac{\partial a}{\partial V}\right)_T \qquad (4\text{-}6)$$

where $(\partial a/\partial V)_T$ is the slope the compression curve. Eq. (4-6) differs by a factor, Z, in the denominator from the expression used by Toney *et. al.* [8] (see Eq. (3-4) in section 3.4). The discrepancy is attributed to fact that, in the free electron gas model, κ_{2D} , is computed using electronic density. In order to compare the experimentally measured κ_{2D} values with the calculation based on the free electron gas model, it is important that the factor Z be taken into account.

Using Eq. (4-6), each compression curve of the Pb monolayer can be fitted with just two fitting parameters, a_{2D}, the nearest neighbor 2D Pb spacing at $V = 0$ and Z_{eff}, the "effective" value $V^{-1/2}$

element	oxidation state	Allred [19]	Pauling [18]
Au	I	2.54	2.3
Ag	I	1.93	1.8
Cu	I	1.90	1.8
Cu	II	2.00	2.0
Pb	II	1.87	1.6
Pb	IV	2.33	1.8
Tl	I	1.62	1.5
Tl	III	2.04	1.9
Bi	III	2.02	1.8

Table 4-2: Estimated electronegativity values from two sources. The discrepancies are due to the difference in estimation method. The electronegativity of an element depends on the oxidation state with a higher electronegativity value associated with the higher oxidation state.

dependence, the fitted curves look quite straight over the narrow range of the data, and provide satisfactory fits. The fitting results are listed in Tab.1, along with the measured κ_{2D} values. Our fitting analysis reveals two important aspects about the compression of Pb monolayers. First, their spacings on all three substrates converge to a single value at the Pb bulk deposition potential (within errors) despite the different degrees of epitaxial strain present at the interfaces. Clearly, the value for a_{2D} is common to all three systems, and it can be identified as a fundamental property of 2D Pb layers. Moreover, a_{2D} is the lattice spacing of a Pb layer in thermodynamic equilibrium

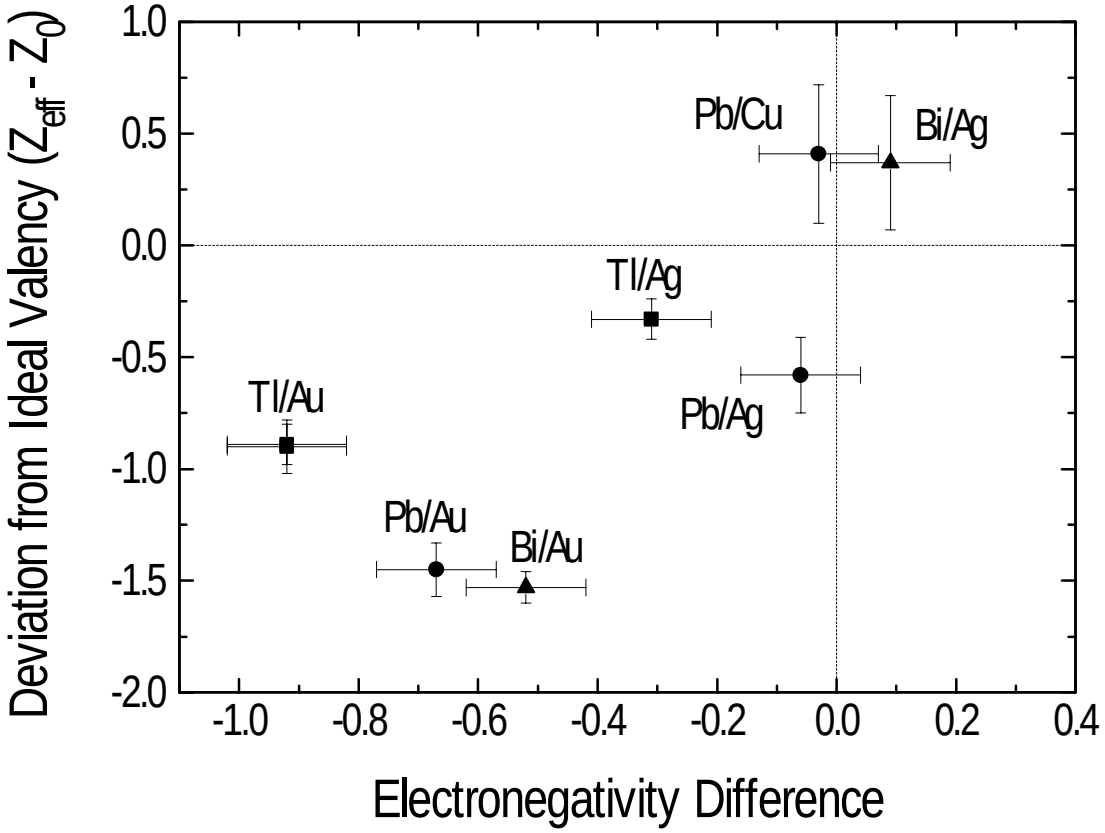

Figure 4-2: Correlation between the deviation from ideal valency (Z_{eff} - Z_0) of 2D metals and the electronegativity differences between the adsorbate and the substrate. The ideal valencies, Z_0, used for Tl, Pb and Bi are 3, 4 and 5, respectively. The electronegativity values of Ref. [19] were used for the plot, but values of Ref. [18] also yield a similar result. An error bar of 0.1 is taken to indicate the uncertainties in the electronegativity values.

with bulk Pb. The second important result is that the substrate dependence of the compression behavior of Pb monolayers can be explained in terms of Z_{eff} alone. In the case for Pb/Cu(111), the large error of is Z_{eff} due to the hysteresis present in the data. The data taken during the negative potential scan exhibit an excellent agreement with the ideal Pb gas (see Fig. 4-1) as well as give a slightly smaller Z_{eff} value.

We have shown that the free electron gas model explains the compressibility of Pb monolayer on all three substrates, provided one adjustable parameter, Z_{eff}, is included. Z_{eff} is the effective number of Pb valence electrons contributing to the free electron gas that is ultimately responsible for the compressibility. The deviation of Z_{eff} from the ideal valency of Pb, $Z_0 = 4$, could be interpreted as a physical transfer of a fraction of the Pb valence electrons into the substrate. Alternatively, there could be a change in the fraction of electrons considered to be "free" in the Pb monolayer due to "bonding" between the Pb monolayer and the substrate. Analogous behavior is from one element to the other are well correlated with their electronegativity difference [15]. The electronic density associated with atoms of the element with the larger electronegativity value is expected to be increased and *vice versa*. Moreover, a binary alloy with a larger electronegativity difference is expected to form stronger internal bonds. Although the concept of electronegativity is

found in other	Z_{eff}	a_{2D} (Å)	κ_{2D} (Å^2/eV)
Tl/Au(111) [8]	2.11 ± 0.09	3.324 ± 0.003	1.88 ± 0.05
Tl/Au(111) [7]	2.10 ± 0.12	3.320 ± 0.04	1.9 ± 0.13
Tl/Ag(111) [8]	2.67 ± 0.09	3.320 ± 0.001	1.52 ± 0.05
Bi/Au(111) [6]	3.47 ± 0.07	4.440 ± 0.004	1.15 ± 0.05
Bi/Ag(111) [4]	5.37 ± 0.34	4.441 ± 0.005	0.79 ± 0.04

Table 4-3: Fit results of other 2D metal systems. For a given 2D metal, the a_{2D} values are independent of the substrates (within errors), and all the substrate dependence is contained in Z_{eff} values. For a given 2D metal, the Z_{eff} values are smaller on Au(111) than on Ag(111).

not theoretically rigorous [16], it has been used extensively for discussing and comparing the properties of solids because it is completely general with regard to bond type, details of crystal structure, and coordination [17]. The electronegativity values for Pb and the substrate metals in their usual oxidation states are listed in Tab. 2, and a clear correlation between the values of Z_{eff} of Pb monolayers and the electronegativity differences between Pb and the substrates is shown in Fig. 4-2.

The model presented here also work for other electrochemically deposited 2D metals. The compression curves for Tl and Bi monolayers on Au(111) and Ag(111) are shown in Fig. 4-3 and Fig. 4-4 together with the fits. The compression data are obtained from Ref. 4, 6, 7, and 8. The

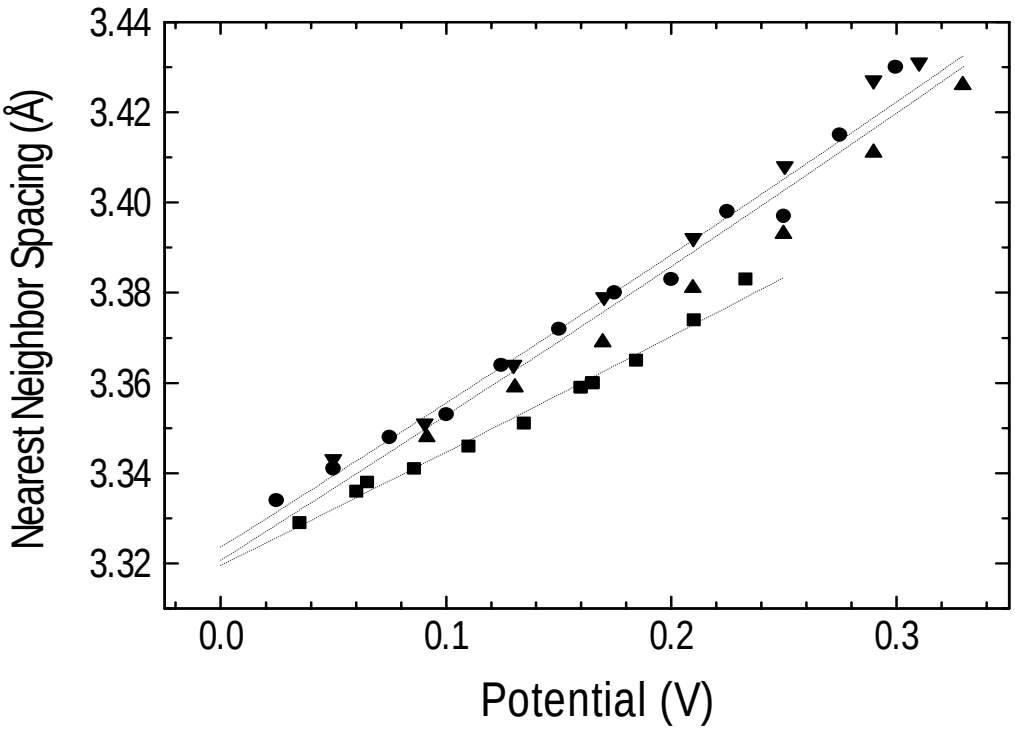

Figure 4-3: Compression curves for UPD Tl monolayers: Tl/Au(111) (circles) [8], Tl/Au(111) (triangles) [7], and Tl/Ag(111) (triangles) [8]. The data from Ref. [7] were obtained in alkaline electrolyte while the others were measured in perchloric acid. The hysteresis for the data from Ref. [7] are indicated with triangles pointing down (during the negative potential scan) and pointing up (during the positive potential scan). The fits to the data are indicated with dotted lines

numerical values of the fit results are listed in Tab. 4-3. The fit results for Tl and Bi are very similar to those of Pb. All the substrate dependence is contained in Z_{eff} alone, and Z_{eff} values are much lower on Au(111) than on Ag(111). The correlation between Z_{eff} values and the electronegativity differences is shown in Fig. 4-2. The good correlation seen in Fig.4-2 supports our hypothesis that the compression of 2D metals is mainly attributed to the valence electron density as modified by the interactions with the substrate. The Z_{eff} values correlate equally well with the *work function* differences between the adsorbates and the substrates. This may be that metals with large electronegativity values tend to have also large work functions.

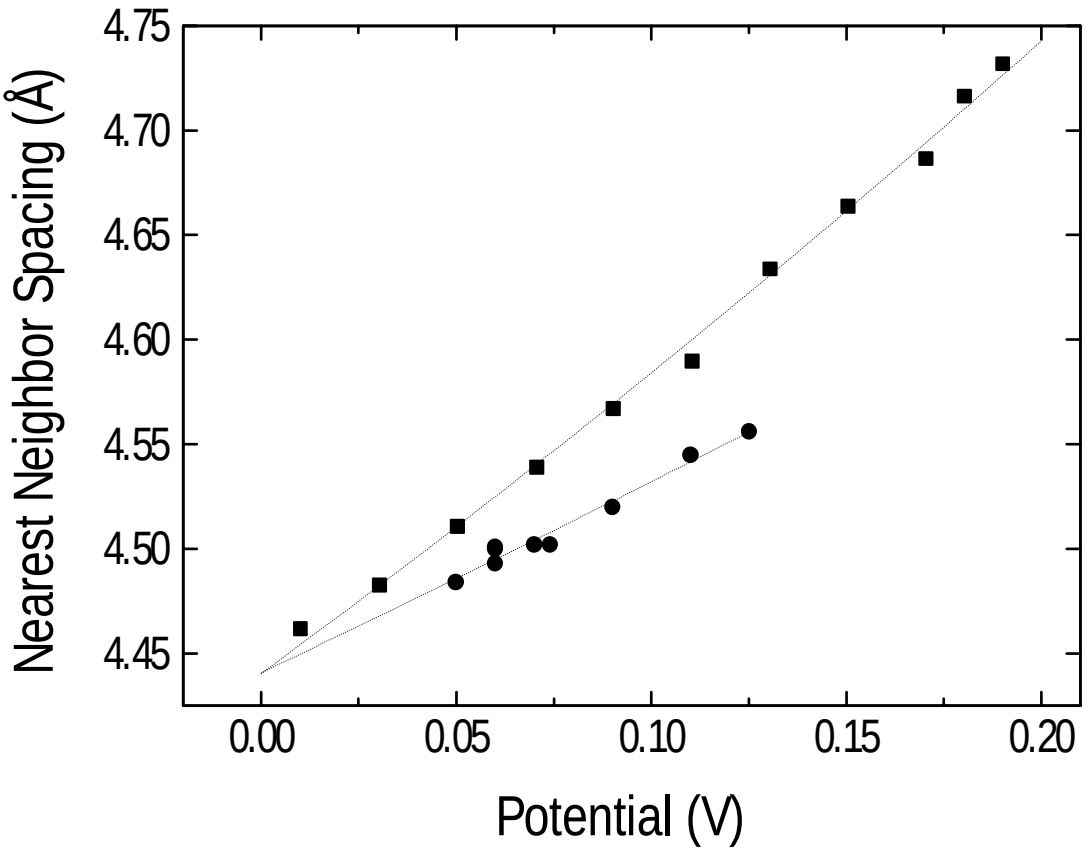

Figure 4-4: Compression curves for UPD Bi monolayers: Bi/Au(111) (circles) [6] and Bi/Ag(111) (triangles) [4]. The fits to data are indicated with dotted lines.

Despite the presence of electrolyte, the electrochemically deposited 2D metals exhibit the compression properties consistent with the simplest theoretical model. The principal deviation from the ideal behavior, parameterized by Z_{eff}, is a measure of the chemical interaction between the 2D metal and the underlying substrate. At the bulk deposition potential, in which 2D and 3D metal coexist in equilibrium, the 2D lattice parameter has the same value on all substrates. Our results for Pb monolayers appear to generalize to Tl and Bi as well.

4.3 References

[1] O. Magnussen, J. Holtos, R. Nichols, D. Kolb, and R. Behm, Phys. Rev. Lett., **64**, 2929 (1990).

[2] C.-H. Chen and A. A. Gewirth, Phys. Rev. Lett., **68,** 1571 (1992).

[3] S. Manne, P. Hansma, J. Massie, V. Elings, and A. Gewirth, Science, **251**, 183 (1991).

[4] M. F. Toney, J. G. Gordon, M. G. Samant, G. L. Borges, D. Wiesler, D. Yee, and L. B. Sorensen, Langmuir, **7**, 796 (1991).

[5] M. F. Toney, J. G. Gordon, M. G. Samant, G. L. Borges, and O. R. Melroy, Phys. Rev. B, **45**, 9362 (1992).

[6] C.-H. Chen, K. D. Kepler, A. A. Gewirth, B. M. Ocko, and J. Wang,

[7] J. Wang, R. Adzic, and B. Ocko, J. Phys. Chem., **98**, 7182 (1994).

[8] M. F. Toney, J. G. Gorden, M. G. Samant, G. L. Borges, and O. R. Melroy,

[9] D. M. Kolb, *Advances in Electrochemistry and Electrochemical Engineering, Vol. 11*, Eds. H. Gerischer, and C. W. Tobias (Wiley-interscience, New York, 1978).

[10] J. G. Dash, *Films on Solid Surfaces*, (Academic Press, New York, 1975).

[11] Y. S. Chu, I. K. Robinson, and A. A. Gewirth (to be published).

[12] J. N. Jovic´eivc´, V. D. Jovic´, and A. R. Despic´, Electrochimica Acta, **29**, 1625 (1984).

[13] N. Ashcroft and N. D. Mermin, *Solid State Physics* (Saunders, Philadelphia, 1976).

[14] A. J. Bard and L. R. Faulkner, *Electrochemical Methods*, (John Wiley & Sons, New York, 1980).

[15] W. B. Pearson, *The Crystal Chemistry and Physics of Metals and Alloys*, (Wiley-Interscience, New York, 1972).

[16] H. O. Pritchard and H. A. Skinner, Chem. Rev., **55**, 745 (1954).

[17] L. Pauling, *The Nature of Chemical Bond* (3rd. ed. Cornell University Press, Ithaca, 1960).

5. Monolayer Oxygen Structure on Cu(111)

As discussed in chapter 3, the Pb UPD process on Cu(111) was speculated to interfere with the simultaneous adsorption/desorption of oxygen or chloride. Because of the Pb atoms on the surface, which are strong X-ray scatterers, the structure of oxygen or chloride could not be measured. In this chapter, the structure of the bare Cu(111) surface is examined in a Pb-free electrolyte.

5.1 Introduction

Structure of metal/electrolyte interface is the fundamental question in electrochemistry, because the interfacial structure significantly influences the electrochemical reactivity. In particular, the structure of copper/water interface is of significant importance because of its relevance to the corrosion behavior of this material. However, accurate and reliable structural characterization of the copper/water interface on atomic level resolution is quite challenging because of the difficulties in obtaining atomically smooth and clean surface to performed *in situ* experiments.

Previous studies have shown evidences of ordered monolayer oxygen structures on low index copper surfaces in liquid environment. Using *in situ* AFM (atomic force microscopy), Gewirth et al. observed an ordered $(\sqrt{2} \times \sqrt{2})R\,45°$ oxygen adlayer in dilute acid solutions at pH 2 [1] and c(2×1) and c(3×1) oxygen chain structures on Cu(110) surface in dilute acid solutions at pH 2.5-2.7 [2]. In both systems, the oxygen adlayer was observed at potentials near the rest potential while the clean substrate lattices was observed at the more negative potentials. The presence of oxygen adlayer on copper surface in acid solutions has significant thermodynamic implication because the bulk copper oxide is expected to be unstable at pH < 3.5 at rest potential

[3].

Despite the absence of direct observation of any ordered oxygen adlayer structure on Cu(111), there have been indirect evidences for the existence of oxygen adlayer. Sigenthaler et al. [4] and Vilche et al. [5] reported voltammetric features of adsorption and desorption of a oxygen monolayer on Cu(111) surface in perchloric acid at a pH ranging from 0.5 to 3.5. Bradley et al. discovered that the second harmonic generation (SHG) signals from the Cu(111) surface in electrochemical environment were different from those from the Cu(111) surface in UHV, and they interpreted this discrepancy due to the formation of an oxygen adlayer on the Cu(111) surface [6]. LaGraff et al. discovered the correlation between the AFM tip-induced enhancement of Cu deposition on the low index copper surfaces and their reactivity toward oxygen adlayer formation in the electrochemical environment. Small but positive enhancement on the Cu(111) surface was interpreted as the presence of oxygen adlayer with relatively weaker Cu-O binding [7]. All these indirect evidences point to the presence of oxygen adlayer on Cu(111) surface, which may be disordered and weakly bound to the surface and therefore is difficult to be imaged with AFM. However, Brisard et al. suggested that the voltammetric features attributed to the adsorption/desorption of oxygen on Cu(111) could be actually due to chloride present as a trace impurity in electrolyte [8].

The oxygen structure on copper surfaces have been extensively studied in UHV conditions. In all cases, significant rearrangement (reconstruction) takes place, and no simple adsorbate structures exist except at low temperature. Oxygen has been reported to form $(2\sqrt{2}\times\sqrt{2})R\,45°$ structure on Cu(100) [9,10,11,12]. A low coverage c(2×1) and high coverage c(6×2) oxygen structure has been reported on Cu(110) [13,14,15,16,17]. At room temperature, the oxygen structure on Cu(111) has been considered to be disordered [18,19,20]. On the other hand,

ordered "29" oxygen structure with large unit cell, (29 and 44 times the (1x1) unit cell) has been reported at 450° C [21], but the details of these structure have not been solved, yet. Some of the important structural features of bulk Cu_2O (cuprite) and O/Cu surface systems are compared in Tab.5-2.

5.2 Results

5.2.1 Voltammetry

The cyclic voltammetry of the electropolished Cu(111) single crystal in 0.1 M $HClO_4$ measured in the electrochemical X-ray cell is shown in Fig. 5-2. The dotted line shows the initial cyclic voltammetry. It is almost featureless, except the tail of the Cu dissolution beginning around 0 V and a very broad cathodic feature C_2, which is not shown well because the upper potential limit was set too high but shown better in the bottom panel of Fig. 5-4. As long as the cathodic potential limit was above the onset of the hydrogen evolution, the voltammetric response remained the same. After a single excursion to about -0.7~ -0.8 V vs. Ag/AgCl (3M KCl), into hydrogen evolution, the subsequent voltammetric response dramatically changed, exhibiting a well-defined

system	O/Cu(110)	O/Cu(110)	O/Cu(100)	bulk Cu_2O
known structure	(2×1)	c(6x2)	$(2\sqrt{2}\times\sqrt{2})R45°$	cubic
O coordination no.	4	4	4	4
Avg. Cu-O length	1.91 Å	1.90 Å	1.89 Å	1.85 Å
O-Cu-O unit	3.62 Å	3.65 Å, 3.71 Å	3.60 Å, 3.66 Å	3.69 Å
∠O-Cu-O	178°	179°, 169°	161°, 167°	180°
∠Cu-O-Cu	178°	104°, 166°	161°	109.5°

Table 5-2: Comparison of structural features for bulk Cu_2O and O/Cu surface systems. The details of the O/Cu(111) structure are still unknown. This table is obtained from ref. [22]

cathodic peak, "C_1", and broader anodic features, A_1, A_2, and A_3. These features were strongly dependent on the limits of the potential cycle. As the upper potential limit was decreased, the size of the cathodic peaks decreased. Likewise, as the lower limit was increased, the anodic peaks became smaller, and eventually the voltammetry changed back to the initial response shown as the dotted line. The voltammetry obtained in a clean glass cell using MSE (mercury/mercurous sulfate reference electrode, $Hg/Hg_2SO_4/K_2SO_4$ (saturated)) is almost identical to the voltammetry taken in the insert. However, the minor feature A_2 was absent in the voltammetry taken in the glass cell, and it might be due to small contamination. The anodic feature, A_1, was not pronounced unless the potential scan rate was low (< 3 mV/s, see the bottom panel of Fig. 5-4). The charge

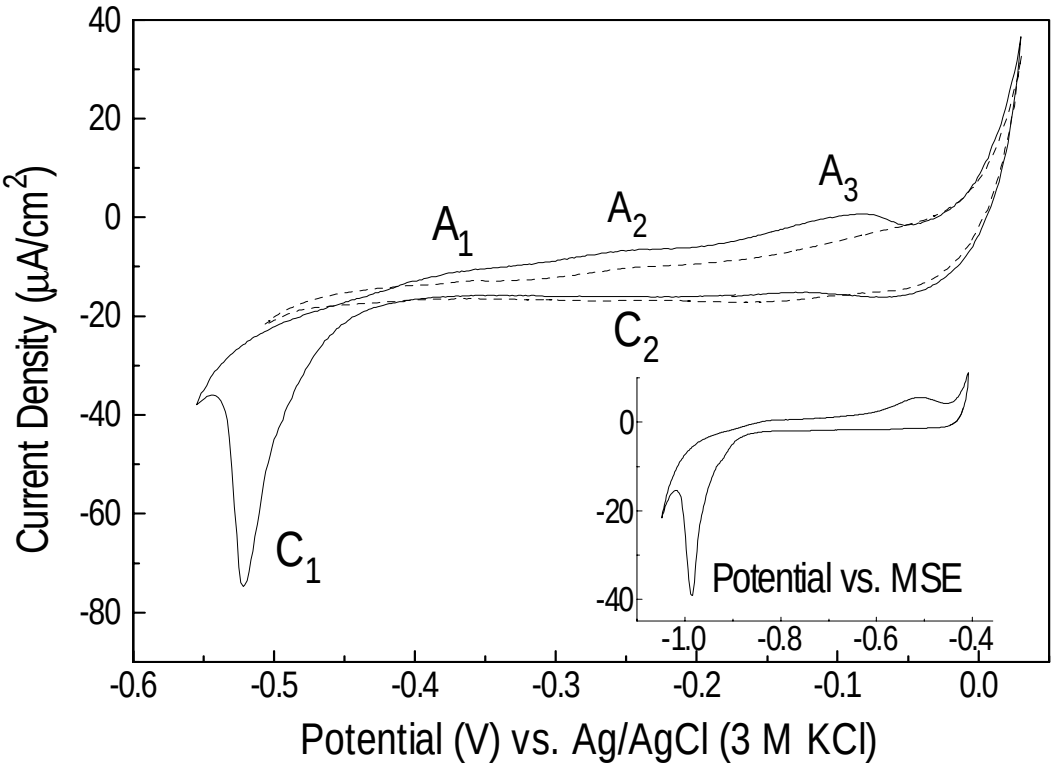

Figure 5-2: Voltammetry of the electropolished Cu(111) surface in 0.1 M $HClO_4$ taken at 10 mV/s in the X-ray cell. The voltammetric response changed from the dotted curve to the solid curve after an excursion to -0.8 V. There is a single sharp cathodic peak, "C", but there are a few broader anodic features, A_1, A_2, and A_3 . A virtually identical voltammetric response was obtained in a clean glass cell with MSE reference electrode (see the insert).

under the cathodic peak after baseline correction was about 150 μ/cm^2. The voltammetry of the electropolished Cu(111) in 0.1 M H_2SO_4 was virtually identical to the ones shown here in 0.1 M $HClO_4$. Similar voltammetries were reported previously [4,5, 6]. However, they are different from one another to some degree. In the voltammetry obtained by Siegenthaler et al. [4] (at 10 mV/s, in 0.01 M $HClO_4$), the anodic and the cathodic peaks were separated by about 410 mV. Under the same condition, Vilche et al. reported the potential separation of about 300 mV. In our voltammetry, the corresponding potential separation was about 520 mV. The voltammetry of Brisard et al. lacked a sharp cathodic peak before the onset of hydrogen evolution, exhibiting only a shoulder [6]. However, it displayed a broad anodic peak similar to "A_3" and a very broad cathodic peak about 200 mV negative of the anodic peak, similar to "C_2". Brisard et al. demonstrated that addition of a small amount of chloride produced voltammetry similar to that of Vilche et al. [5]. However, their voltammetry obtained in the chloride-containing electrolyte was much different from our voltammetry presented here. Their voltammetry showed only a very sharp peak in each scan direction, separated by only about 200 mV, with no other broad features. Since the voltammetry of the Cu(111) surface is very sensitive to the details of the surface treatment and there is no consensus on a clean Cu(111) voltammetry, it is difficult to judge the level of "cleanness" from the features in the voltammetry alone.

5.2.2 *In situ* surface diffraction

Crystal truncation rod measurement (CTR) is a well-proven technique to measure the surface structure of solids. In order to investigate if the voltammetric features shown in Fig. 5-2 correspond any physical change in the surface structure, the intensity of reflectivity (zeroth order rod or 00L rod) at (0, 0, 2.1) was monitored as the potential was cycled. L=2.1 was chosen to monitor the surface structural change because the change in the intensity at this point, being close

to the half way between two Bragg peaks, (0,0,0) and (0,0,3), was expected to reflect the change in the surface structure, while the intensity was large enough to provide good statistic reliability in narrow time intervals. Fig. 5-4 shows the reflectivity intensity during a full potential cycle at 1 mV/s. The intensity started to increase as the potential was swept across the cathodic peak, "C_1" and started to decrease again roughly as the potential was scanned through the anodic feature "A_1". The voltammetric response during the reflectivity measurements could not be measured, but the voltammogram in the bottom panel of Fig. 5-4, measured at 2.5 mV/s, is probably very close to the actual response. The reflectivity scan indicates the surface structure in a narrow potential window just negative of the cathodic peak (near the onset of hydrogen evolution) is substantially different from the surface structure outside this window.

In order to investigate the atomic details of the structure of the Cu(111) surface, the entire

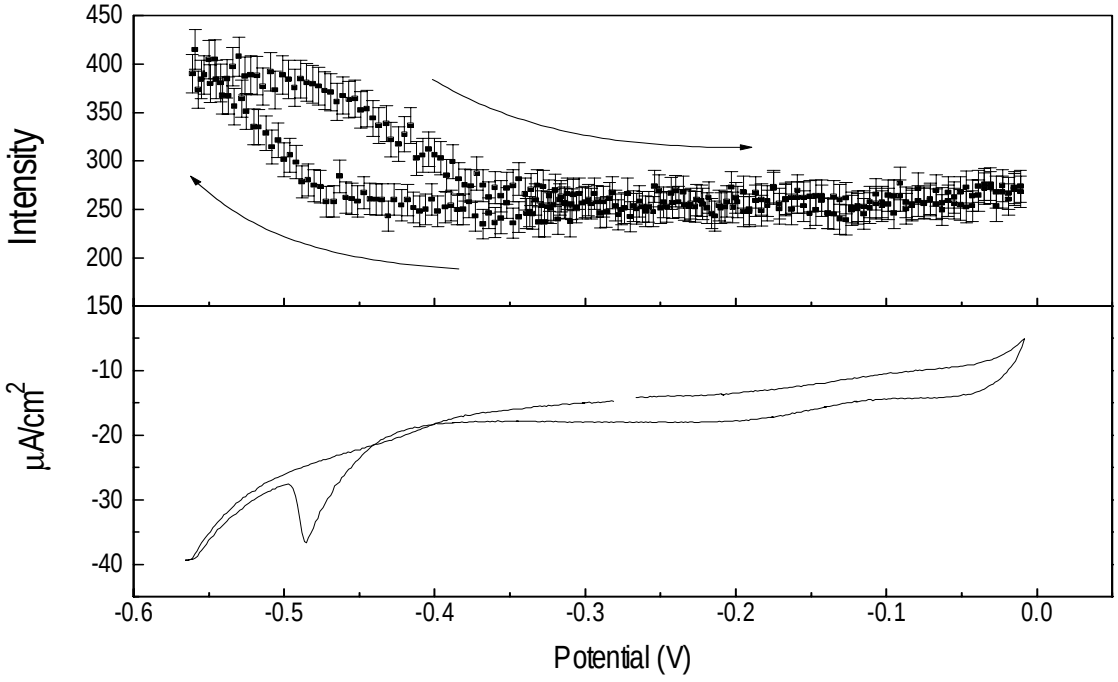

Figure 5-4: : The reflectivity intensity at (0, 0, 2.1) vs. potential. The change in the reflectivity intensity shows a good correlation with the voltammetric features, "C_1" and "A_1" (see Fig. 5-2). The voltammogram in the bottom panel was measured at 2.5 mV/s.

curves of the reflectivity (00L rod) and 10L rod were measured at two potentials, -0.05 V (just below the dissolution of Cu), and -0.60 V (just below the cathodic peak). The data are shown in Fig. 5-6. Each data point was obtained by integrating the ϕ-rocking curve through the CTR peak,, to remove the background due to scattering from the capillary electrolyte layer and the poly-propylene membrane. The divergent behavior at L=3 and 6 in the 00L rod is due to $(1,1,1)_{cubic}$ and $(2,2,2)_{cubic}$ Bragg peaks of the underlying Cu(111) substrate. Likewise, the peaks at L=1 and 4 in the 10L rod are $(-1, 1, 1)_{cubic}$ and $(0,2,2)_{cubic}$ substrate Bragg peaks. The different surface structures at the two potentials are evident from the large difference in the rod profile between the Bragg peaks.

Using simple models of atomic layers, the 00L and 10L rods were fitted simultaneously in order to reduce systematic errors, and the fitting results are listed in Tab.5-4 and plotted in Fig. 5-6. The data taken at -0.60 V were fitted using the Cu(111) bulk plus two relaxed topmost copper layers. For the relaxed layers, their positions and Debye-Waller parameters were all allowed to vary (see section 3.5 for details). For the Cu(111) bulk, the atomic positions and Debye-Waller parameters were fixed at their bulk values. This simple model of Cu(111) surface fitted the data with χ^2 =1.7. In order to improve χ^2, the coverage of the topmost copper layer was allowed to vary. But the result was insignificant differences. According to the fitting results, at -0.60 V, the Cu(111) surface was virtually the same as the ideally terminated Cu(111) surface. No significant modification of the surface was noted except the enhancement of σ, the Debye-Waller parameter expressed as root-mean square (rms) atomic displacement, from the bulk value of 0.085 Å. The enhancement of rms atomic displacement for the surface layer has been observed for many

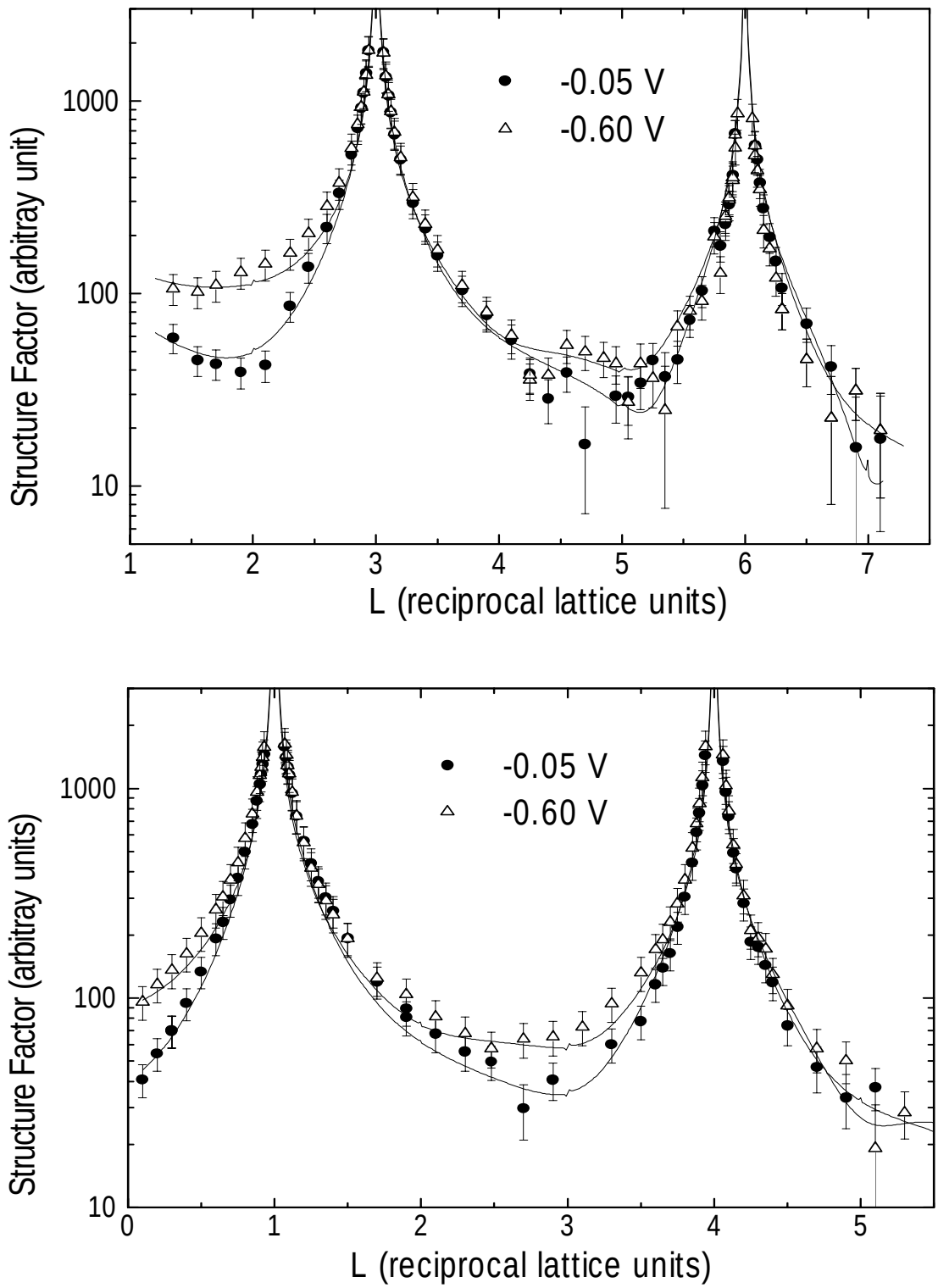

Figure 5-6: CTR of the Cu(111) surface at two potentials, -0.05 V and -0.60 V; 00L rod (Top) and 10L rod (Bottom). The data taken at -0.05 V and -0.60 V were shown as open triangles and solid circles, respectively. The solid lines are the fits to the data

surfaces in contact with electrolyte and so appears to be a general phenomenon [23, 24]

Fitting the data taken at -0.05 V required much more attention. The reduced structure factor at midpoint of the Bragg peaks indicates that the surface may be rougher. In order to model the roughness, a "β parameter" model was used, which has been found to work for a variety of samples, previously. In this method, the surface roughness is modeled by an exponential distribution of partially occupied layers; layer 0 is assumed to be fully occupied, layer 1 above layer 0 has a fraction of β sites filled, layer 2 has fraction β^2 and so on [25]. Using the β description of roughness, the data at -0.05 V were compared with a model of a Cu(111) surface with two relaxed top copper layers. The data were reasonably fitted with $\beta \sim 0.4$ and $\chi^2 = 1.3$. In order to improve the fit, a separate Cu layer was added on the rough Cu(111) model surface. This improved the fit, yielding $\chi^2 = 1.0$ and the coverage, $\theta_{Cu} = 0.15$. However, the partially occupied topmost copper layer was significantly contracted. The Cu-Cu bond length, 1.9 Å, based on the layer spacing, was too short to be a realistic Cu-Cu bond length, because the Cu-Cu bond length in the bulk copper is 2.56 Å. Thus, an oxygen layer was used instead in the model to fit the data, which is a more appropriate choice for the electrochemical reason [4,5]. A layer of oxygen atoms placed at the 3-fold hollow sites of the substrate also produced an excellent fit ($\chi^2 = 1.0$), but no satisfactory fit was obtained with oxygen atoms at the top sites. The fitting results are

E (V)	atom	spacing (Å)	relaxation (%)	σ (Å)	coverage
-0.60	Cu	2.082 ± 0.005	-0.24 ± 0.24	0.13 ± 0.05	1 (fixed)
	Cu	2.082 ± 0.008	-0.24 ± 0.36	0.19 ± 0.10	1 (fixed)
-0.05	Cu	2.104 ± 0.008	+0.8± 0.4	0.12 ± 0.06	β=0.4
	Cu	2.022 ± 0.009	-3.1 ±0.4	0.15 ± 0.08	
	O	1.19 ± 0.07		0.14 ± 0.25	0.68 ± 0.15

Table 5-4: Fitting results.

listed in Tab.5-4. The coverage of oxygen was 0.68 ± 0.15, and the calculated average Cu-O bond length, based on the oxygen-copper layer spacing of 1.19 ± 0.07 Å, was 1.90 ± 0.11 Å. This is consistent with the known Cu-O bond length listed in Tab.5-2. According to the fitting analysis, the layer spacings of the first two copper layers were found significantly modified; the first copper layer was significantly contracted while the second layer was slightly expanded. This may be due to strong binding between oxygen and copper, which could alter the electronic density of the topmost copper layer.

Brisard et al. indicated that the cathodic voltammetric peak might be due to trace amount of chloride in the electrolyte instead of oxygen [8]. In order to investigate this possibility, the data taken at -0.05 V were fitted with an alternate model consisting of the Cu(111) surface with two relaxed Cu layer and a single chloride layer. This model produced basically the same results, except that the coverage of the chloride layer was 0.30 ± 0.07. The chloride layer spacing was almost the same as the oxygen layer spacing, giving rise to the average Cu-Cl bond length of 1.89 ± 0.10 Å. However, this is value is too small to be a realistic Cu-Cl bond length, considering the Cu-Cl bond length of 2.34 Å found in bulk CuCl [26].

The fitting results were almost independent whether the topmost layer was copper, oxygen, or chloride. The only difference among the three model was the coverage, θ, of the top layer, but it was found to scale with *Z*, the number of electrons in atom (i.e. $\theta_{Cu}/Z_{Cu} \approx \theta_O/Z_O \approx \theta_{Cl}/Z_{Cl}$), as expected. Effectively, there is only one solution for the fit. The change in the coverage from Cu to O and to Cl was due to the difference in their X-ray scattering cross sections. Thus, it is impossible to distinguish based on the qualitiy of the fit alone, whether the deviation of the CTR profiles at -0.05 V from those of the ideally terminated Cu(111) surface was due to surface roughening, adsorption of oxygen, or adsorption of chloride. The surface roughening model is

unlikely because it is difficult to produce a current response as seen experimentally in Fig. 5-2. The adsorption/desorption of chloride could be responsible for the observed voltammetry of Cu(111) surface. However, the consideration of the bond length can also rule out adsorption of chloride as a likely candidate.

In the aforementioned fitting analysis, the oxygen atoms were placed on the FCC sites of the substrate. On the Cu(111) surface, there are two 3-fold hollow sites, FCC sites and HCP. The FCC sites are the sites for conserving the cubic symmetry, while the HCP sites are the stacking fault sites. Although slight coupling with other parameter were found, the fit did not show any particular preference whether oxygen atoms were on FCC or HCP sites.

In order to learn more definite structure of the oxygen adlayer on Cu(111), the in-plane oxygen diffraction peaks were searched along the high symmetry directions in the reciprocal. space. However, no ordered diffraction patterns other than those of the substrate were observed, and the oxygen monolayer is concluded to exhibit no in-plane order. The proposed structure of the adsorbed oxygen monolayer on Cu(111) is shown in Fig. 5-8.

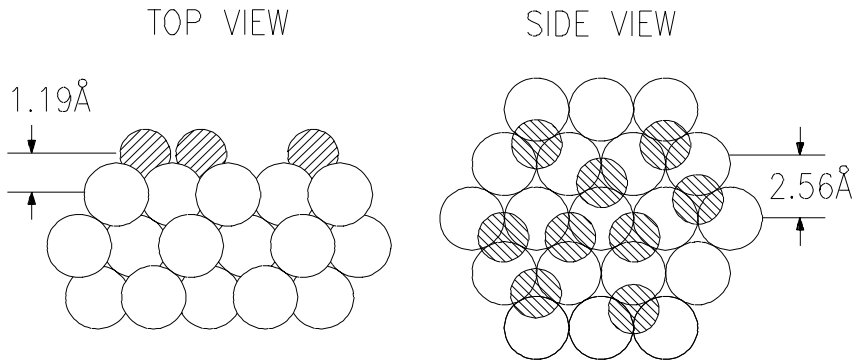

Figure 5-8: The proposed structure of an oxygen monolayer on Cu(111). Although oxygen atoms (hatched circles) occupy the 3-fold hollow substrate sites, there is no long-ranged in-plane order.

5.3 Discussion

The oxygen structure observed in this study is different from the "29" oxygen structure observed in UHV which is the oxygen induced reconstruction of the Cu(111) surface found after annealing at 450° C [22]. The oxygen structure observed here is due to adsorption of oxygen not the reconstruction of the surface. The oxygen structure on the Cu(111) electrode, observed in this study, lacked the in-plane superstructure, while it exhibited a well-defined surface normal structure.

Since hydrogen has a very small X-ray cross section and its form factor falls very rapidly with $\vec{q}$ (consequently with L since $\vec{q} \propto L$), our diffraction measurements are insensitive the presence of hydrogen. Therefore, the observed oxygen monolayer could be a monolayer of hydroxide (OH^-) with the oxygen bound to copper. The observed pH dependence of the voltammetry indicates the adsorbed species is probably OH^- [4]. In addition, since the charge required to desorb a hydroxide monolayer of coverage 0.68 would be about 190 $\mu C/cm^2$, and 380 $\mu C/cm^2$ for oxygen, the observed charge transfer in the voltammetry of about 150 $\mu C/cm^2$ (see Fig. 5-2) is more consistent with the interpretation that the adsorbed species is actually hydroxide.

Toney. et al. observed a similar change in the reflectivity profile of the Ag(111) electrode with the potential in 0.1 M NaF [27]. A significant depression near L=1.7 and a relatively small depression near L=5 are seen in their reflectivity curve measured at -0.12 V vs. Ag/AgCl (3M KCl), displaying much similarity with our reflectivity curve measured at -0.05 V. Their reflectivity curve measured at -0.9 V is also very similar to our data taken at -0.60 V. However, their interpretation of the change in the reflectivity profile is totally different. They attributed the change in the reflectivity profile to the rearrangement of the dipole orientation responding to the change in the electrode potential with respect to the PZC (potential of zero charge). Instead of a layered model,

they used continuous distribution of water density to account for 3 ~ 4 water layers near the surface. Their density of water was modeled by a rather arbitrary arrangement of asymmetric, symmetric Gaussian functions and error functions. Despite the large number of the fitting parameters, the water density near the surface was found to be unrealistically large, as much as 2.3 times larger than the bulk water. Since the density of adsorbed oxygen can be much larger than the density of the bulk water, re-interpretation of their data based on our model could resolve their controversial conclusion.

According to our X-ray diffraction measurements, the Cu(111) surface is not "bare" for the most of its double-layer potential region; the surface is adsorbed by a partially occupied monolayer oxygen. Only when the potential is significantly decreased to the point of hydrogen evolution, the desorption of oxygen occurs, exposing a clean surface. The adsorbed oxygen monolayer structures have now been observed on all three low index copper surfaces at pH <3.5, in the pH regions where a bulk oxide is thermodynamically unstable [3, see chapter 1]. The presence of a stable 2D oxygen layer in the apparently "forbidden" potential-pH phase space indicates that the oxygen monolayer on copper surfaces has much different thermodynamic properties from the bulk oxide. Furthermore, since the adsorption oxygen is the first step toward bulk oxidation, the structure of oxygen monolayer on Cu(111), observed in this study, may be an important clue to understand the oxidation of copper surfaces.

5.4 References

[1] B. J. Cruickshank, D. D. Sneddon and A. A. Gewirth, Surf. Sci., **281**, L308 (1993).

[2] J. R. LaGraff and A. A. Gewirth, Surf. Sci. **326**, L461 (1995).

[3] M. Pourbaix, *Atlas of Electrochemical Equilibria in Aqueous Solutions* (Pergamon, New York, 1966).

[4] H. Siegenthaler and K. Jüttner, Electroanal. Chem., **163**, 327 (1984).

[5] J. R. Vilche and K. Jüttner, Electrochim. Acta. **32**, 1567 (1987).

[6] R. A. Bradley, K. A. Friedrich, E. K. L. Wong and G. L. Richmond, J. Electroanal. Chem., **309**, 319 (1991); E. K. L. Wong, K. A. Friedrich, J. M. Robinson, R. A. Bradley, L. G. Richmond, Vac. Sci, Technol. A, **10**, 2985 (1992).

[7] J. R. LaGraff and A. A. Gewirth, J. Phys. Chem., **99**, 10009 (1995).

[8] G. M. Brisard, E. Zenati, H. A. Gasteiger, N. M. Markovíc, and P. N. Ross, Jr., Langmuir, **11**, 2221 (1995).

[9] F. Jensen, F. Besenbacher, E. Laegsgaard and I. Stensgaard, Phys. Rev., **B 42**, 9206 (1990).

[10] H. c. Zeng, R. A. McFarlane, and K. A. R. Mitchell, Surf, Sci. **208**, L7 (1989).

[11] I. K. Robinson, E. Vlieg, and S. Ferrer, Phys. Rev. B **42**, 6954 (1990).

[12] M. C. Asensio, M. J. Ashwin, A.L.D. Kilcoyne, D. P. Woodruff, A. W. Robinson, T. Linder, J. S. Somers, D. E. Ricken, and A. M. Bradshaw, Surf, Sci. **236**, 1 (1990).

[13] R. R. Parkin, H. C. Zeng, M. Y. Zhou, and K. A. R. Mitchell, Phys. Rev. B **41**, 5432 (1990).

[14] R. Feidenhans'l, F. Grey, R. L. Johnson, S. G. J. Mochrie, J. Bohr, and M. Nielson, Phys Rev. B **41**, 5420 (1990).

[15] R. Feidenhans'l, F. Grey, M. Nielson, F. Besenbacher, F. Jensen, E. Laegsgaard, I. Stensggard, K. W. Jacobsen, J. K. Nørskov, and R. L. Johnson, Phys Rev. Lett. **65**, 2027 (1990).

[16] D. Coulman, J. wintterlin, J. V. Barth, G. Ertl, and R. J. Behm, Surf. Sci. **240**, 151 (1990).

[17] G. Dorenbos, M. Breeman, and D. O. Boerma, Phys. Rev. **B47**, 1580 (1993).

[18] L. H. Dubois, Surf. Sci., **119**, 399 (1982).

[19] H. Niehus, Surf. Sci. **130**, 41 (1983)

[20] J. Haase and J.-J. Kuhr, Surf. Sci. **203**, L695 (1988).

[21] F. Jensen, F. Besenbacher, and I. Stensgaard, Surf. Sci. **269/270**, 400 (1992).

[22] W. Liu, K. C. Wong, H. C. Zeng and K. A. R. Mitchell, Prog. in Surf. Sci., **50,** 247 (1990).

[23] J. Wang and B. M. Ocko, Phys. Rev. **B46**, 10321 (1992).

[24] J. Wang, R. Adzic, and B. Ocko, J. Phys. Chem. **98**, 7182 (1994).

[25] I. K. Robinson and D. J. Tweet, Rep. Prog. Phys. **55**, 599 (1992).

[26] R. W. G. Wyckoff, *Crystal Structures*, 2nd ed., Vol. 1 (Wiley, New York, 1963).

[27] M. F. Toney, J. N. Howard, J. Richer, G. L. Borges, J. G. Gordon, O. R. Melroy, D. G. Wiesler, D. Yee, and L. B. Sorensen, Nature, **368**, 444 (1994).

6. Aqueous Oxide on Cu(111) at pH 4.5

In the previous chapter, the structure of the specifically adsorbed oxygen adlyaer on Cu(111) under electrolyte at pH 1 was discussed. Since the thermodynamics at copper/water interface forbids the formation of bulk oxide at pH < 3.5 (as explained in Pourbaix diagram in chapter 1), the stable 2D oxygen at pH 1 is analogous to a metal UPD monolayer before bulk deposition, a precursor to the bulk phase. In this chapter, the formation of bulk oxide on Cu(111) is discussed.

6.1 Introduction

Fundamental understanding of metal oxidation processes is an important problem in many disciplines of physical science. In particular, oxidation of copper has attracted attention because of strong interest to understand the corrosion of this widely used metal. Dry oxidation of copper has been studied extensively using a number of techniques such as TEM [1,2] , LEED [3, 4] , RHEED [3], EELS [5], STM [4, 6], and SEXAFS [7]. In these studies, the copper surfaces were cleaned under vacuum and oxidized by dosing oxygen. The growth of cubic cuprous oxide (Cu_2O) or cuprite on the low index copper surfaces was found to be epitaxial with the substrate, and a wide array of growth morphologies were reported, depending on the growth conditions.

By comparison, there exists only small number of reports on the oxidation of copper in the presence of water to investigate the structure and growth properties of the aqueous oxides on copper surfaces. Gewirth et al. reported a $c(2 \times 2)$ oxygen adlayer on Cu(100) [8] and (2×1) and (3×1) oxygen chain structures on Cu(110) [9] in dilute acid solutions (pH 2~3), using *in situ* AFM, which were considered as precursors to bulk oxide growth. Ikemiya et al. investigated the structures of aqueous oxide on Cu(111) and Cu(100) in alkaline solutions at pH 13 and reported the epitaxial Cu_2O structures on both surfaces [10]. The AFM measurements have provided

valuable information on the structure and morphologies of the aqueous oxide. Yet, since this is a prototypical thin-film system, question of epitaxial strain and growth properties are important but still largely unknown. In this study, we investigate using X-ray diffraction, the structure of the aqueous oxide on Cu(111) in a very dilute acid solution at pH 4.5. The focus of this study is to understand how the epitaxial structure of Cu_2O changes with the thickness of the oxide film. In addition, we examine the structure of the native oxide, found upon exposure to air, on the freshly electropolished Cu(111) surface, to understand the differences and similarities between these two oxides formed under different conditions.

6.2 Experiment

Basically, the same experimental procedures and the sample preparations methods described in section 2.4 were employed. However, more caution was used to avoid excessive oxidation after electropolishing, because the electrolyte used was much less acidic. When visible native oxides formed after electropolishing, a drop of 0.1 M $HClO_4$ was put on the sample. This method was very effective in removing the oxide. Then, the sample was rinsed with Millipore water. A double junction Ag/AgCl electrode was used as a reference electrode. The supporting electrolyte was 0.1 M $NaClO_4$, and the pH≈ 4.5 was adjusted with $HClO_4$. The X-ray diffraction measurements were carried at 8.5 keV (λ = 1.46 $Å^{-1}$).

6.3 Structure of bulk cuprite

In order to provide adequate background, the structure of cuprite, Cu_2O with cubic symmetry, is discussed briefly here. Fig. 6-2 shows the structure of cuprite. The primitive unit cell is a cube with a lattice constant, a = 4.2696 Å, and contains two oxygen atoms and four copper atoms [11]. The oxygen atoms form a body centered cubic structure, while the copper

atoms partially occupy the interstitial positions in an alternating pattern. Each copper atom has only two nearest oxygen neighbors, while each oxygen atoms is surrounded by a tetrahedron of copper atoms. The copper atoms are located midway between two oxygen atoms with Cu-O bond length of 1.85 Å. The Cu-Cu separation is 3.01 Å. The [111] surface shown in Fig. 6-2 is constructed by taking a cross section defined by the three corner oxygen atoms. The crystallographic unit cell of $Cu_2O(111)$ is defined by a hexagonal base of length, $a = \sqrt{2}a_o$, and a height, $c = \sqrt{3}a_o$ and contains twice as many number of atoms as the cubic unit cell.

6.4 Results

6.4.1 Native oxides on Cu(111)

Before immersing the Cu(111) sample into the electrolyte, the dry surface of Cu(111) was carefully examined for existence of any native oxide on the surface. Four different electropolished

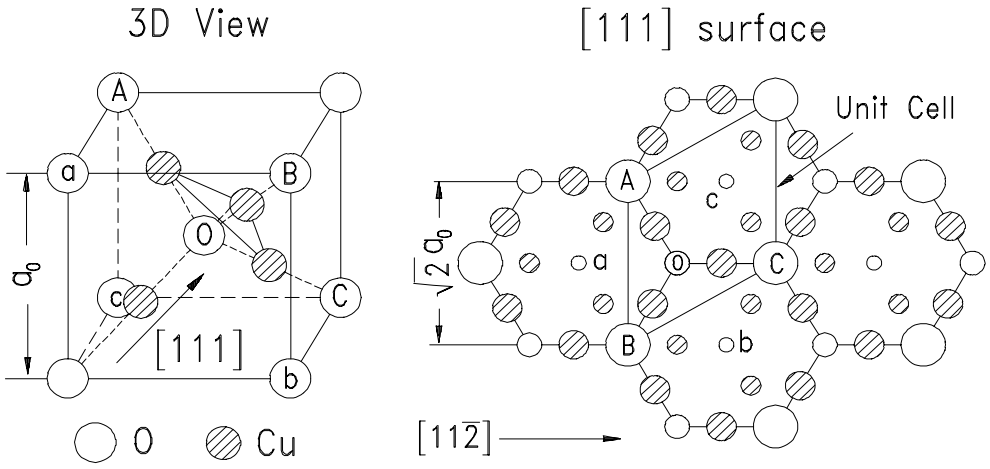

Figure 6-2: Structure of cuprite. Each copper atom has two oxygen atoms as the nearest neighbors, and each oxygen atom is surrounded by a tetrahedron of copper atoms. The top view of the [111] surface is constructed by a cross section containing three oxygen atoms, A, B, and C. The crystallographic [111] unit cell has twice as many atoms as the primitive cubic unit cell, with the hexagonal base of length, $a = \sqrt{2}a_o$, and a height, $c = \sqrt{3}a_o$. In the surface view, all the copper atoms at the (1/4, 1/4, 1/4) positions (see the 3D view) are omitted for clarity.

samples were examined with X-ray diffraction. On all four samples, two distinct epitaxial oxides were found. The diffracted intensities from the two oxides were about the same and resulted in 6-fold symmetric diffraction patterns. Both epitaxial oxides were found to have the diffraction pattern of the cubic cuprite structure (Cu_2O) with their [111] axis parallel with [111] substrate axis. However, they exhibited different in-plane epitaxial relations with the substrate. The models of the two different cuprite structures on Cu(111) surface are shown in Fig. 6-4. In the "aligned' cuprite (Cu_2O) structure, the $[1\bar{1}0]$ oxide axis is parallel with the $[1\bar{1}0]$ substrate axis, while in the "reversed" cuprite $[1\bar{1}0]$ oxide axis is anti-parallel with the $[1\bar{1}0]$ substrate axis. Another way to appreciate the difference between the two structures is that they are related with a 180° rotation about the axis perpendicular to the plane of view.

The details of the native oxide structures were investigated as a function of the film thickness. Since the growth conditions of the native oxide could not be controlled reliably, the initial oxide

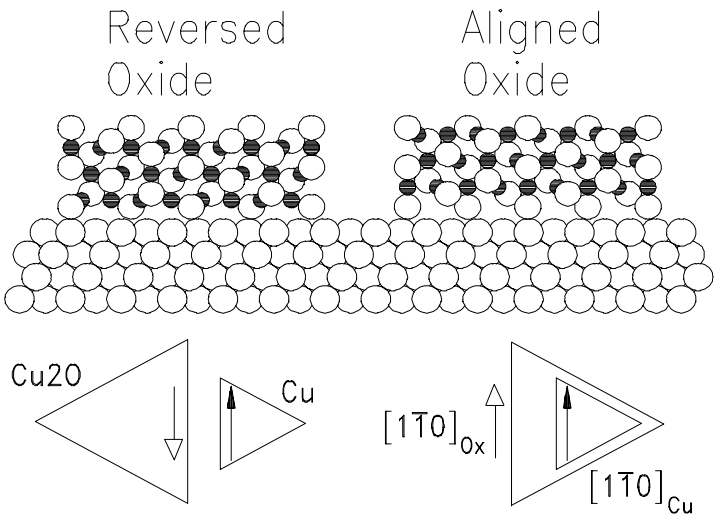

Figure 6-4: Side view of the atomic model of cuprite on the Cu(111) substrate. In the oxide, the oxygen and copper atoms are represented by open and hatched circles, respectively. Both "aligned" and "reversed" oxides have their [111] axis parallel with the substrate [111] axis but with different in-plane epitaxial relations. In the aligned cuprite, $[1\bar{1}0]_{Cu2O}$ // $[1\bar{1}0]_{Cu(111)}$, while in the reversed cuprite, $[1\bar{1}0]_{Cu2O}$ // $[\bar{1}10]_{Cu(111)}$.

film thickness (measured within a few hours since electropolishing) exhibited strong sample dependence. However, all four samples displayed a similar growth trend subsequently afterwards. Fig. 6-6 shows the profiles of the cuprite Bragg peaks at different elapsed times since electropolishing. Peak "A" and peak "B", located approximately at $(0, 0.85, 0.85)_{hex}$ and $(0, 0.85, 1.7)_{hex}$, corresponds to the reversed$(-1, 1, 1)_{cubic}$ and aligned $(0, 0, 2)_{cubic}$ cuprite Bragg peaks, expressed in the cuprite reciprocal lattice units. The diffraction patterns of the aligned, reversed cuprite, and substrate are shown in the bottom panel of Fig. 6-6. The diffraction patterns of the two structures are symmetric with respect the 00L axis. About 9 hours after electropolishing, the

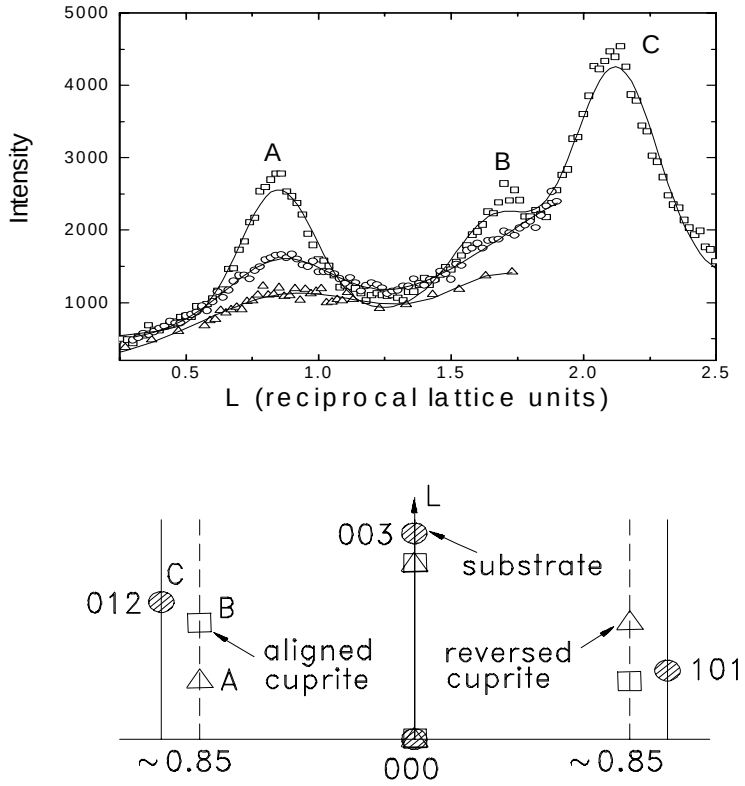

Figure 6-6: The bulk oxide peaks scanned along (0, 0.85, L) direction, taken at different elapsed times since electropolishing on the same sample; 9 hours (triangles), 12 hours (circles) and 23 hours (squares). As shown in the reciprocal space in the bottom panel, peak "A" and peak "B", located approximately at (0, 0.85, 0.85) and (0, 0.850, 1.7), are the reversed and aligned cuprite Bragg peaks. Peak "C" is due to the diffuse scattering from (0, 1, 2) substrate Bragg peak. The lines are multiple Gaussian fits, used to determined the exact peak locations.

cuprite Bragg peaks were very weak and wide. However, about 23 hours after polishing, the intensity of the $(0, 0.85, 0.85)_{hex}$ peak increased by about 4 times, and the width (HWHM) decreased by about 50%. The peak positions changed slightly with time, suggesting large strain in the oxide film.

The dependence of the lattice parameters of the native oxide on the oxide film thickness is displayed in Fig. 6-8. For a comparison purpose, instead of the actual crystallographic lattice parameters, a and c, $a/\sqrt{2}$ and $c/\sqrt{3}$ are shown, which are more convenient quantities for examining the strain of the film, because $a/\sqrt{2} = c/\sqrt{3} = a_0$ =4.270 Å for an unstrained film. Although the natural misfit between cubic Cu_2O (a_0 = 4.270 Å) and copper (a_0 =3.615 Å) is -15.3 %, the in-plane spacing of Cu(111) surface (a = 2.556 Å) and Cu_2O(111) surface (a = 6.038 Å)

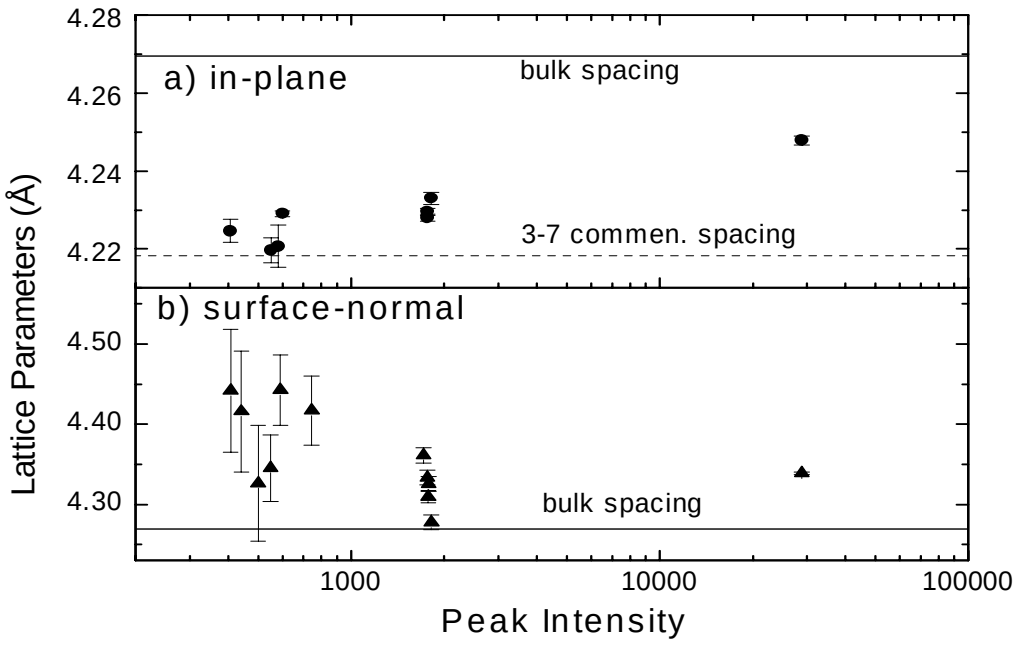

Figure 6-8: In-plane and surface-normal lattice parameters of the cuprite oxide on Cu(111) as a function of the peak intensities. For comparison purposes, $a/\sqrt{2}$, and $c/\sqrt{3}$ are plotted. As the oxide grew thicker, the in-plane lattice parameter increased from a value close to the 3-7 commensurate spacing (4.2175 Å) toward the bulk cuprite spacing (4.2696 Å). The opposite trend was observed for the surface-normal lattice parameter.

are such that the coincidence misfit for 3 $Cu_2O(111)$ unit cells over 7 Cu(111) unit cells is only -1.22 % when the two lattices are aligned. The previous study on the dry oxide [1] and the STM study on the aqueous oxide at pH 13 [10] have suggested the 3-7 commensurate oxide structure. When the oxide film was thin, the in-plane oxide spacing of the oxide was found to be close to this 3-7 commensurate spacing. As the oxide grew thicker, the in-plane spacing approached the bulk cuprite spacing. While the in-plane spacing increased toward the bulk spacing, the surface-normal oxide spacing, decreased toward the bulk spacing from much larger initial values, showing the opposite trend. The direction of the change in the surface-normal oxide spacing can be understood in terms of reducing the compressive epitaxial strain at the interface and conserving the unit cell volume.

To summarize, during the 24 hour period since polishing, the lattice parameter of the oxide did not relax to the bulk value. During the growth of the native oxide, the average unit cell volume was close to the bulk unit cell volume, and no particular correlation with time other than random fluctuations was observed

6.4.2 Voltammetry of aqueous oxidation

The voltammetry of Cu(111) single crystal in 0.1 M $NaClO_4$ (pH 4.5) is shown in Fig. 6-10. Major features of the voltammetry are marked with labels, A, B, and C. The anodic peak, “A”, corresponds to oxidation of the surface, while the cathodic peak, "B”, corresponds to reduction. The tail of the voltammogram, labeled as “C”, is due to reduction of $2H^+$ to H_2. A well defined oxidation peak exists because the surface becomes passivated after initial oxidation in a well deoxygenated electrolyte. The charge transferred during the oxidation or reduction, estimated by integrating this particular voltammogram, is about 150 $\mu C/cm^2$. However, the exact amount of

charge depends critically on the details of the kinetic variables (i.e. scan rate, polarization history, limits of the potential cycle, thickness of the electrolyte film, etc.)

6.4.3 Aqueous oxides

The electrochemically oxidized Cu(111) surface was examined by X-ray diffraction at various potentials after "freezing" the oxidation process. "Freezing" the oxidation process was carried out in the following way. First, the potential was kept cycling while the membrane was inflated. After the surface was completely reduced, the membrane was deflated and the potential was increased slowly (1 mV/s) into the oxidation potential region. After moving into the desired potential, the potential scan direction was reversed, in order to prevent further oxidation. The potential was stopped when the current became slightly negative. During the X-ray measurements, the current density remained small, typically within a few $\mu A/cm^2$. In this way, the extent of oxidation on the Cu(111) surface was controlled accurately and reliably. This freezing method was possible because of the small irreversibility associated with the oxidation/reduction process of the Cu(111)

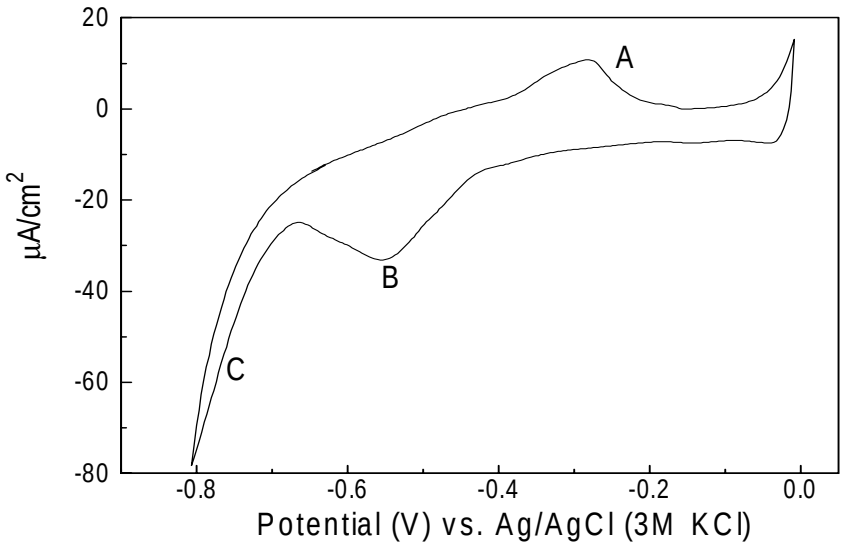

Figure 6-10: Cyclic voltammetry of Cu(111) single crystal in 0.1 M $NaClO_4$ at pH 4.5 measured at 10 mV/s. Peak "A" and peak "B" are due to oxidation and reduction of the Cu(111) surface, respectively. Peak "C" is due to reduction of proton (H^+) to hydrogen gas (H_2).

surface; it requires some overpotential to reduce the surface after it is oxidized, and *vice versa*. Effectively, the freezing procedure is offsetting the overpotential needed to start the oxidation. If no precaution were taken, the oxidation would continue during the measurements, and the data would show significant time dependence. However, complete freezing was not possible over a long time because of the nonnegligible background current and the motion of the diffractometer. If the galvanostatic method were used instead of the potentiostatic method to control the electrochemical reactions, the freezing procedure would not be necessary (see chapter 2).

X-ray diffraction study revealed that the electrochemical oxidation of the Cu(111) surface in 0.1 M $NaClO_4$ at pH 4.5 resulted in the formation of two epitaxial cuprites (the aligned and

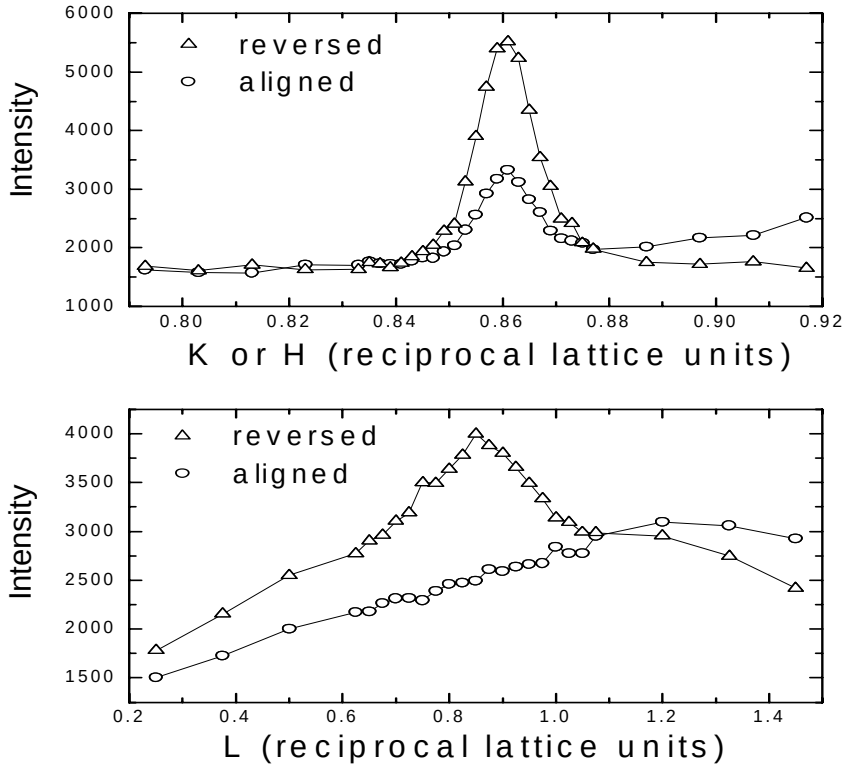

Figure 6-12: Profiles of the aqueous oxide Bragg peaks along the surface-parallel (top panel) and surface-normal (bottom panel) direction at -0.43 V before thick oxide appears. The diffraction peak from the reversed oxide is well-defined in both directions, while the diffraction peak from the aligned oxide is sharp only in the surface-parallel direction. The broad diffused scattering from the nearby substrate Bragg peak make it difficult to extract the true surface-normal profiles of the aligned diffraction peak.

reversed). The diffraction patterns from the epitaxial oxides disappeared completely when the surface was reduced. The epitaxy of the aqueous cuprite oxides was identical to that of the native cuprite oxides. However, the aqueous oxidation exhibited an interesting dependence of the crystallographic orientation of the oxides at the interface. Fig. 6-12 shows the diffraction peaks from the aligned and reversed cuprite. The reversed bulk Bragg peak, found at approximately (0, 0.86, 0.84) (in the substrate reciprocal lattice units), exhibited a well-defined peak in both K-direction (surface-parallel direction or $q_{//}$ -direction) and L-direction (surface-normal direction or $q_{\perp}$-

direction). This indicates that the reversed cuprite has a three-dimensional crystalline structure. However, the diffraction peak from the aligned cuprite is sharp in the surface-parallel direction but very wide in the surface-normal direction. The true line shape in the surface-normal direction is difficult to extract due to the broad diffused scattering from the nearby (1,0,1) substrate Bragg peak. A very wide surface-normal profile indicates that the aligned cuprite is very thin, probably no more than a few monolayers[1]. In addition, the diffraction intensity from the aligned oxide was much smaller that that of the reversed oxide so the diffraction pattern kept the 3-fold symmetry of the substrate. In order to check whether these findings might be due to the diffraction from certain preferentially oriented oxide domains isolated in just on region of the surface, the same scans were made after translating the sample by ± 2 mm with respect to the X-ray beam (the beam size was 0.5×2 mm). However, the same results were obtained for all three parts of the sample, providing a convincing proof that the preferential growth of the reversed cuprite was occurring throughout the entire surface.

---

[1] We define a monolayer as the minimum number of atomic layers that give rise to the in-plane diffraction pattern

In order to study the growth kinetics of the two types of cuprite oxide more systematically, the intensity of both the reversed and aligned cuprite diffraction peaks were monitored simultaneously as the potential was slowly scanned. Simultaneous observation of two diffraction peaks, separated far apart in reciprocal space, was possible because of the high speed of the custom-designed Kappa diffractometer [12]. As shown in Fig. 6-14. the growth of aqueous cuprite on the Cu(111) surface depends strongly on the crystallographic orientation of the oxides at the

interface. As the potential was increased from -0.6 V to potential "A" (~ -0.43 V) both reversed and aligned cuprites began to form on the surface. Until the point "B" (about -0.3 V), the intensities of both oxides remained almost constant. Within this narrow potential window, the

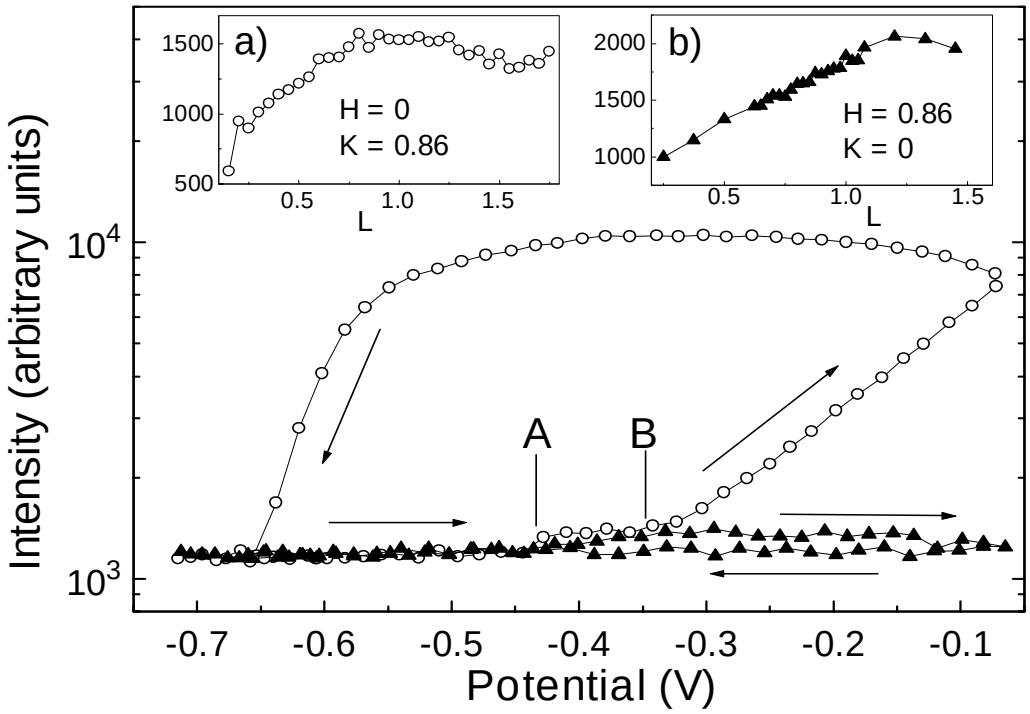

Figure 6-14: Growth of the reversed (open circles) and aligned (solid triangles) cuprites as a function of the potential. The arrows indicate the change in the intensities as the potential was cycled from -0.6 V. For a narrow potential window between "A" and "B", the growth of both oxide appears to be two dimensional evidenced by very wide surface-normal profiles shown in inserts "a" and "b". As the potential increased further, the reversed cuprite grew into the bulk phase, but the aligned cuprite remained two dimensional and became unstable at sufficiently high potentials.

of cuprite which is a single Cu-O bilayer not an entire unit cell.

diffraction peaks of both aligned and reversed oxides were very wide in L-direction, while they were sharp in the in-plane directions. As the potential was increased further, the intensity of the reversed cuprite began increasing exponentially, while the intensity of the aligned cuprite remained constant until it started to drop to the background level at sufficiently high potentials. The intensity of the reversed oxide continued to increase even after the direction of the potential scan was reversed though the rate began to drop. The intensity of the reversed cuprite eventually began to decrease once the potential reached the reducing potential region. At the maximum, there was about 50 times more reversed oxide at the interface than aligned oxide, based on their diffraction intensities.

Monitoring the diffraction peak intensities as a function of the potential has thus provided useful kinetic information on the quantity of the oxide present at different stages of growth. However, it did not provide much information about the structure. In order to investigate how the structure of the reversed cuprite behaves as a function of the film thickness, the following procedure was adopted. After the surface was completely reduced, the potential was increased slowly at 1 mV/s while the membrane was deflated. After stopping the potential at a desired value, the profile of the diffraction peak in both the surface-parallel and the surface-normal directions were measured. This procedure continued for one full potential cycle. Since the thickness of the aligned cuprite was known to be independent of the potential it was assumed the structure did not change either, so this investigation of the structure was performed on the reversed cuprite only.

Fig. **6-16** shows how the lattice spacing of the reversed cuprite varied with the potential. Both the in-plane lattice spacing, $a/\sqrt{2}$, and the surface-normal lattice parameter, $c/\sqrt{3}$, depended very sensitively on the potential. At -0.4 V (the first potential in the cycle), the diffraction peak was very wide in L-direction, and its position could not be determined accurately. At this potential,

the reversed cuprite film was probably no thicker than a few monolayers, and its in-plane lattice spacing was under significant compressive strain (about -1.9 %). As the potential increased from -0.4 to -0.06 V, both the in-plane and the surface-normal lattice spacing increased. At -0.06 V, the in-plane lattice parameter of the reversed cuprite was still under about -1.3 % strain. After the potential scan direction was reversed at -0.06 V, the relaxation of the in-plane lattice parameters still continued but at much lower rate, because the growth rate of the oxide has become reduced significantly by this point as shown in Fig. 6-14. In the potential range from -0.25 V to -0.4 V, no significant changes occurred. A slight increase in the in-plane lattice parameter and considerable increase in the surface-normal lattice parameter were observed at -0.50 ~ -0.55 V. This

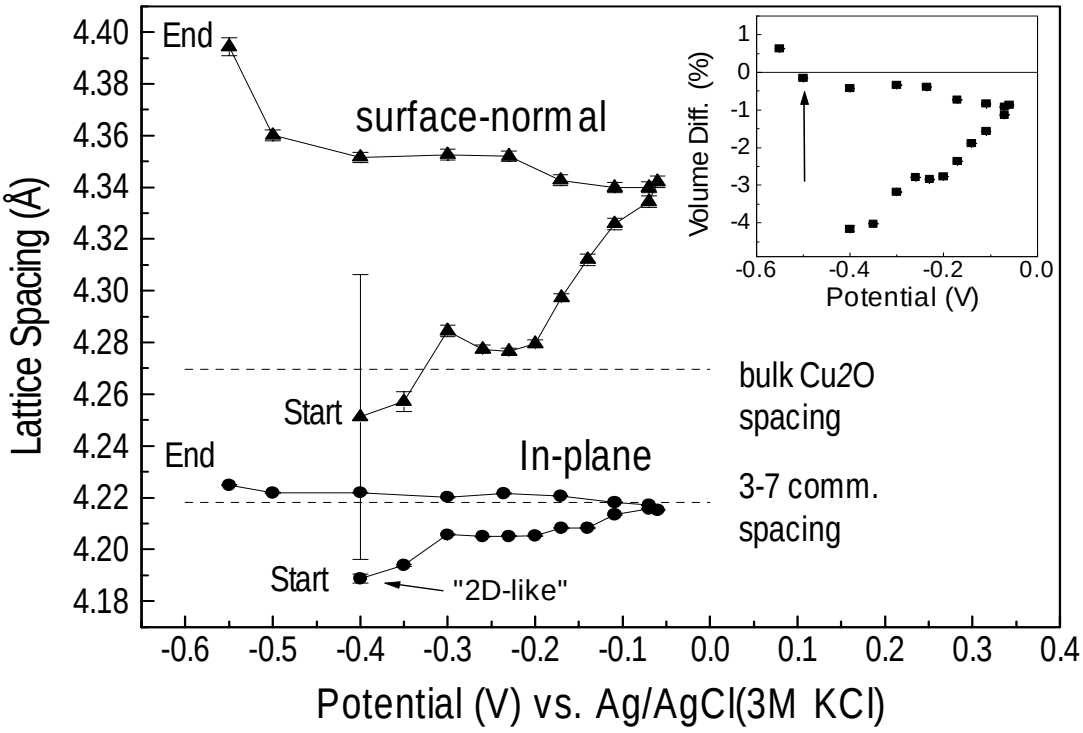

Figure 6-16: Lattice spacings of the reversed cuprite vs. the potential. For the comparison purpose, $a/\sqrt{2}$ (circles) and $c/\sqrt{3}$ (triangles) are plotted. The start and the end point of the potential cycle are shown in the plot. The diffraction peak at -0.4 V (the first data in the series) was very broad in the surface-normal (L) direction, and its position (thus the surface normal lattice spacing) could not be determined accurately. For the reference, the bulk cuprite spacing and 3-7 commensurate spacing are indicated with dotted lines. The insert shows the % deviation of the unit cell volume from the bulk cuprite *vs.* the potential.

phenomenon was due to the reduction of the oxide. In this potential region, the oxide was unstable and was being dissolved while the measurements were made. During the entire cycle, the in-plane lattice parameter was never fully relaxed. Even while the oxide was being reduced, it was under about -1% strain.

The relaxation behavior of the aqueous cuprite film as it thickens was very unusual, especially when compared with the relaxation behavior of the native cuprite film. Both the in-plane and surface-normal spacing relaxed in the same direction. Consequently, the unit cell volume has undergone a monotonic increase from a value about 4% smaller than the bulk volume. At -0.3 V, the unit cell volume was almost completely relaxed (about 99.7 % of the bulk volume), while both in-plane and surface-normal lattice parameters were significantly strained from the bulk values. As the oxide becomes unstable (< -0.5 V, indicated by an arrow in the insert), the unit cell volume became slightly larger than the bulk volume.

Although tremendous effort was made to avoid fluctuation of data points due to growth of oxide during the measurement, the data in Fig. 6-16 does show some fluctuation. The fluctuation of the data can be improved by removing the time dependence. One way to do this is by using the inverse L-width (HWHM) of the diffraction as the independent variable instead of the potential. In a simple diffraction model, the thickness of the film, h, is related to the width (HWHM) of the diffraction peak in the surface-normal direction, ΔL as

$$h = \frac{c}{\Delta L} \qquad (6\text{-}2)$$

where c is the unstrained surface-normal lattice parameter of cuprite and h is the apparent thickness of the film with no resolution correction. In Fig. 6-18, all the data collected for this experiment including the data shown in Fig. 6-16 are plotted against the apparent thickness.

According to the way the integrated intensity and the in-plane lattice spacing depend on the inverse L-width, the data shown in Fig. 6-18 can be divided into four different regions. In region "A", no diffraction pattern from the oxide was observed. In region "B", the in-plane lattice spacing remained constant, while the integrated intensity was very small and did not change much with the thickness. The diffraction pattern in this region was characterized by very wide diffraction profiles in L-direction, and the oxide film was under high epitaxial strain (-2.0 ~ -1.5 %). In region B, the extracted values of the apparent film thickness are subject to large systematic errors because the L-width of the diffraction peak depended strongly on the peak fitting methods and the background subtraction methods. The data shown in this region were obtained in the potential range about -0.43 to -0.4 V.

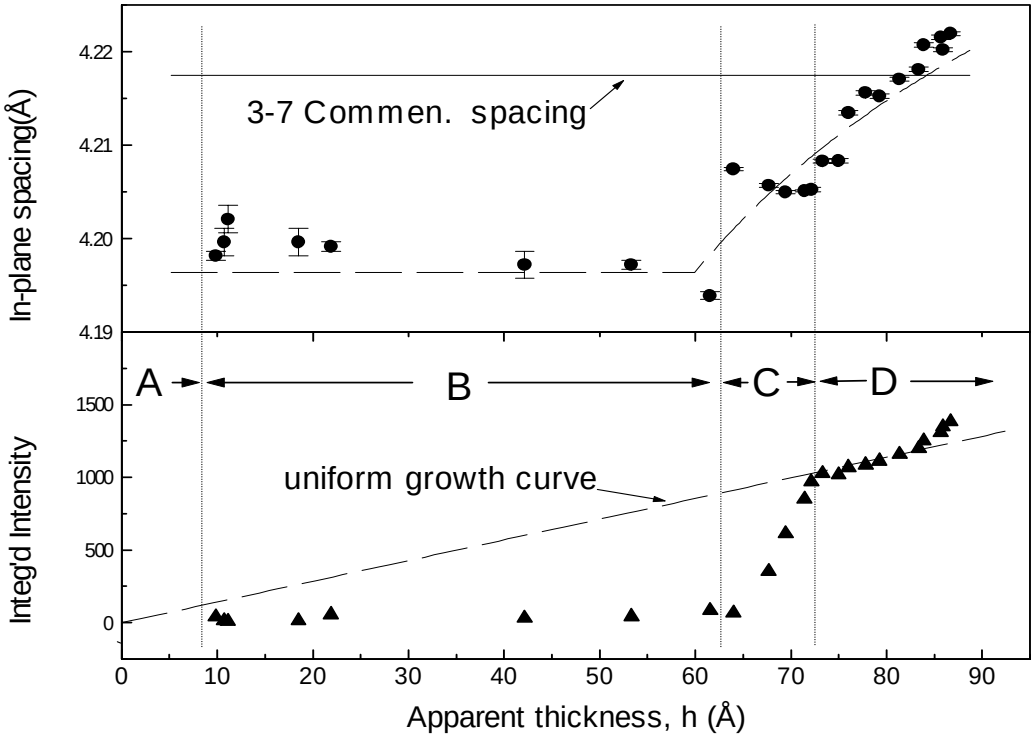

Figure 6-18: The in-plane spacing, $a/\sqrt{2}$, of the reversed cuprite (top panel) and the integrated intensity of the diffraction peak (bottom panel) are plotted against the apparent thickness. According to the way the in-plane spacing and the integrated intensity of the diffraction peak change, there are distinct growth regions. The dashed line in the top figure is the fit to the data using a simple elastic equilibrium theory (see text), and the dashed line in the figure is the expected intensity behavior for uniform growth.

Throughout the growth region "B" and "C", the in-plane lattice parameter increases systematically. This behavior can be compared with Van der Mervwe's equilibrium theory of epitaxy, which predicts that a thin film will be commensurate with its substrate, but will become energetically unfavorable beyond a certain "critical" thickness [13]. In this model, the epitaxial in-plane lattice parameter, a, is found to depend on the thickness of the film, h, in the following way,

$$a = a_0 + \frac{h_c}{h}(a_s - a_0) \quad \text{for} \quad h > h_c, \tag{6-4}$$

where a_0 is the bulk lattice parameter, a_s is the substrate lattice parameter, and h_c is the critical thickness. The solid line Fig. 6-18 is a fit of this functional dependence to the data, which yielded, a_s = 4.196 Å, h_c = 59.9 Å. Although the data exhibit a reasonable trend with the fit, the agreement is not excellent, suggesting the aqueous oxide growth at the Cu(111) surface may be more complicated than the simple equilibrium growth. For example, the in-plane lattice spacing, 4.196 Å, below the critical thickness, can not be explained by the simple epitaxy between the substrate and cuprite, because it does not corresponds to any obvious substrate periodicity.

The boundary between the region "B" and "C" is marked by remarkable change in the rate of increase of the integrated intensity with the film thickness. This change is not due to reversing the potential scan direction, which occurred much later at h =78 Å. Since the integrated intensity of the diffraction peak is proportional to the number of the scatterers, the integrated intensity should be proportional to the thickness if the film is uniform. The obvious deviation of this linear behavior in region A and B indicates that the growth of the oxide film is not uniform, while a uniform growth of the oxide film was observed in region C. Slight deviation from the uniform

growth for the last three data points is due to peak broadening before/during the reduction, which slightly increased the integrated intensity.

It is interesting that no sharp change in the intensity with respect to the potential was observed in Fig. 6-14. One possible reason for it may be the set of data shown in Fig. 6-14 were collected over a period of about 15 minutes, while the set of data shown in Fig. 6-16 and Fig. 6-18 were collected over 2 hours with frequent and long stops during the potential cycle. In addition, the growth of oxide during the later cycle was more extensive (about 5 time more in intensity) than the previous one. Therefore, it is possible that this particular change in the growth kinetics has not occurred during the earlier set of measurements

Based on the diffraction from the oxide film, the growth of the aqueous oxide can be summarized with a model in Fig. 6-20. In region A, no diffraction pattern of cuprite was observed. During this time, adsorption of oxygen on the surface and possible diffusion into the substrate might have occur. The oxygen could become the nucleus for the oxide. In growth region B,

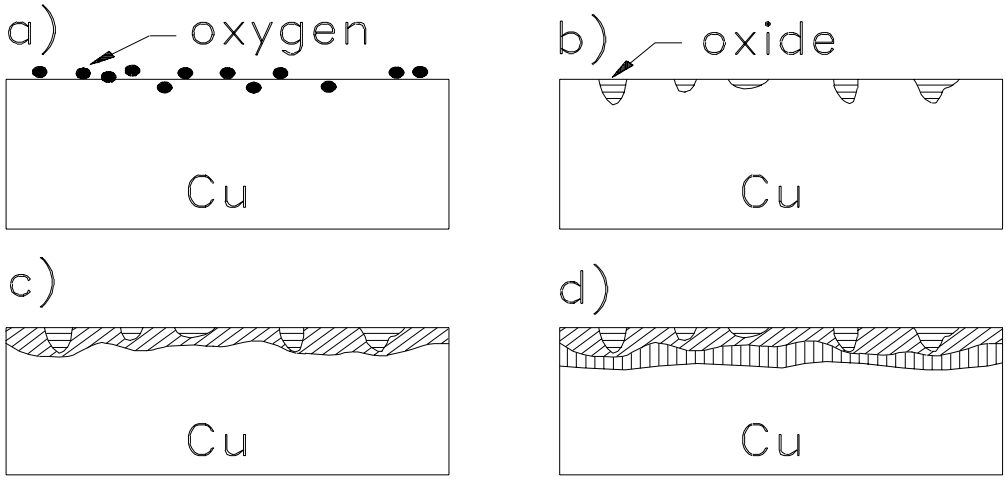

Figure 6-20: Growth of the aqueous oxide. a) Oxygen adsorption on the surface and possible diffusion before formation of oxide, b) Initial growth of non-uniform oxide film with possible formation of narrow oxide pits. Highly strained and compressed oxide film. c) Conversion of copper atoms between the oxide pits into oxide with no significant increase of the film thickness. d) Uniform growth of oxide and passivation.

the diffraction pattern of cuprite structure was first observed. Highly non-uniform film up to 60 Å-thick was observed, possibly involving formation of narrow oxide pits into the copper substrate. The oxide film was highly strained with average lateral strain of -1.7 % and the oxide unit cell volume was compressed by about 4%. The diffraction intensity was very weak and did not increase much with the film thickness. In growth region C, the intensity of the oxide diffraction peak increased rapidly, yet the film thickness has not increased significantly, probably because of lateral spreading of the oxide so that the regions between the oxide pits were getting converted to oxide. The epitaxial strain of the film became somewhat reduced, and the unit cell volume of the oxide became rapidly relaxed toward the bulk value. In the final phase of the growth, the film was growing uniformly. Before the passivation, the in-plane lattice spacing of the oxide film was still strained by about -1 %, but the unit cell volume was almost completely relaxed.

6.5 Discussion

Our X-ray diffraction study demonstrated that the same epitaxial oxides were formed during both native and aqueous oxidation (at pH 4.5). Though their structure and epitaxial relationship with the substrate were identical, the native and aqueous oxides were different in many respects. The most interesting contrast was found in their growth properties. During the native oxidation, both parallel (aligned) and anti-parallel (reversed) cuprites were observed to grow into the bulk phase. The same results have been reported for the oxide grown under vacuum at temperatures, 150~800° C [1,2, 14]. However, during the aqueous oxidation at pH 4.5, only the reversed cuprite was found to grow in the bulk phase, while the aligned cuprite remained as a very thin film, no more than a few layers thick. In the same experiment performed at pH 13, we found only the reversed cuprite. The native aligned cuprite, initially present on the surface, disappeared completely after the reduction, and only the reversed cuprite was observed in the subsequent

aqueous oxidation. Therefore, the preferential growth of the reversed orientation over the aligned orientation appears to be the common characteristics of the aqueous oxidation, strongly suggesting that the oxidation mechanisms in the electrochemical environments might be fundamentally different from those of the dry oxidation.

A possible reason for the preferential growth of the reversed orientation is that the reversed cuprite might have a more energetically favorable interface with the substrate. However, the fact that both orientations were observed in the dry oxidation suggests that the energy difference, if exits at all, may not be significant. A obvious candidate mechanism to bring about the oriented growth would be the preferred nucleation of oxide along the surface steps, which are likely nucleation sites. During the dry oxidation in vacuum, the observed pyramidal growth of oxide along $[110]$ and $[1\bar{1}0]$ directions on Cu(111) have been attributed to the preferred nucleation along the steps [1]. In addition, the oxides with the same orientation have been found to form islands of size ~ 0.1 μm [1, 2, 15]. Since the islands of opposite orientations are too dissimilar to have originated from the initial nucleus by means of tilt or slip, it has been speculated that the two distinct orientations of oxide might be formed at the time of nucleation [15]. However, a realistic surface has a distribution of different step edges, and the preferred nucleation along these step edges inevitably leads to growth of both orientations. Therefore, the preferred growth of the reversed cuprite during the aqueous oxidation can not be explained by the preferred nucleation of oxide along step edges alone.

A possible explanation for this phenomenon can come from the symmetry of the cuprite structure. As shown in Fig. 6-2, the cubic unit cell is asymmetric with respect to the (111) plane going through the oxygen in the body centered position, which we will call plane O. While plane O and plane ABC are separated by the copper atoms forming the base of the tetrahedron around

the body centered oxygen atom, while no copper plane exists between plane O and plane abc. However, this asymmetry is local around a specific oxygen atom and no longer present if an entire crystallographic unit cell is considered. At the initial stage of oxidation, oxygen ions or hydroxide are likely to be specifically adsorbed probably at the 3-fold hollow sites on the Cu(111) surface or at the step edges. The formation of cuprite requires the oxygen and copper atoms to nucleate around the initial adsorbate structures. Since oxygen exists as charged species (O^{2-} or OH^-) in solution and the surface is electrified at the electrochemical environment, the local asymmetry of the cuprite structure with regard to the distribution of oxygen and copper atoms can impose significant influence on the subsequent formation of cuprite structure from the initial adsorbate structures, which may eventually lead to growth of only one orientation. This locally asymmetric property of the cuprite structure is not likely to influence the resulting oxide structure significantly during the dry oxidation, because the copper and oxygen exist mainly as neutral species. The slight difference in the oxide growth properties between the aqueous oxidation at pH 4.5 and at pH 13 may be due to the difference in the kinetic properties of the charged species (i.e. mobility of copper ions, hydroxide, oxygen ions), or the pH dependent nature of the aqueous interface (i.e. concentration of hydroxide, effect of pH on electrolysis of water).

Regardless of the exact reason, the preferential growth of the reversed oxide still provides valuable insights into the aqueous oxidation process. If the oxidation were to occur at the interface between the oxide film and the electrolyte, the crystallographically preferential oxide growth would be very difficult to maintain because the possible dislocations and defects in the oxide film would interfere with the perfect selection of one epitaxial orientation over the other. Therefore, the growth must occur at the interface between the Cu(111) surface and the oxide film, leading inward oxide growth into the substrate rather than the outward growth from the oxide film

to the electrolyte. Furthermore, this peculiar oxide growth property could have significant applications in corrosion/oxidation inhibition of the copper surface. Since the aligned cuprite does not grow beyond a few monolayers, the surface covered with only the aligned cuprite would not be oxidized further, acting as a corrosion barrier.

The difference between the native and aqueous oxides was also found in their epitaxial strain and relaxation behavior. When the native oxide film was thin, the observed in-plane spacing was very close the 3-7 commensurate spacing while the surface-normal spacing was much larger than the bulk spacing. As the film grew thicker with time, both in-plane and the surface-normal spacing approached toward the bulk spacing. This is in agreement with the findings on the oxide grown in vacuum [1]. However, the aqueous oxide film displayed much larger strain and very different relaxation behavior. The observed values for the in-plane lattice spacing for the thin aqueous oxide film were much smaller than the 3-7 commensurate spacing (see Fig. 6-16). Even when the oxide film became considerably thick, the in-plane spacing was below the 3-7 commensurate spacing. For the native oxide, an in-plane spacing smaller than the 3-7 commensurate spacing was never observed. Furthermore, the trend in the surface normal lattice spacing is exactly opposite to that of the native oxide. Consequently, the volume of the aqueous oxide unit cell was significantly compressed (about 4%) at the beginning of the oxidation and relaxed toward the bulk value. Almost complete relaxation (99.7 % of the bulk volume) was achieved after passivation. A very different relaxation behavior of the aqueous oxide film suggests the native and aqueous oxidation processes might involve different oxide formation mechanisms.

6.6 Conclusion

X-ray diffraction technique was used to study the aqueous oxidation of the Cu(111) single

crystal surface in 0.1 M $NaClO_4$ at pH 4.5. The observed native oxide and the aqueous oxide exhibited the same structure and epitaxial relationship with the Cu(111) substrate, which is in agreement with the results of the previous studies on the oxide grown under vacuum. However, the aqueous oxide displayed dramatically different growth properties as well as its strain relaxation behavior. This difference shows that the aqueous oxidation process is fundamentally different from the native oxidation process.

6.7 References

[1]I. H. Ho and R. W. Vook, J. Cryst. Growth, **44**, 561 (1978).

[2] D. A. Goulden, Phil. Mag. **33**, 393 (1976).

[3] G. W. Simmons, D. F. Mitchell and K. R. Lawless, Surf. Sci. **8**, 130 (1967).

[4] F. Jensen, F. Besenbacher, E. Laegsgaard and I. Stensgaard, Surf. Sci., **259**, L774 (1991).

[5] L. H. Dubois, Surf. Sci., **119**, 399 (1982).

[6] F. Jensen, F. Besenbacher, E. Laegsgaard and I. Stensgaard, Phys. Rev., **B 42**, 9206 (1990).

[7] U. Döbler, K. Baberschke, J. Stö, and D. A. Outka, Phys. Rev. **B31**, 2532 (1985).

[8] B. J. Cruickshank, D. D. Sneddon and A. A. Gewirth, Surf. Sci., **281**, L308 (1993).

[9] J. R. LaGraff and A. A. Gewirth, Surf. Sci. **326**, L461 (1995).

[10] N. Ikemiya, T. Kubo and S. Hara, Surf. Sci., **323**, 81 (1995).

[11] R. W. G. Wyckoff, *Crystal Structures*, 2nd ed., Vol. 1 (Wiley, New York, 1963).

[12] I. K. Robinson, H. Graafsma, A. Kvick, and J. Linderholm, Rev. Sci. Instr. **66**, 1675 (1995).

[13] J. H. van der Merwe, Surf. Sci. **31**, 198 (1972).

[14] D. F. Mitchell and K. R. Lawless, J. Paint Technol., **38**, 575 (1966).

[15] R. H. Milne and A. Howie, Philosophical Magazine A, **49**, 665 (1984).

Appendix: X-ray Diffraction[1]

1. 3D diffraction

The x-ray scattering amplitude from a block of crystal, ignoring the polarization factor, can be expressed as

$$A(\boldsymbol{q}) = A_0\left(\frac{r_e}{R}\right)F(\boldsymbol{q})S(\boldsymbol{q}) \qquad \text{(A1-1)}$$

where q is the momentum transfer, the difference from the incident and exit wavevectors ($\boldsymbol{q} \equiv \boldsymbol{k}_f - \boldsymbol{k}_i$), A_0 is the incident amplitude, r_e is the classical radius of electron, R is the distance to the observer. The term, $A_0(r_e/R)$, is the (classical) scattering contribution from an electron. The structure factor , $F(\boldsymbol{q})$, accounts for the scattering contribution from all the atoms in a unit cell. It can be written as

$$F(\boldsymbol{q}) = \sum_{j=1}^{N_c} f_j(q)e^{i\boldsymbol{q}\cdot\boldsymbol{r}_j} \qquad \text{(A1-2)}$$

where the summation is for the entire atoms in the unit cell, $f(q)$ is the atomic scattering form factor, and r_j is the relative coordinates of the atoms in the unit cell. Alternatively, $F(\boldsymbol{q})$ can be viewed as the Fourier transform of the electron density for one unit cell of the crystal. The term, $S(\boldsymbol{q})$, contains the systematical summation of all the unit cells in the crystal. If the crystal block contains N_i unit cells along the crystal axes vectors, a_i (i = 1, 2, and 3), $S(\boldsymbol{q})$ can be written as

---

[1] More complete discussion can be found in I. K. Robinson and D. J. Tweet, Rep. Prog. Phys. **55**, 599 (1992)

$$S(\boldsymbol{q}) = \prod_{i=1}^{3} S_{N_i}(\boldsymbol{q}\cdot\boldsymbol{a}_i) = \sum_{n_1=0}^{N_1-1}\sum_{n_2=0}^{N_2-1}\sum_{n_3=0}^{N_3-1}\exp\{i\boldsymbol{q}\cdot(n_1\boldsymbol{a}_1 + n_2\boldsymbol{a}_2 + n_3\boldsymbol{a}_3)\} \qquad \text{(A1-3)}$$

The square modulus of S_N, representing the scattered intensity, is

$$\left|S_N(x)\right|^2 = \frac{\sin^2(Nx/2)}{\sin^2(x/2)}\ , \qquad \text{(A1-4)}$$

and becomes the δ-function in the large-N limit

Thus, the conditions for the maximum diffracted intensity (the Laue conditions) are

$$\boldsymbol{q}\cdot\boldsymbol{a}_1 = 2\pi h$$

$$\boldsymbol{q}\cdot\boldsymbol{a}_2 = 2\pi k$$

$$\boldsymbol{q}\cdot\boldsymbol{a}_3 = 2\pi l \qquad \text{(A1-5)}$$

where the integer h, k, and l are called Miller indices. The Laue conditions can be satisfied by the $\boldsymbol{q}$ vector,

$$\boldsymbol{q} = h\boldsymbol{b}_1 + k\boldsymbol{b}_2 + l\boldsymbol{b}_3 \qquad \text{(A1-6)}$$

with the bases

$$\boldsymbol{b}_1 = 2\pi\frac{\boldsymbol{a}_2\times\boldsymbol{a}_3}{\boldsymbol{a}_1\cdot\boldsymbol{a}_2\times\boldsymbol{a}_3},\ \text{etc.} \qquad \text{(A1-7)}$$

The set of points satisfying the Laue conditions form the reciprocal lattice, which is spanned by the reciprocal bases $\{\boldsymbol{b}_1, \boldsymbol{b}_2, \boldsymbol{b}_3\}$ orthogonal to $\{\boldsymbol{a}_1, \boldsymbol{a}_2, \boldsymbol{a}_3\}$. Thus, the 3D diffraction intensity is zero unless the $\boldsymbol{q}$ vector coincides with a discrete reciprocal lattice point, and the intensity is given by

$$I_{hkl} = \left|A_0\left(\frac{r_e}{R}\right)F(h\boldsymbol{b}_1 + k\boldsymbol{b}_2 + l\boldsymbol{b}_3)N_1N_2N_3\right|^2 \qquad \text{(A1-7)}$$

2. **Crystal truncation rods**

The derivation of the 3D diffraction shown in the previous section ignores the fact that the crystal has the surfaces. The sharp boundary of crystal face gives a rise to an additional diffraction pattern. Since the Fourier transform of a surface, represented by a step function, is $1/q$, the diffraction intensity near the Bragg peaks now exhibits $1/(\Delta q)^2$ dependence along the surface normal direction. Although a parallelepiped crystal has six faces, in most experimental cases, only the face of the crystal on which the x-ray beam strikes is important. The faces on the sides do not contribute because the dimension of the beam is usually smaller than the sample and/or the edges of the beam are not sharp. The bottom face is unimportant due to the limited penetration of the beam.

The formulation of the "crystal truncation rods" can derived from the 3D diffraction. If one of the Laue conditions is relaxed so that $q_3 a_3 \neq 2\pi l$, Eq. (A1-3) can be rewritten (in the limit, N_1, N_2, and $N_3 \to \infty$),

$$S(2\pi h/a_1, 2\pi k/a_2, q_3) = N_1^2 N_2^2 \frac{\sin^2(N_3 q_3 a_3/2)}{\sin^2(q_3 a_3/2)} = N_1^2 N_2^2 \frac{1}{2\sin^2(q_3 a_3/2)} \quad \text{(A2-1)}$$

where the rapid oscillations of the numerator are averaged out to be 1/2. Thus, the diffraction intensity is sharp in two surface parallel directions while it is diffuse and non-zero (referred to as "rod") in the surface normal-normal direction.

Alternatively, the CTR can be obtained by construction of the diffraction amplitude coming from the semi-infinite crystal inside with absorption ε from one layer to the next,

$$S_3'(q_3a_3) = \sum_{j=0}^{\infty} \exp\{-(iq_3a_3 + \varepsilon)j\} = \frac{1}{1 - \exp(-iq_3a_3 - \varepsilon)} \qquad \text{(A2-1)}$$

In the limit, $\varepsilon \to \infty$, the square modulus of S_3' takes a form $1/2\sin^2(q_3a_3/2)$. This interpretation of the CTR is quite useful because the measured CTR intensity can be fitted with the 1D layered model representing the surface (see chapter 3 for details).

Vita

Yong Song Chu was born in Seoul, Korea on March 31, 1965. He and his family emigrated to the United States in 1983 and settled down in Maryland. After having graduated from Eleanor Roosevelt High School in Greenbelt, MD, he enrolled at California Institue of Technology in 1985 and recieved a B. S. degree in physics four years later. He entered the graduate college of the University of Illinois in 1989 and received a M.S. degree in phisics 1990. From the summer of 1990 to the end of 1992, he studied neculea physics with prof. Doug. Beck. Since Jan. 1993, he has studying surface science with prof. Ian K. Robinson unitl the completion of his Ph. D. work in Feb. 1997.